2016

Factors Controlling the Formation of Unconformity-related Uranium Deposits in Sedimentary Basins: Insights from Reactive Mass Transport Modeling

Yousef Beiraghdar Aghbelagh
University of Windsor

Factors Controlling the Formation of Unconformity-related Uranium Deposits in Sedimentary Basins: Insights from Reactive Mass Transport Modeling

by

Yousef Beiraghdar Aghbelagh

A Dissertation

Submitted to the Faculty of Graduate Studies

through the Department of Earth and Environmental Sciences

in Partial Fulfillment of the Requirements for

the Degree of Doctor of Philosophy

at the University of Windsor

Windsor, Ontario, Canada

2016

Factors Controlling the Formation of Unconformity-related Uranium Deposits in Sedimentary Basins: Insights from Reactive Mass Transport Modeling

by

Yousef Beiraghdar Aghbelagh

APPROVED BY:

_____

Dr. John Molson, External Examiner
Université Laval

_____

Dr. Ronald Barron
Department of Mathematics & Statistics

_____

Dr. Iain M. Samson
Department of Earth & Environmental Sciences

_____

Dr. Ali Polat
Department of Earth & Environmental Sciences

_____

Dr. Jianwen Yang, Advisor
Department of Earth & Environmental Sciences

2 May 2016

Declaration of Co-Authorship / Previous Publication

I. Co-Authorship Declaration

I hereby declare that this thesis incorporates material that is result of joint research, as follows:

The collaboration occurs in Chapter 2, 3 and 4 of this dissertation. These chapters contain material that has been published or submitted for publication. They are coauthored with Dr. Jianwen Yang. He provided advice on numerical experiments, result analyses, and paper writing. However, the key ideas, primary contributions, numerical experiments, and data interpretation, were performed by the author of this thesis.

I am aware of the University of Windsor Senate Policy on Authorship and I certify that I have properly acknowledged the contribution of other researchers to my thesis, and have obtained written permission from each of the co-author(s) to include the above material(s) in my thesis.

I certify that, with the above qualification, this thesis, and the research to which it refers, is the product of my own work.

II. Declaration of Previous Publication

This thesis includes 3 original papers that have been previously published/submitted for publication in peer reviewed journals, as follows:

Thesis Chapter	Publication title/full citation	Publication status
Chapter 2	Aghbelagh Y., and Yang, J., Effect of graphite zone in the formation of unconformity-related uranium deposits: insights from reactive mass transport modeling: Journal of Geochemical Exploration, v. 144, p. 12-27.	Published

Chapter 3	Aghbelagh Y., and Yang, J., Evaluation of Fe-rich chlorite as a reducing agent in the formation of unconformity-related uranium deposits: insights from reactive mass transport modeling: submitted to Mineralium Deposita (under review)	Submitted (under review)
Chapter 4	Aghbelagh Y., and Yang, J., Role of hydrodynamic factors in controlling the formation and location of unconformity-related uranium deposits: insights from reactive flow modeling: submitted to Hydrogeology Journal (under review)	Submitted (under review)

I certify that I have obtained a written permission from the copyright owner(s) to include the above published material(s) in my thesis. I certify that the above material describes work completed during my registration as graduate student at the University of Windsor.

I declare that, to the best of my knowledge, my thesis does not infringe upon anyone's copyright nor violate any proprietary rights and that any ideas, techniques, quotations, or any other material from the work of other people included in my thesis, published or otherwise, are fully acknowledged in accordance with the standard referencing practices. Furthermore, to the extent that I have included copyrighted material that surpasses the bounds of fair dealing within the meaning of the Canada Copyright Act, I certify that I have obtained a written permission from the copyright owner(s) to include such material(s) in my thesis.

I declare that this is a true copy of my thesis, including any final revisions, as approved by my thesis committee and the Graduate Studies office, and that this thesis has not been submitted for a higher degree to any other University or Institution.

Abstract

This thesis aims at investigating the formation and controlling factors of unconformity-related uranium (URU) deposits through fluid flow and reactive mass transport modeling.

The role of a graphite zone was first addressed using two different reducing mechanisms. In the first mechanism, uraninite precipitation involves methane as a reductant. In the second mechanism, oxygen is used for formulating the redox reaction. Results show that uraninite can precipitate below the unconformity and away from the graphite zone regardless of the reducing agent. However, methane leads to a higher grade in uranium mineralization.

Fe-rich chlorite was next investigated. Results show that Fe^{2+}, released by destruction of Fe-rich chlorite, reduces the oxidized uranium and therefore is a viable mechanism to precipitate uraninite. Both basinal sandstone and basement were evaluated as a uranium source using two separate models. For both models uraninite precipitates in the basement and either away from or along the fault, depending on the fault permeability. However, precipitated uraninite has a greater grade in the first model than that in the second model and exhibits both chlorite and muscovite alterations that are commonly present in most basement-hosted URU deposits. The second model exhibits only muscovite alteration.

The role of hydrodynamic factors was finally investigated by assigning different dip angles and directions to faults and various permeabilities to hydrostratigraphic units. Results show that these factors govern the fluid flow pattern, temperature distribution, and uranium mineralization. A vertical fault results in uranium mineralization at the bottom of the fault within the basement, while a dipping fault leads to uraninite

precipitation below the unconformity either away from or along the fault. A more permeable fault causes uraninite precipitation along the fault, whereas a less permeable fault gives rise to the precipitation of uraninite away from it. No economic ore mineralization forms when either very low or very high permeabilities are assigned to the sandstone or basement.

Physicochemical parameters also exert an additional control on both location and grade of URU deposits. Uranium mineralization occurs in locales experiencing a reduction of oxygen fugacity and having a temperature of 160-180 ^{o}C and a pH of about 4-4.5.

Acknowledgements

I would like to thank my supervisor, Dr. Jianwen Yang, for his enthusiasm, dedication and patience during this research. I thank him for his assistance and willingness to discuss many aspects of this work, and also many suggestions that helped improve this thesis. I have benefited tremendously from Dr. Yang's considerable experience in numerical modeling of fluid flow, heat and reactive mass transport as well as in English writing. I also thank Dr. Iain M. Samson for the valuable discussions in relation to the speciation calculation and geochemistry of the hydrothermal deposits. I acknowledge Dr. Ali Polat for his valuable comments on my proposal, and encouraging me throughout this study. Special thanks to Dr. Ronald Barron, from whom I gained much knowledge in computational fluid dynamics (CFD).

This research is supported by the Natural Science and Engineering Research Council of Canada (NSERC)'s Discovery Grant to Dr. Jianwen Yang. It is also sponsored by the University of Windsor's International Graduate (Doctoral) Excellence Scholarship and the University of Windsor's Doctoral Tuition Scholarship.

Dr. Tianfu Xu (at Lawrence Berkeley National Laboratory University of California, Berkeley) and Alison Alcott (at Rockware Company) are sincerely appreciated for their help on the use of TOUGHREACT code.

I acknowledge faculty, staff members, and graduate students in the Department of Earth and Environmental Sciences for their encouragement. I had a great time with them.

Finally, I would like to thank my parents and siblings for their support during this study.

Table of contents

List of tables

List of figures

Chapter 1

Introduction

1.1 Introduction

Unconformity-related uranium (URU) deposits represent the most profitable uranium resource because of their exceptionally high grade and large tonnage (Derome et al., 2005; De Veslud et al., 2009). They are located within or around the unconformities between Proterozoic basin fill and underlying Archean to lower Proterozoic metamorphic sedimentary rocks, where reductants and faults exist (Jefferson et al., 2007). In recent years, various models have been proposed for the URU deposition mechanism:

1. Mixing between oxidized basinal brines and basement-derived reduced fluids (Hoeve and Sibbald, 1978; Pagel et al., 1980; Ypma and Fuzikawa, 1980; Hoeve and Quirt, 1987; Wilson and Kyser, 1987; Kotzer and Kyser, 1990; Kotzer and Kyser, 1995; Raffensperger and Garven, 1995b; Fayek and Kyser, 1997)
2. Adsorption into clays and/or chlorite (Ferguson et al.,1980; Taylor and Rowntree, 1980)
3. Interaction of basinal brines with the reduced basement lithologies (Binns et al., 1980; Donnelly and Furguson, 1980; Hoeve and Quirt, 1984; Komninou and Sverjensky, 1996; Fayek and Kyser, 1997)
4. Changes in physicochemical parameters such as pressure, temperature, pH, and/or oxygen fugacity (Wilde and Wall, 1987; Wilde et al., 1989; Raffensperger and Garven, 1995b)

Among the above models, No. 1 and No. 3 are more popular. In model No. 1, the sedimentary fill serves as the source of both the uranium and oxidizing mineralizing fluids (e.g., Hoeve and Sibbald, 1978; Kyser et al., 2000); uranium minerals precipitate when oxidizing uranium-bearing brines mix with basement-derived reducing fluids or react with reducing brines in the basement. It has been proposed that thermal convection is responsible for moving fluids around to leach uranium (Raffensperger and Garven, 1995a, b; Cui et al., 2010). Model No. 3 considers the basement as the source of the uranium that is leached by the oxidizing basinal fluids after they penetrated into the basement (e.g., Cuney et al., 2003; Richard et al., 2010; Cui et al., 2012b). It is also believed that uranium precipitation in most deposits is related to a decrease of oxygen fugacity, generally resulting from the interaction of oxidized uranium-bearing fluids with reductants (Cuney, 2009).

Although significant progress has been made with respect to understanding the formation of URU deposits (e.g., Hoeve and Sibbald, 1978; Hoeve and Quirt, 1984, 1987; Kotzer and Kyser, 1995; Fayek and Kyser, 1997; Alexandre and Kyser, 2012; Cui et al., 2010, 2012a, 2012b; Chi et al., 2013, 2014; Li et al., 2014, 2015), several aspects of uranium mineralization of this type are still not fully understood: 1) what is the role of graphite zones in the formation of URU deposits? 2) how do various physicochemical parameters impact the formation of URU deposits? 3) is it possible for uranium mineralization to occur via inorganic reducing agents such as Fe-rich chlorite? 4) why do some URU deposits form along basement fault zones while others form away from the faults? 6) how do various hydrodynamic factors control the formation and location of the URU deposits? and 7) where is the large amount of uranium sourced for URU deposits?

The thesis aims to address these questions by developing a series of reactive mass transport models and conducting systematic numerical simulations.

1.2 Background and literature review

URU deposits are located close to the unconformity between Archean to lower Proterozoic metamorphic rocks and middle Proterozoic sandstone cover with reverse faults that are rooted in the basement graphitic metasedimentary rocks (Hoeve and Sibbald, 1978; Hoeve and Quirt, 1984; Ramaekers, 1990; Kotzer and Kyser, 1995; McGill, 1999; Derome et al., 2005). The Athabasca Basin (Fig. 1.1) in northern Saskatchewan, as a premiere host of URU deposits, has an estimated geological reserve of about 427 million kg of U_3O_8 (Fayek and Kyser, 1997), and Saskatchewan is a major producer (about 30 %) of the world's uranium (Fayek and Kyser, 1997).

Geologically, the Athabasca Basin is located on the western Churchill province between the eroded remnants of two major orogenic belts: the 1.9 Ga Taltson magmatic zone to Thelon tectonic zone and the 1.8 Ga Trans-Hudson Orogeny (Fig. 1.2). The deposition of the sediments is dated to late Paleoproterozoic to Mesoproterozoic at about 1.7 Ga, and is separated from the underlying basement by a major unconformity. The Snowbird tectonic zone (Fig. 1.3), which has a northeast trend, separates the basement to Rae province to the west and the Hearne province to the east, both of which consist of Archean gneisses, Paleoproterozoic platform, metasedimentary rocks and mafic to felsic plutons (Madore et al., 1999; Thomas et al., 2000; Annesley and Madore, 2002).

The Athabasca Basin occurs as a series of northeast-southwest oriented sub-basins (Fig. 1.4) controlled by major Hudsonian faults rooted in the basement rocks (Hoeve and

Sibbald, 1978; Hoeve and Quirt, 1984; Ramaekers, 1990; Kotzer and Kyser, 1995). These faults were reactivated after the filling of the Athabasca Basin (Hoeve and Sibbald, 1978; Kotzer and Kyser, 1995) and have remained active until recent times (Hoeve and Quirt, 1984). The basin fill comprises the Athabasca Group, a sequence of thick unmetamorphosed fluviatile quartzose sandstones deposited in a proximal shelf environment (Ramaekers and Catuneanu, 2004). The Athabasca Group in the eastern part of the basin is made up exclusively of the Manitou Falls formation (Fig. 1.5), which consists of coarse to fine-grained hematite-rich conglomerates along thin stratigraphic horizons, indicating oxidation of heavy mineral layers, siltstones, and sandstones filling (Ramaekers, 1990). Fluid inclusions and diagenetic clay assemblage studies (Pagel et al., 1980; Hoeve et al., 1981; Halter, 1988) reveal a maximum total thickness of 5-7 km for the sediments in the basin. The metamorphic basement consists of a steeply dipping belt of northeast-trending metapelitic gneisses, granitoid gneisses and migmatitic gneisses of the Trans-Hudson orogeny. Most of the known URU deposits are located in the eastern Athabasca Basin (Figs. 1.3 and 1.5) in the vicinity of the graphite-rich Cable Bay shear zone that occurs between the Mudjatik and the Wollaston domains. Recent reflection seismic studies indicate that the unconformity between the basinal sandstone and the basement is at shallow depth (~ 200 m) in the eastern Athabasca Basin, but much deeper (~ 2000 m) in the center of the basin (Derome et al., 2005).

The conditions for the genesis of URU deposits include: 1) large-scale migration of uranium transported by acidic and oxidizing diagenetic solutions circulating in permeable sedimentary rocks close to the bottom of the basin and infiltrating into the underlying basement to at least several hundred meters; 2) development of strongly argillized

alteration zones on both sides of the unconformity; and 3) massive accumulation of uraninite at redox fronts stabilized near the unconformity (Morichon et al., 2010). The first common feature of all URU deposits is a structural trap – an area where mobilized uranium had "pooled" and deposited uranium minerals (http://www.nuinsco.ca). Exceptional trapping conditions commonly resulted from a strong redox gradient between the oxidized sandstone cover and the graphite-rich metasedimentary rocks of the basement and the openings created in the sandstone and the basement by the combined effects of reverse tectonics and quartz dissolution (Lorilleux et al., 2002; Cuney, 2009). Cuney (2009) also proposed that the space created by quartz dissolution within sudoite–dravite breccia bodies was the site of mixing between reducing silica-undersaturated, basement-derived fluids and the uranium-bearing oxidized fluids, forming a trap for uranium mineralization. Faulting and fracturing of the basement and overlying sandstone (Fig. 1.6) have an important role in enhancing fluid flow, focusing mineralizing fluids, and controlling the deposition of the ore in all URU deposits (Jefferson et al., 2007; Needham and Stuart–Smith, 1980; Wilson and Kyser, 1987; Raffensperger and Garven, 1995a). The ability of faults to localize fluids depends on their size, spatial distribution and their relationship to the aquifer (Cui et al., 2010). The reduction of U(VI) to U(IV) and subsequent UO_2 precipitation were spatially associated with the intersection of graphite rich basement-rooted faults and the basement-sandstone unconformity, which may have acted as redox interfaces (Hoeve and Quirt, 1987). The unconformity interface itself also plays an important role in the fluid flow regime and consequently ore deposition (Cui et al., 2010), since it is a zone with relatively high permeability and porosity that enhanced fluid flow (Cui et al., 2010).

Recent genetic models concur that diagenetic brines are the main ore-forming fluids (Cuney, 2009; Derome et al., 2005). However, there is a controversy regarding the nature of the basement-derived brines. Some researchers (e.g., Richard et al., 2010) believe that basal fluids were originally oxidizing basinal brines, but modified through fluid-rock interaction to gain U, Ca, Sr and Ba; while others (e.g., Alexandre et al., 2009) propose that basement-derived fluids were reducing. One significant characteristic of the ore-forming fluids, which differentiates them from any known modern systems, is their oxidation state. Fluids responsible for the formation of URU deposits must have had a high oxygen fugacity to transport appreciable amount of uranium (Komninou and Sverjensky, 1996; Raffensperger and Garven, 1995b). Thermodynamic calculations (Komninou and Sverjensky, 1996) show that log fO_2 must have been above -24 at 200 °C to account for dissolved U(VI) (as uranyl complexes), well above that of the hematite-magnetite buffer (log fO_2=-39.5 at 200 °C).

Numerical modeling has been employed to delineate the uncertainties associated with the formation of a variety of ore deposits (Feltrin et al., 2009; Yang et al., 2004a, 2004b, 2010a, b), and also to examine ore-forming fluid flow in relation to the genesis of URU deposits. The first numerical attempt to model the formation of URU deposits was made by Raffensperger (1993) and Raffensperger and Garven (1995a). Using 2D modeling, they concluded that free convection is a viable driving mechanism for the formation of URU deposits within a sedimentary basin. De Veslud et al. (2009) conducted 3D modeling to evaluate the geometrical and geological relationships between breccias, faults, and mineralization zones in the Athabasca Basin. They indicated a strong spatial correlation between mineralized bodies and the sudoite-dravite breccia bodies,

that appears to be controlled by reverse shear zones cross-cutting the unconformity and containing graphite in the basement. Within the space created by quartz dissolution in the breccia body, mixing between the basement and basinal fluids induced uranium deposition and allowed the development of high-grade mineralization (De Veslud et al., 2009).

Cui et al. (2010) examined the topographic relief and thermally-induced buoyancy as fluid flow driving mechanisms for the formation of URU deposits. By assigning different gradients to the water table elevation, they concluded that in a high water table slope (about 0.001 m/m) forced convection (gravity-driven flow) is dominant, and in a moderate water table slope (about 0.0005 m/m) mixed convection (resulted from combined effect of buoyancy and gravity forces) prevails. Only at a low water table slope (about 0.0001 m/m), free convection is dominant which is capable of leaching and redistributing uranium in sandstone sequences. They also evaluated the effect of unconformity, stratigraphic heterogeneity, and faults on fluid flow and temperature regime, and revealed that fluid flux is enhanced in the unconformity interface, and uranium concentration tends to occur within or around the unconformity due to the high flux. Their results also exhibited that the ability of faults to localize fluids depends on their size, spatial distribution and their relationship to the aquifer. More recently, a hydrodynamic study by Li et al. (2015) showed that the location and spacing of the basement faults influence the pattern and position of the convection cells within the basinal sandstone.

Recent studies (e.g., Boiron et al., 2010; Richard et al., 2010) argue that basinal brines may flow into the basement to hundreds of meters below the unconformity, not

only along major faults, but also through a dense network of microfractures. Cui et al. (2012b) confirmed that buoyancy-driven thermohaline fluids can penetrate into the underlying basement to some depth, and the basal fluids can also flow up into the basin. By assuming a uranium source to be located below the unconformity either in the center or close to the margin, they concluded that basement-derived uranium can be transported into the overlying basinal sediments by free convection.

The effect of tectonic deformation and fluid pressure on the mineralization of URU deposits was investigated by various researchers (e.g., Chi et al., 2011; Cui et al., 2012a, Chi et al., 2013; Li et al., 2015). Cui et al. (2012a) developed a thermo-hydro-mechanical model by integrating existing data from the Athabasca, Thelon, and Kombolgie basins to investigate the role of deformation-driven flow in the formation of URU deposits. It was suggested that free convection is a dominant mechanism for leaching uranium in absence of tectonic deformation. Their numerical experiments showed that reactivation of pre-existing basement structures and generation of new faults, resulting from tectonic deformation, suppresses the free convection and leads to deformation-dominated fluid flow or mixed convection, depending on strain rates. For relatively high strain rates, deformation-driven flow dominates the system. However, a mixed convection (co-existence of thermally driven free convection and deformation driven fluid flow) may occur at low strain rates. During compressive deformation, reduced brines in the basement may be squeezed out along fractured zones and encounter uranium-bearing fluids in the clastic sequence to form sandstone-hosted URU deposits (Cui et al., 2012a). By contrast, basement-hosted URU deposits are likely to form during extension, when oxidized basinal brines flow into faulted structures to interact with reduced minerals or

fluids in the basement (Cui et al., 2012a). In weakly overpressured or zero overpressure regimes, uranium ore mineralization occurs mainly near the unconformity interface (Chi et al., 2011; Chi et al., 2013; Chi and Xue, 2014; Li et al., 2015).

Reactive flow modeling has recently been applied to the study of a variety of types of mineral deposits including URU deposits (Raffensperger and Garven, 1995b), copper (Lichtner and Biino, 1992a; He et al., 1999; Kuhn et al., 2004), bauxite (Soler and Lasaga, 1998), and Mississippi Valley-type deposits (Lichtner and Biino, 1992b; Appold and Garven, 2000). Raffensperger and Garven (1995b) simulated the formation of URU deposits in the Athabasca Basin over a time scale of 0.1 to 1 Ma, and suggested that a high permeable graphite-rich zone in the crystalline basement was necessary to focus groundwater flow along this zone and to provide methane as a reductant for uranium deposition. Komininou and Sverjensky (1996) employed reaction path modeling to test the capability of uranium-bearing fluids in forming uranium-ore bodies, and also reproduced the alteration observed in the URU deposits.

1.3 Objectives of study

1.3.1 Overall objectives

The goal of this study is to develop fully coupled fluid flow, heat transport and reactive mass transport models to better understand the formation of URU deposits and the controlling factors in sedimentary basins, in particular in the Athabasca Basin.

1.3.2 Specific objectives

There are several ambiguities concerning the formation of URU deposits. The thesis aims to address the following outstanding issues through systematic reactive flow modeling.

I. Effect of a graphite-rich zone

Despite the general understanding that a graphite-rich shear zone in the Athabasca Basin has an ore-controlling role (Cuney et al., 2003; Jefferson et al., 2007), its exact role in the formation of URU deposits is still not fully understood, and therefore requires further investigation through reactive mass transport modeling.

II. The impact of various physicochemical parameters

Physicochemical parameters (e.g., pressure, temperature, oxygen fugacity and pH) control whether metals are deposited to form ore, or remain in fluids to be transported elsewhere. Komninou and Sverjensky (1996) conducted speciation calculations and showed that the amount of total uranium dissolved in the fluid is a strong function of the oxygen fugacity. Nutt (1989) suggested that a drop in pH accompanying chloritization could promote uraninite precipitation by destabilizing uranyl-carbonate complexes. Speciation calculations suggest that fluids responsible for the formation of URU deposits were distinguished from basal brines by their high oxygen fugacity and relatively low pH. The impact of these physicochemical parameters in controlling the location and grade of URU deposits is therefore also investigated.

III. Fe-rich silicates as a reducing agent in URU mineralization

Debate continues with respect to reducing agents for precipitation of uraninite. Hoeve and Sibbald (1978) proposed that graphitic metapelitic gneiss was the source of reductants to precipitate uraninite. Kyser et al. (1989) suggested that methane generated by graphite dissolution was not responsible for reduction of uranium, and suggested that the highly permeable graphite zone only played a hydromechanical role by allowing the basinal fluids to channel into the basement. Komininou and Sverjensky (1996) argued that minerals being rich in reduced iron were the major cause of uranium reduction. These minerals can be either metamorphic phases such as Fe-rich garnet, biotite, or hornblende or Fe-rich chlorite produced during the pre-ore alteration. Destruction of these Fe-rich silicates releases Fe^{2+} in solution and causes reduction of the oxidized uranium present in solution. One of the objectives of this research is therefore to test whether or not Fe^{2+}, released by the destruction of Fe-rich chlorite, can reduce the oxidized uranium present in a solution as a viable mechanism for uraninite precipitation.

IV. The uranium source

Two possible uranium sources have been proposed for the formation of URU deposits in the Athabasca Basin. One suggests that the uranium source is mainly from uranium-bearing phases, such as apatite, zircon, and monazite in the sandstones of the Manitou Falls Formation. In this model, uranium is leached from these minerals by basinal fluids and transported downward into suitable structural traps such as fracture zones and faults in the basement, and then deposited by reaction with reducing rock types or by mixing with reducing fluids of basement origin (Wilson and Kyser, 1987; Kotzer and Kyzer, 1995; Fayek and Kyser, 1997). The other proposes that the uranium source is monazite in

the metamorphic basement rocks while oxidized fluids still originate from sedimentary basins (Hecht and Cuney, 2000; Derome et al., 2003). One objective of this thesis is therefore to evaluate whether the overlying basinal sandstones or the basement rocks are more likely the source of the uranium in forming unconformity-related deposits.

V. The role of hydrodynamic factors

Hydrodynamic factors, such as the dip angle and direction of faults and the permeability of various hydrostratigraphic units, control fluid flow dynamics, and consequently thermal regime in sedimentary basins (Hitchon, 1969a, b; Senger and Fogg, 1987; Belitz and Bredehoeft, 1988), which in turn affects uranium mineralization. The last objective of this thesis is to address the role of these factors in controlling the formation and location of uranium deposits since no similar numerical investigation has been done previously.

Below is a summary list of the objectives:

1. Effect of graphite-rich zone
2. The impact of various physicochemical parameters
3. Fe-rich silicates as a reducing agent in URU mineralization
4. The uranium source
5. The role of hydrodynamic factors

1.4 Methodology and principles

The research throughout the thesis was carried out mainly by employing 2D numerical modeling techniques integrated with geological and geochemical constraints, following the general numerical modeling framework (Fig. 1.7) for addressing scientific problems (Cimbala and Cengel, 2006; Cui, 2012). A typical unconformity-related uranium system contains five important elements: (1) basinal sandstone above the unconformity; (2) upper confining unit; (3) unconformity interface; (4) reduced metamorphic basement beneath the unconformity; (5) basement faults. Hydrological properties associated with these units, such as porosity, permeability and thermal conductivity are important variables controlling fluid flow, heat and reactive solute transport. These properties were determined based on data used in similar numerical modeling studies and on published compilations (e.g., Freeze and Cherry, 1979; Garven and Freeze, 1984; Raffensperger and Garven, 1995a, b; Mclellan et al., 2004; Yang et al., 2004; Oliver et al., 2006; Cui et al., 2012a). The data from petrography, fluid inclusions, and geochemical analysis of bulk components, trace elements, and x-ray diffraction measurements on cores was also used for further constraining the numerical models. In particular, fluid inclusions provide information on the temperature, salinity, pressure and composition of paleofluids (Goldstein, 2001; Samson et al., 2003), and hence help to constrain the properties of mineralizing fluids in the models.

Reactive mass transport modeling was carried out using the non-isothermal multi-component reactive fluid flow and geochemical transport code TOUGHREACT (Xu et al., 2004a). The governing equations for fluid flow, heat and reactive mass transport, and the integral finite difference (IFD) method for solving the governing equations are presented in Appendix 1. The code can be applied to one-, two-, or three-dimensional

porous and fractured media with physical and chemical heterogeneity, and can accommodate any number of chemical species present in liquid, gas and solid phases. Figure 1.8 shows the flowchart (Xu et al., 2004a) for solving coupled non-isothermal multiphase fluid flow, solute transport, and reactive geochemistry in TOUGHREACT. In brief, after solving the flow equations, the fluid velocities and phase saturations are used for the chemical transport simulation, which is solved on a component-by-component basis. The resulting concentrations obtained from solving the transport equations are substituted into the chemical reaction model. The system of mixed equilibrium-kinetic chemical reaction equations is solved on a grid block by grid block basis by Newton-Raphson iteration. The chemical transport and reactions are solved iteratively until convergence.

Iteration between fluid flow and heat transport solutions allows updating water properties (e.g., density and viscosity) via the EOS modules which calculate these properties using the steam table equations, given by the International Formulation Committee (1967).

Effect of mineral precipitation/dissolution on the porosity, permeability, and consequently fluid flow is considered. Porosity changes are calculated from changes in volume fraction of minerals (Xu et al., 2004):

$$\varphi = 1 - \sum_{m=1}^{nm} f_{rm} - f_{ru} \qquad (1.1)$$

where nm is the number of minerals, f_{rm} is the volume fraction of the mineral m in the rock ($V_{mineral}/V_{medium,}$ including porosity), and f_{ru} is the volume fraction of nonreactive rock. As the f_{rm} of each mineral changes, the porosity is recalculated in each time step. Matrix permeability changes are calculated from changes in porosity using ratios of

permeabilities calculated from the Carman-Kozeny equation (Bear, 1972), ignoring the changes in grain size, tortuosity and specific surface area:

$$k = k_i \frac{(1-\varphi_i)^2}{(1-\varphi)^2} \left(\frac{\varphi}{\varphi_i}\right)^3 \quad (1.2)$$

Porosity and permeability are up-dated in each iteration and used in the coupled fluid flow and heat transport equations.

1.5 Organization of thesis

This thesis is structured as follows.

Chapter 2 investigates the effect of a graphite zone in the formation of URU deposits. To achieve this goal, two different reducing mechanisms are examined for the precipitation of uraninite in a typical URU deposit. In the first mechanism, precipitation of the uraninite involves methane as a reducing agent that is produced by the dissolution of the graphite. The second reducing mechanism does not incorporate methane as a reducing agent, and oxygen is used for formulating the redox reaction of uraninite precipitation. This chapter answers the following important questions: 1) is methane required for uranium mineralization? 2) is it possible for uraninite to precipitate by other redox mechanisms? 3) why are some uranium deposits not associated with graphite zones? 4) how do physicochemical parameters such as oxygen fugacity and temperature influence the formation of URU deposits?

In chapter 3, Fe-rich chlorite is evaluated as a reducing agent in the precipitation of URU deposits. This chapter answers the question of whether URU deposits can form by

inorganic reducing agents such as Fe-rich chlorite, and whether these mechanisms can lead to high-grade uranium deposits. This chapter also answers the question of where the large amount of uranium is likely sourced for uranium mineralization. Finally, this chapter also investigates the effect of the fault permeability on the location of URU deposits.

Chapter 4 aims to address the role of various hydrodynamic factors, including fault dip angle, fault dip direction, and permeability of each hydrostratigraphic unit involved, in controlling the formation and location of URU deposits. This chapter also explains the reasons why the size and grade of uranium deposits in sedimentary basins are different, and proposes that both the basement and the sandstone seem to have an optimal window of permeability for the formation of economically significant URU deposits.

Chapter 5 summarizes the original contributions and recommendations for future research.

Fig. 1.1. The location of Athabasca Basin (modified from Aben Resources Ltd).

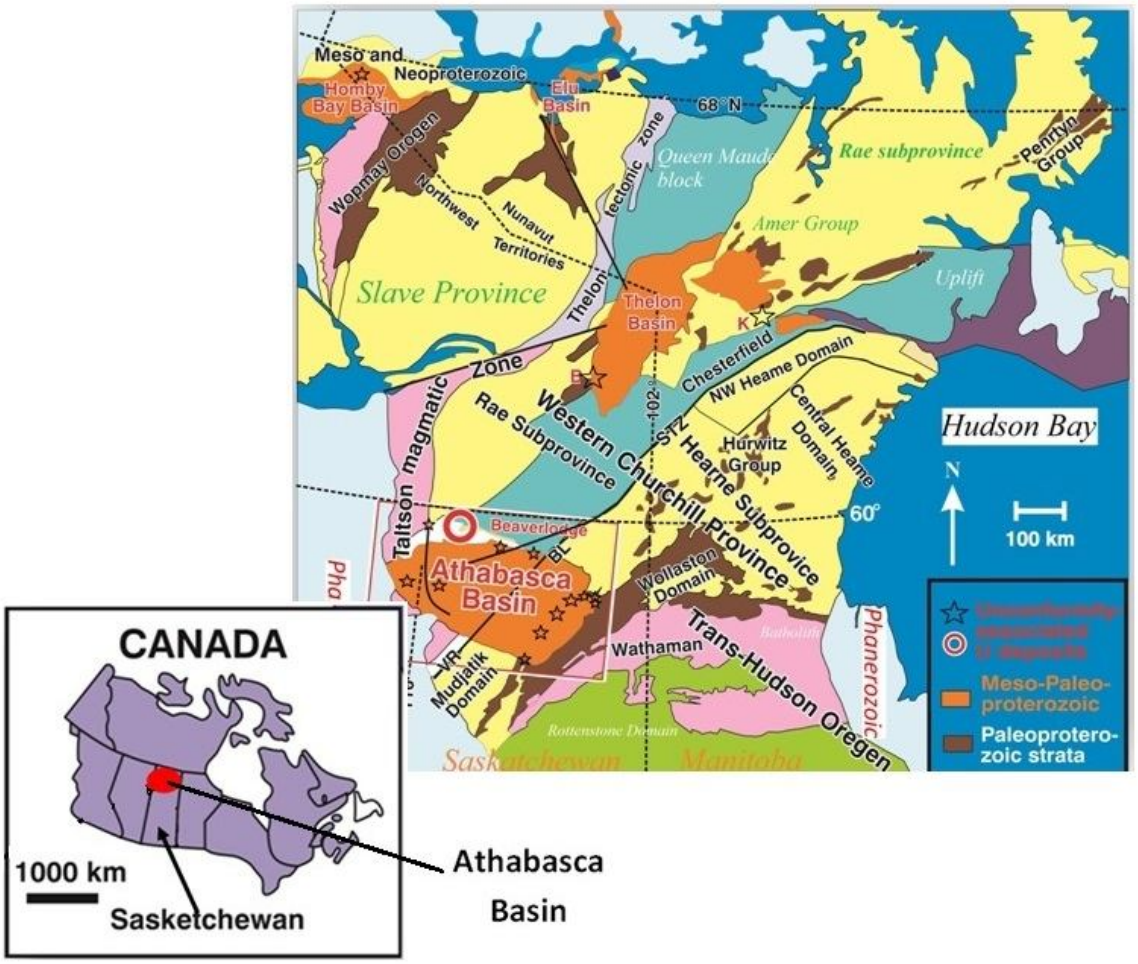

Fig. 1.2. Unconformity-related uranium deposits, prospective Proterozoic basins and basement elements of the northwestern Canadian Shield (modified from Jefferson et al., 2007).

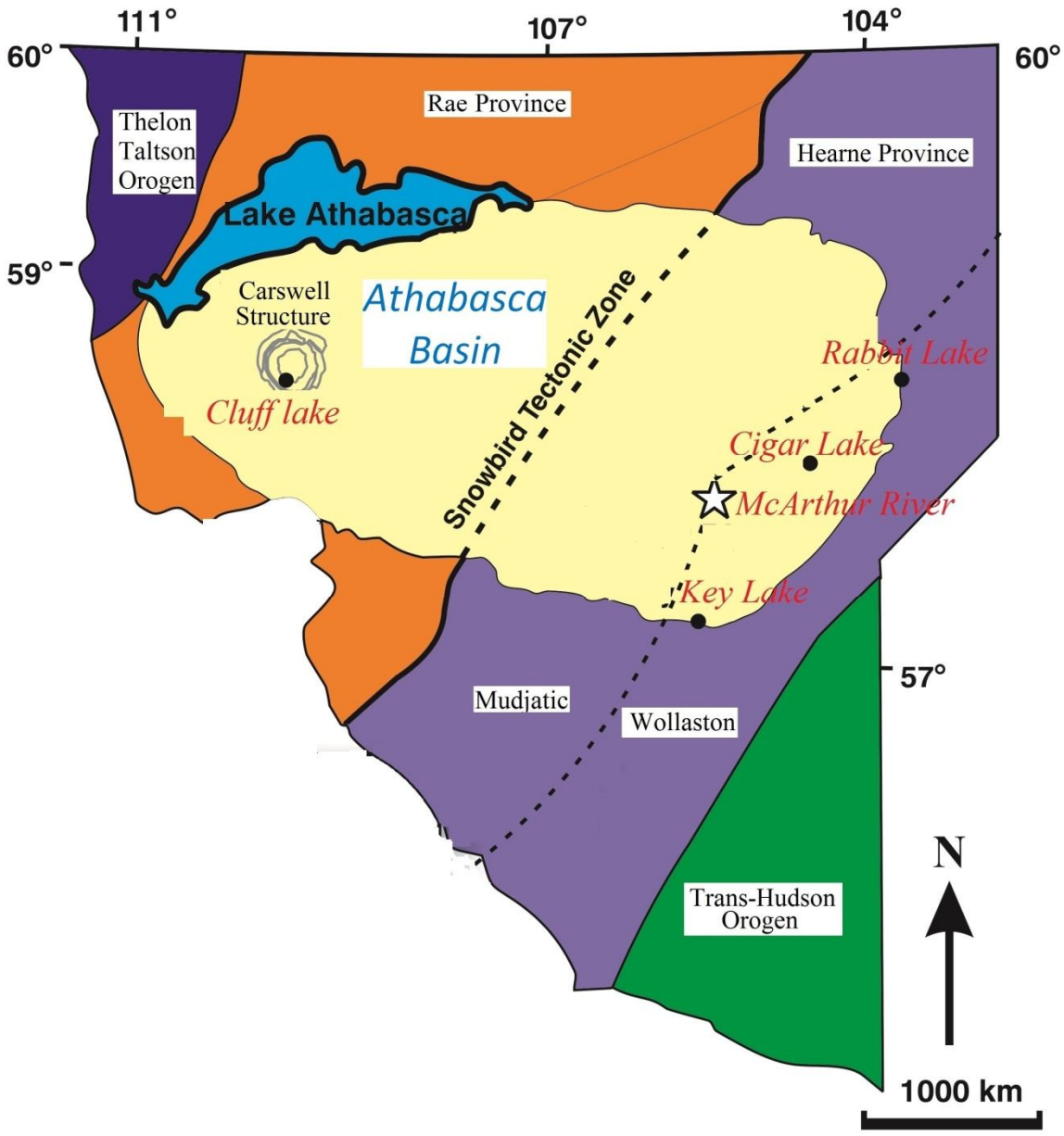

Fig. 1.3. Snowbird tectonic zone and location of the main unconformity-related uranium deposits in the Athabasca Basin (modified from Derome et al., 2005).

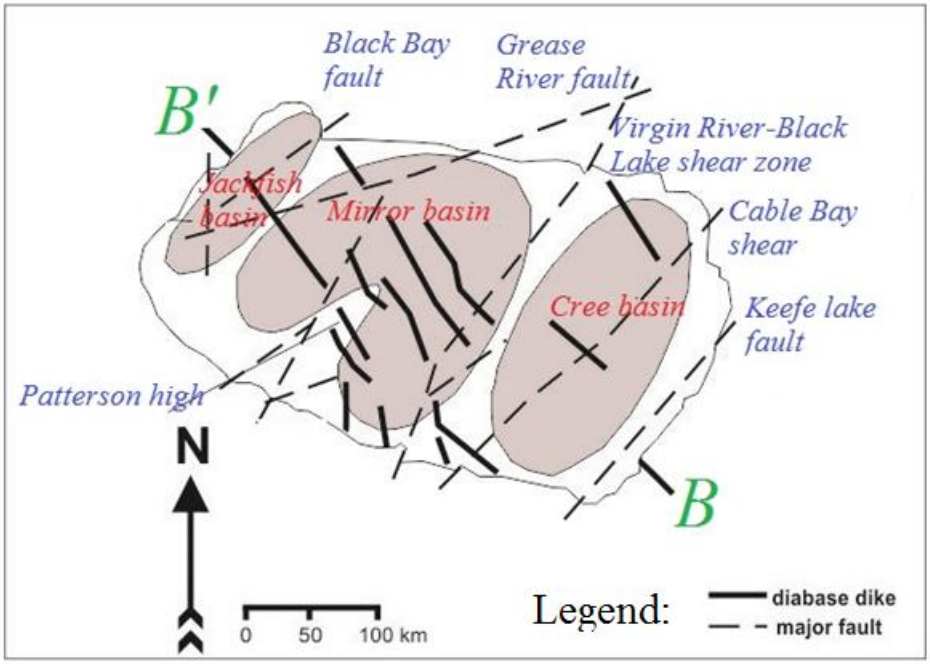

Fig. 1.4. Location of sub-basins, major faults, and diabase dikes in the Athabasca Basin (modified from Hoeve and Quirt, 1984).

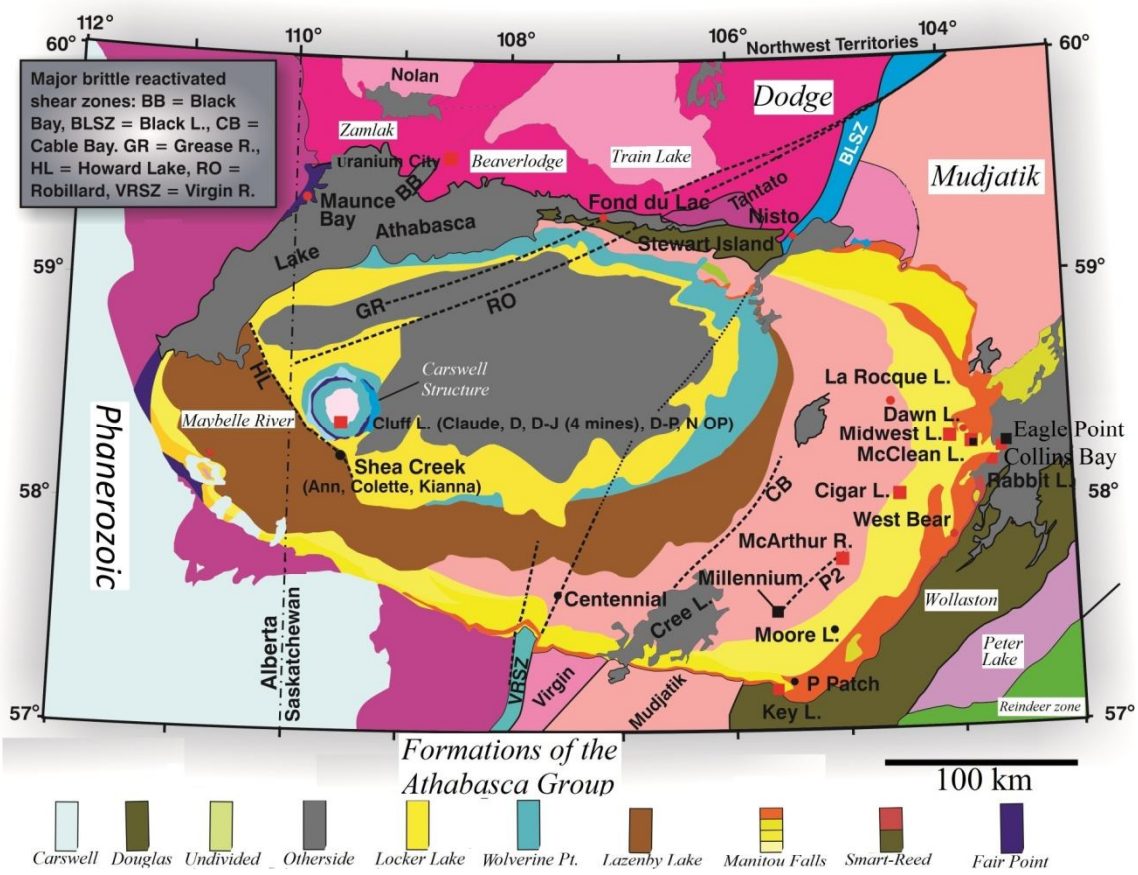

Fig. 1.5. Geological setting and unconformity-related uranium occurrences of the Athabasca Basin. Heavy dashed lines are selected major reactivated fault zones (modified from Jefferson et al., 2007).

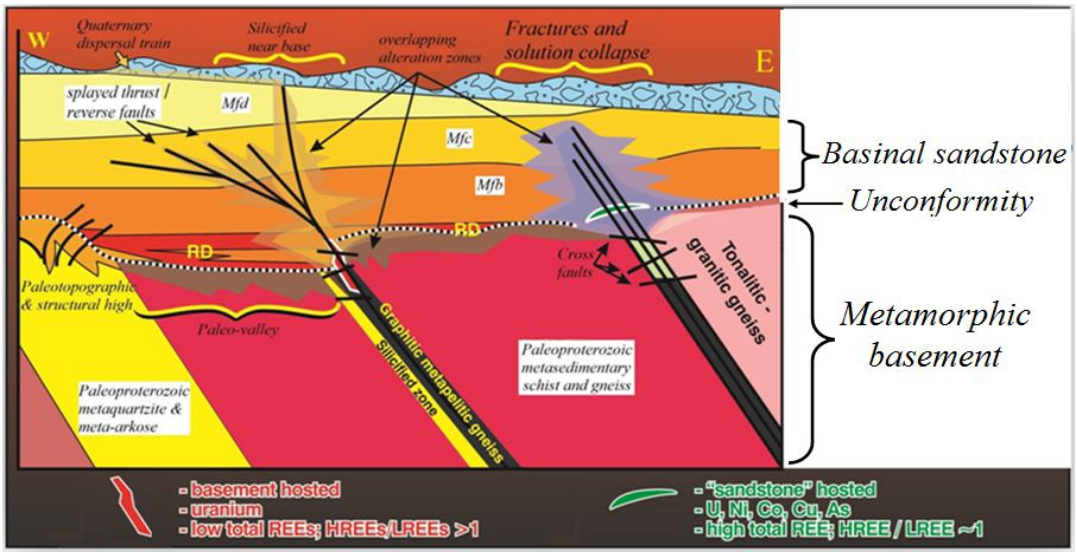

Fig. 1.6. Schematic cross-section of typical URU deposits in the eastern part of Paleoproterozoic Athabasca Basin. This cross-section illustrates both sandstone-hosted and basement-hosted styles of URU deposits (modified from Sibbald et al. (1976), Hoeve and Sibbald (1978), Hoeve and Quirt (1984), McGill et al. (1993), Ruzicka (1993), Thomas et al. (2000), and Tourigny et al. (2007)).

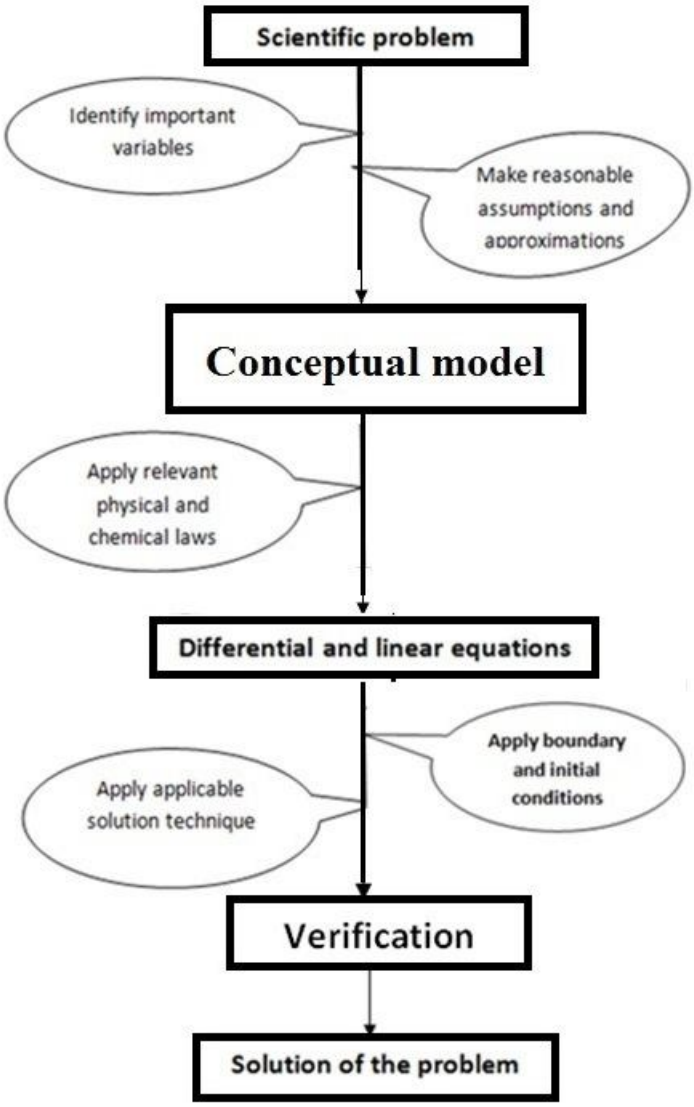

Fig. 1.7. Schematic of modeling framework (modified from Cimbala and Cengel, 2006).

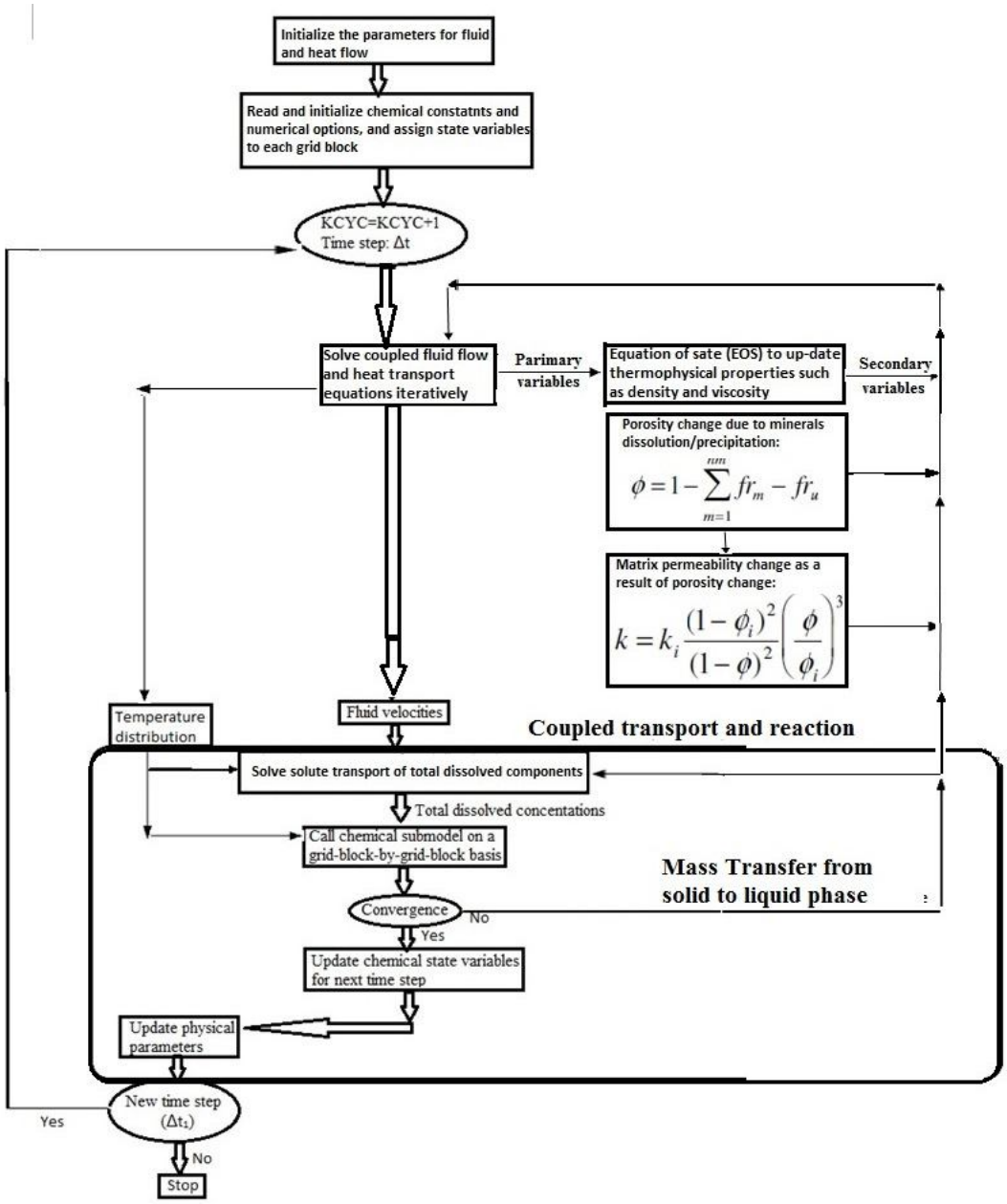

Fig. 1.8. Flowchart of the TOUGHREACT program (modified from Xu et al., 2004a).

References

Aben Resources Ltd: www.abenresources.com/s/uranium.asp.

Alexandre, P., and Kyser, T.K., 2012, Modeling of the fluid flow involved in the formation of Athabasca Basin unconformity-type uranium deposits: Joint annual meeting of the Geological Association of Canada-Mineralogical Association of Canada, Abstracts, v. 35, p. 3.

Alexandre, P., Kyser, K., and Jiricka, D., 2009, Critical geochemical and mineralogical factors for the formation of unconformity-related uranium deposits: Comparison between barren and mineralized systems in the Athabasca basin, Canada: Economic Geology, v. 104, p. 413-435.

Annesley, I.R., and Madore, C., 2002, Thermotectonics of Archean/Paleoproterozoic basement to the eastern Athabasca unconformity-type uranium deposits, in Kribek, B., and Zeman, J., eds., Uranium deposits: From their genesis to their environmental aspects: Czech Geological Survey, p. 33–36.

Appold, M.S., and Garven, G., 2000, Reactive flow models of ore formation in the southeast Missouri Pb-Zn-Cu district: Economic Geology, v. 95, p. 1605-1626.

Bear, J. 1972, Dynamics of fluids in porous materials: New York, Elsevier (reprinted by Dover Publications, 1988), 784 p.

Belitz, K., and Bredehoeft, J.D., 1988, Hydrodynamics of Denver Basin: explanation of subnormal fluid pressures: American Association of Petroleum Geologists Bulletin, v. 72, p. 1334-1359.

Binns, R.A., Ayres, D.E., Wilmshurst, J.R., and Ramsden, A.R., 1980, Petrology and geochemistry of alteration associated with uranium mineralization at Jabiluka,

Northern Territory, Australia. International Uranium Symposium on the Pine Creek Geosyncline (J.Fergusen and A.B.Goleby, eds): International Atomic Energy Agancy, Vienna, p. 417-438.

Boiron, M.C., Cathelineau, M., and Richard, A., 2010, Fluid flows and metal deposition near basement/cover unconformity: Lessons and analogies from Pb-Zn-F-Ba systems for the understanding of Proterozoic U deposits: Geofluids, v. 10, p. 270-292.

Chi, G., Bosman, S., and Card, C., 2013, Numerical modeling of fluid pressure regime in the Athabasca basin and implications for fluid flow models related to the unconformity-type uranium mineralization: Journal of Geochemical Exploration, v. 125, p. 8–19.

Chi, G., Li, Z., and Bethune, K.M., 2014. Numerical modeling of hydrocarbon generation in the Douglas Formation of the Athabasca basin (Canada) and implications for unconformity-related uranium mineralization: Journal of Geochemical Exploration, v. 144, p. 37–48.

Cimbala, J., and Cengel, Y., 2006, Fluid Mechanics: Fundamentals and Applications. McGraw-Hill, New York.

Cui, T., 2012, The formation mechanisms of unconformity-related uranium deposits: numerical modeling concerning the Thelon Basin: Unpublished PhD thesis, University of Windsor, Windsor, Canada.

Cui, T., Yang, J., and Samson, I. M., 2010, Numerical modeling of hydrothermal fluid flow in the Paleoproterozoic Thelon Basin, Nunavut, Canada: Journal of Geochemical Exploration, v. 106, p. 69-76.

Cui, T., Yang, J., and Samson, I. M., 2012a, Tectonic deformation and fluid flow: Implication for the formation of unconformity-related uranium deposits: Economic Geology, v. 107, p. 147-163.

Cui, T., Yang, J., and Samson, I. M., 2012b, Uranium transport across basement/cover interfaces by buoyancy driven thermohaline convection: implications for the formation of unconformity-related uranium deposits: American Journal of Science, v. 312, p. 994-1027.

Cuney, M., 2009, The extreme diversity of uranium deposits: Mineralium Deposita, v. 44, p. 3-9.

Cuney, M., Brouand, M., Cathelineau, M., Derome, D., Freiberger, R., Hecht, L., Kister, P., Lobaev, V., Lorilleux, G., and Peiffert, C., 2003, What parameters control the high grade-large tonnage of the Proterozoic unconformity related uranium deposits?: Uranium Geochemistry, Nancy, France, International Conference, pp. 123-126.

De Veslud, C.L.C., Cuney, M., Lorilleux, G., Royer, J.J., Jébrak, M., 2009, 3D modeling of uranium-bearing solution-collapse breccias in Proterozoic sandstones (Athabasca Basin, Canada)-metallogenic interpretations: Computers & Geosciences, v. 35, p. 92–107.

Derome, D., Cathelineau, M., Cuney, M., Fabre, C., Lhomme, T., and Banks, D.A., 2005, Mixing of sodic and calcic brines and uranium deposition at McArthur River, Saskatchewan, Canada: A Raman and Laser-Induced breakdown spectroscopic study of fluid inclusions: Economic Geology, v. 100, p. 1529-1545.

Derome, D., Cuney M., Cathelineau, M., Dubessy, J., and Bruneton, P., 2003, A detailed fluid inclusion study in silicified breccias from the Kombolgie sandstones (Northern

Territory, Australia): Application to the genesis of Middle-Proterozoic unconformity-type uranium deposits: Journal of Geochemical Exploration, v. 80, p. 259-275.

Donnelly, T.H., and Ferguson, J., 1980, A stable isotope study of three deposits of Alligator River uranium field, N. T. International Uranium Symposium on the Pine Creek Geosyncline (J.Fergusen and A.B.Goleby, eds): International Atomic Energy Agancy, Vienna, p. 397-406.

Fayek, M., and Kyser, T.K., 1997, Characterization of multiple fluid-flow events and rare-earth-element mobility associated with formation of unconformity type uranium deposits in the Athabasca Basin, Saskatchewan: The Canadian Mineralogist, v. 35, p. 627–658.

Feltrin, L., McLellan, J., and Oliver, N., 2009, Modeling the giant, Zn-Pb-Ag Century deposit, Queensland, Australia: Computers and Geosciences, v. 35, p. 108-133.

Ferguson, J., Ewers., G.R., and Donnelly, T.H., 1980, Model for the development of economic uranium mineralization in the alligator river uranium field. International Uranium Symposium on the Pine Creek Geosyncline (J.Fergusen and A.B.Goleby, eds): International Atomic Energy Agancy, Vienna, p. 563-574.

Garven, G., and Freeze, R. A., 1984, Theoretical analysis of the role of groundwater flow in the genesis of stratabound ore deposits: 2. Quantitative results: American Journal of Science, v. 284, p. 1125-1174.

Goldstein, R.H., 2001, Fluid inclusions in sedimentary and diagenetic systems: Lithos, v. 55, p.159-193.

Halter, G., 1988, Zonality of alterations in the environment of uranium deposits associated to Middle Proterozoic unconformity (Saskatchewan, Canada): Ph.D. Dissertation, Universite´ Louis Pasteur, Strasbourg, 252pp.

Hecht, L., and Cuney, M., 2000, Hydrothermal alteration of monazite in the Precambrian crystalline basement of the Athabasca Basin (Saskatchewan, Canada): implications for the formation of unconformity-related uranium deposits: Mineralium Deposita, v. 35, p. 791-795.

Hitchon, B., 1969a, Fluid flow in the Western Canada Sedimentary Basin: 1. Effect of topography: Water Resources Research, v. 5, p. 186-195.

Hitchon, B., I 969b, Fluid flow in the Western Canada Sedimentary Basin: 2. Effect of geology: Water Resources Research, v. 5, p. 460-469.

Hoeve, J., and Quirt, D., 1984, Mineralization and host rock alteration in relation to clay mineral diagenesis and evolution of the middle Proterozoic, Athabasca basin, northern Saskatchewan, Canada: Saskatchewan Research Council Technical Report, 202 pp.

Hoeve, J., and Quirt, D., 1987, A stationary redox front as a critical factor in the formation of high grade, unconformity-type uranium ores in the Athabasca Basin, Saskatchewan, Canada: Bulletin of Mineralogy, v. 110, p. 151–171.

Hoeve, J., Rawsthorn, K., and Quirt, D., 1981, Uranium metallogenetic studies: clay mineral stratigraphy and diagenesis in the Athabasca Group: Saskatchewan Research Council Publication, v. 22, p. 76-89.

International Formulation Committee, 1967, A formulation of the thermodynamic properties of ordinary water substance, IFC secretariat, Düsseldorf, Germany.

Hoeve, J., and Sibbald, T.I.I., 1978, On the genesis of Rabbit Lake and other unconformity-type uranium deposits in northern Saskatchewan, Canada: Economic Geology, v. 73, p. 1450-1473.

Jefferson, C.W., Thomas, D.J., Gandhi, S.S., Ramaekers, P., Delaney, G., Brisbin, D., Cutts, C., Quirt, D., Portella, P., and Olson, R.A., 2007, Unconformity associated uranium deposits of the Athabasca Basin, Saskatchewan and Alberta. In: Goodfellow, W.D. (Ed.), Mineral Deposits of Canada: A Synthesis of Major Deposit-types, District Metallogeny, the Evolution of Geological Provinces, and Exploration Methods: Geological Association of Canada, Mineral Deposits Division, Special Publication, v. 5, p. 273–305.

Komininou, A., and Sverjensky, D.A., 1996, Geochemical modeling of the formation of an unconformity-type uranium deposit: Economic Geology, v. 91, p. 590-606.

Kotzer, T., and kyser, T.K., 1990, The use of stable and radiogenic isotopes in the identification of fluids and processes associated with unconformity-type uranium ore deposits: Geological Society of Saskatchewan Special publication, v. 10, p. 115-131.

Kotzer, T.G., and Kyser, T.K., 1995, Petrogenesis of the Proterozoic Athabasca basin, Northern Saskatchewan, Canada, and its relation to diagenesis, hydrothermal uranium mineralization and Paleohydrogeology: Chemical Geology, v. 120, p. 45–89.

Kyser, T.K., Wilson, M.R., and Ruhrmann, G., 1989, Stable isotope constraints on the role of graphite in the genesis of unconformity-type uranium deposits: Canadian Journal of Science, v. 26, p. 490-498.

Kyser, T.K., Hiatt, E., Renac, C., Durocher, K., Holk, G., and Deckart, K., 2000. Diagenetic fluids in Paleo- and Meso-Proterozoic sedimentary basins and their implications for long protracted fluid histories, in Kyser, T.K., ed., Fluids and basin evolution: Mineralogical Association of Canada, Short Course, v. 28, p 225–262.

Li, Z., Chi, G., Bethune, K.M., Bosman, S.A., and Card, C.D., 2015, Geometric and hydrodynamic modeling and fluid-structural relationships in the southeastern Athabasca Basin and significance for uranium mineralization, *in* Targeted Geoscience Initiative 4: unconformity-related uranium systems, (ed.) E.G. Potter and D.M. Wright: Geological Survey of Canada, Open File 7791, p. 103–114. doi:10.4095/295776.

Li, Z., Bethune, K.M., Chi, G., Card, C.D., and Bosman, S.A., 2014, Topographic features of the sub-Athabasca Group unconformity surface in southeastern Athabasca Basin and its relationship to uranium ore deposits: Joint annual meeting of the Geological Association of Canada - Mineralogical Association of Canada, Abstracts, v.37, p. 162.

Lichtner, P.C., and Biino, G.G., 1992a, A first principles approach to supergene enrichment of a porphyry copper protore: I. Cu-Fe-S subsystem: Geochimica et Cosmochimica Acta, v. 56, p. 3987-4013.

Lichtner, P.C., and Biino, G.G., 1992b, Genesis of mississippi valley- type (MVT) deposits: Geological Society of America, Abstracts with Programs, v. 24, pp. 324.

Lorilleux, G., Je´brak, M., Cuney, M., and Baudemont, D., 2002, Polyphase hydrothermal breccias associated with unconformity-related uranium mineralization

(Canada): from fractal analysis to structural significance: Journal of Structural Geology, v. 24, p. 323–338.

Madore, C., Annesley, I.R., and Tran, H.T., 1999, Petrology and geochemistry of Paleoproterozoic Wollaston Group metasediments from the eastern Keller Lake-Siemens Lake area, Saskatchewan: A preliminary interpretation: Saskatchewan Geological Survey, Summary of Investigations, v. 2, p. 80–89.

McGill, B., Marlatt, J., Matthews, R., Sopuck, V., Homeniuk, L. and Hubregtse, J., 1993, The P2 North uranium deposit Saskatchewan, Canada: Exploration Mining Geology v. 2, p. 321-331.

Millington, R.J., and Quirk, J. P., 1961, Permeability of porous solids, Trans. Faraday Soc., v. 57, p. 1200-1207.

Morichon, E., Beaufort, D., Allard, T., and Quirt, D., 2010, Tracing past migrations of uranium in Paleoproterozoic basins: New insights from radiation- induced defects in clay minerals: Geology, v. 38, p. 983-986.

Needham, R.S., and Stuart -Smith, P.G., 1980, Geology of the alligator River uranium field, in Ferguson, J., and Goleby, A. B., eds., Uranium in the Pine Creek geosyncline: Vinnea: International Atomic Energy Agency, p. 233-257.

Nutt, C.J.,1989, Chloritization and associated alteration at the jabiluka unconformity-type uranium deposit, Northern Territory, Australia: Canadian Mineralogist, v. 27, p. 41-58.

Pagel, M., Poty, B., and Sheppard, S.M.F., 1980, Contribution to some Saskatchewan uranium deposits mainly from fluid inclusion and isotopic data. International

Uranium Symposium on the Pine Creek Geosyncline (J.Fergusen and A.B.Goleby, eds): International Atomic Energy Agency, Vienna, p. 639-654.

Pruess, K., 1987, TOUGH user's guide, Nuclear Regulatory Commission, report NUREG/CR-4645 (also Lawrence Berkeley Laboratory Report LBL-20700, Berkeley, California).

Pruess, K., 1991, TOUGH2: A general numerical simulator for multiphase fluid and heat flow, Lawrence Berkeley Laboratory Report LBL-29400, Berkeley, California.

Pruess, K., Oldenburg, C., and Moridis, G., 1999, TOUGH2 user's guide, Version 2.0, Lawrence Berkeley Laboratory report LBL-43134, Berkeley, California.

Raffensperger, J.P., 1993, Quantitative evaluation of the hydrologic and geochemical processes in the formation of unconformity-type uranium deposits: Unpublished Ph.D. thesis, Baltimore, John Hopkins University, 679 p.

Raffensperger, J.P., and Garven, G., 1995a, The formation of unconformity-type uranium ore deposits 1. Coupled ground water flow and heat transport modeling: American Journal of Science, v. 295, p. 581-636.

Raffensperger, J.P., and Garven, G., 1995b, The formation of unconformity-type uranium ore deposits 2. Coupled hydrochemical modeling: American Journal of Science, v. 295, p. 639-696.

Ramaekers, P., 1990, Geology of the Athabasca Group (Helikian) in northern Saskatchewan: Saskatchewan Energy and Mines, Saskatchewan Geological Survey, Report 195, 49 p.

Ramaekers, P., and Catuneanu, O., 2004, Development and sequences of the Athabasca basin, early Proterozoic, Saskatchewan and Alberta, Canada. In: Eriksson, P.G.,

Altermann, W., Nelson, D.R., Mueller, W.U., Catuneanu, O. (Eds.). The Precambrian Earth: Tempos and Events: Developments in Precambrian Geology. Elsevier Science, Amsterdam, p. 705–723.

Richard, A., Pettke, T., Cathelineau, M., Boiron, M.C., Mercadier, J., Cuney, M., and Derome, D., 2010. Brine–rock interaction in the Athabasca basement (McArthur River U deposit, Canada): consequences for fluid chemistry and uranium uptake: Terra Nova, v. 22, p. 303-308.

Ruzicka, V., 1993, Unconformity-type uranium deposits; in Kirkham, R.V., Sinclair, W.D., Thrope, R.I., and Duke, J.M., eds., Mineral Deposits Modeling: Geological Association of Canada, Special paper, v. 40, p. 125-149.

Samson, I.M., Anderson, A., and Dan, M., 2003, Fluid Inclusions: Analysis and Interpretation: Short Course, Mineralogical Association of Canada, Ottawa, v. 32, 374 p.

Senger, R.K., Fogg, G.E., 1987, Regional underpressuring in deep brine aquifers, Palo Duro Basin, Texas. 1 . Effects of hydrostratigraphy and topography: Water Resources Research, v. 23, p. 1481-1493.

Sibbald, T.I.I., Munday, R.J.C. and Lewry, J.F., 1976, The geological setting of uranium mineralization in northern Saskatchewan, in Dunn, C.E., Uranium in Saskatchewan: Saskatchewan Geological Society, Special Publication, v. 3, p. 51-98.

Soler, J. M., and Lasaga, A.C., 1998, An advection-dispersion- reaction model of bauxite formation: Journal of Hydrology, v. 209, p. 311-330.

Steefel, C.I., and Lasaga, A.C., 1994, A coupled model for transport of multiple chemical species and kinetic precipitation/dissolution reactions with applications to reactive

flow in single phase hydrothermal system: American Journal of Science, v. 294, p. 529-592.

Taylor, G.H., and Rowntree, J.C., 1980, The symposium-retrospect and discussion. International Uranium Symposium on the Pine Creek Geosyncline (J.Fergusen and A.B.Goleby, eds): International Atomic Energy Agancy, Vienna, p. 751-758.

Thomas, D., Matthews, R.B., and Sopuck, V., 2000, Athabasca Basin (Canada) unconformity-type uranium deposits: Exploration model, current mine developments and exploration directions: Geology and Ore deposits 2000: The Great Basin and Beyond: Geological Society of Nevada Symposium, May 15-18, 2000, Proceedings, v. 1, p. 103-125.

Tourigny, G., Quirt, D.H., Wilson, N., Wilson, S., Breton, G., and Portella, P., 2007, Basement geology of the Sue C uranium deposit, McClean Lake area, Saskatchewan, in Jefferson, C.W. and Delaney, G., eds., EXTECH IV: Geology and Uranium Exploration Technology of the Proterozoic Athabasca Basin, Saskatchewan and Alberta: Bulletin 588. Geological Survey of Canada (also Special Publication 18. Saskatchewan Geological Society, Special Publication 4: Geological Association of Canada, Mineral Deposits Division), p. 229-248.

Walter, A.L., Frind, E.O., Blowes, D.W., Ptacek, C.J., and Molson, J.W., 1994, Modeling of multicomponent reactive transport in groundwater: 1, Model development and evaluation: Water Resources Research, v. 30, p. 3137-3148.

Wilde, A.R., and Wall, V.J., 1987, Geology of the Nabarlek uranium deposit, Northern Territory, Australia: Economic Geology, v. 82, p. 1152-1168.

Wilde, A.R., Mernagh, T.P., Bloom, M.S., and Hoffman, C.F., 1989, Fluid inclusion evidence on the origin of some Australian unconformity-related uranium deposits: Economic Geology, v. 84, p. 1627-1642.

Wilson, M. R., and Kyser, T.K., 1987, Stable isotope geochemistry of alteration associated with key lake uranium deposit, Canada: Economic Geology, v. 82, p. 1540-1557.

Xu, T., Sonnenthal, E., Spycher, N., and Pruess, K., 2004a, TOUGHREACT user's guide: A simulation program for non-isothermal multiphase reactive geochemical transport in variable saturated geologic media: Lawrence Berkeley National Laboratory Report LBNL-55460, Berkeley, California, 192 pp.

Yang, J., 2006, Finite element modeling of transient saline hydrothermal fluids in multifaulted sedimentary basins: implications for ore-forming processes: Canadian Journal of Earth Sciences, v. 43, p. 1331-1340.

Yang, J., Bull, S., and Large, R., 2004a, Numerical investigation of salinity in controlling ore-forming fluid transport in sedimentary basins: Example of the HYC deposit, Northern Australia: Mineralium Deposita, v. 39, p. 622-631.

Yang, J., Large, R.R., and Bull, S.W., 2004b, Factors controlling free thermal convection in faults in sedimentary basins: implications for the formation of zinc-lead mineral deposits, Geofluids, v. 4, p. 237-247.

Yang, J., Feng, Z., Luo, X., and Chen, Y., 2010a, Numerically quantifying the relative importance of topography and buoyancy in driving groundwater flow: Science China Earth Sciences, v. 53, p. 64-71.

Yang, J., Feng, Z., and , Luo, X., and Chen, Y., 2010b, Three-dimensional numerical modeling of salinity variations in driving basin-scale ore-forming fluid flow: Example from Mount Isa Basin, northern Australia: Journal of Geochemical Exploration, v. 106, p. 236-243.

Yeh, G.T., Tripathi, V.S.A., 1991, Model for simulating transport of reactive multispecies components: model development and demonstration, Water Reources Research, v. 27, p. 3075-3094.

Chapter 2[1]

Effect of a graphite zone in the formation of unconformity-related uranium deposits: insights from reactive mass transport modeling

2.1 Introduction

Unconformity-related uranium (URU) deposits are the most important and profitable deposits among other types of uranium deposits (Derome et al., 2005; De Veslud et al., 2009). They are located within or around basal unconformities between Proterozoic basin fill and the underlying Archean granitoid gneisses and Paleoproterozoic metamorphic rocks, where reductants and faults exist (Jefferson et al., 2007; Cui et al., 2012). The Athabasca Basin, a premier host of URU deposits, is located in the northern part of Saskatchewan and Alberta. It occurs as a series of northeast-southwest oriented sub-basins controlled by major Hudsonian faults rooted in the basement rocks (Hoeve and Sibbald, 1978; Hoeve and Quirt, 1984; Ramaekers, 1990; Kotzer and Kyser, 1995). These faults were reactivated after the filling of the Athabasca basin (Hoeve and Sibbald, 1978; Kotzer and Kyser, 1995) and have remained active until recent times (Hoeve and Quirt, 1984). Most of the known URU deposits in the Athabasca basin are located in the eastern part of the basin, particularly in the vicinity of the graphite-rich Cable Bay shear zone that occurs between the Mudjatik and the Wollaston domains (Derome et al., 2005).

---

[1]This chapter has been published in a slightly modified form, "Aghbelagh, Y., and Yang, J., 2014. Effect of graphite zone in the formation of unconformity-related uranium deposits: Insights from reactive mass transport modeling. Journal of Geochemical Exploration 144, 12-27.

The McArthur River deposit is a good example of the URU deposits located in the eastern part of the Athabasca basin. The deposit is structurally controlled by the northeast-trending, southeast dipping, graphite-rich reverse fault which is rooted in the basement and extends several meters above the unconformity surface into the basin (Derome et al., 2005). The existence of URU deposits is not limited to the eastern part of the Athabasca basin and there are some URU deposits in other parts of the basin as well. The Shea Creek area, for example, is located in the western part of the Basin. In this area, three main Paleoproterozoic basement lithostratigraphic units have been identified: a metasedimentary unit (consisting of metapelites and garnetites) in which graphite is mainly concentrated along reverse faults, surrounded by two metaigneous felsic gneiss units, one above and another below the metasedimentary package (De Veslud et al., 2009). Despite the general understanding that graphite-rich shear zones in the Athabasca Basin have a critical role in providing the reducing agents (Hoeve and Sibbald, 1978), enhancing the local permeability, and focusing fluid flow (Kyser et al., 1989; Kotzer and Kyser, 1990, Raffensperger, 1993; Raffensperger and Garven, 1995a, b), its exact role in the formation of these deposits is still not fully understood. Some uranium deposits can form in the absence of graphitic units (e.g., Kiggavik, Fuchs and Hilger, 1989; and some of the deposits at Cluff Lake, Jefferson et al., 2007), but they are in the minority. It is still unsure whether super high-grade deposits, such as the McArthur River deposit, can form without the presence of graphite zone (Jefferson et al., 2007).

Computational simulations in the computational geoscience field (Zhao et al., 2008a, 2009) have provided an important, if not unique, way for simulating geological phenomena that take place within the crust of the Earth. Owing to its robust and practical

nature, modeling has been extensively used to deal with fluid flow processes associated with not only a wide range of ore-forming problems (Hobbs et al., 2000; Gow et al., 2002; Ord et al., 2002; Sorjonen-Ward et al., 2002; Zhang et al., 2003, 2008), but also various other types of geoscience problems (Lin et al., 2003, 2006, 2008, 2009; Yan et al., 2003; Liu et al., 2005, 2008, 2010, 2011; Zhao et al., 2008b, 2010; Xing et al., 2008; Zhao, 2009, Schmidt Mumm et al., 2010; Zhang et al., 2011; Mugler et al., 2012; Awadh et al., 2013). The simulation results have greatly enhanced our understanding of controlling dynamic mechanisms behind the mineralization within the upper crust of the Earth (Gow et al., 2002; Ord et al., 2002; Sorjonen-Ward et al., 2002). Furthermore, computational simulations have also been used to solve groundwater pollution problems in the geoevironmental field (Zhao et al., 2008b, 2010; Sung et al., 2012; Khalil et al., 2013; Charifo et al., 2013).

In this study, reactive mass transport modeling is conducted for evaluating the role of faulted graphite zone in the formation of URU deposits, which couples the processes of fluid flow, heat transfer, solute transport, and geochemical reactions in a collective manner. Reactive mass transport modeling has been applied successfully to the study of a number of different types of ore deposits, including URU (Raffensperger and Garven, 1995b), copper (Lichtner and Biino, 1992a; He et al., 1999; Kuhn et al., 2004), bauxite (Soler and Lasaga, 1998), and Mississippi Valley-type deposits (Lichtner and Biino, 1992b; Appold and Garven, 2000). A previous study by Raffensperger and Garven (1995b), predicted the formation of uranium ore deposits in the Athabasca Basin, inside the sandstone cover, over a time scale of 0.1 to 1 Ma. In their conceptual model the graphite unit was only limited to the basement. However, it is now clear that these faulted

graphite units (e.g., McArthur River deposit, Derome et al., 2005) are rooted in the basement and can extend into the basin. Also, they conjectured a single redox process for precipitation of uraninite which involves methane as the reducing agent, and did not examine any other reducing mechanisms for the precipitation of uraninite. In addition, for the dissolution and precipitation of minerals, their model only considers the simple case of equilibrium conditions. But, in reality we need to set up more robust kinetic behavior for the dissolution and precipitation of the minerals in the system.

According to the diagenetic-hydrothermal model proposed for the URU deposits (Hoeve et al., 1981; Hoeve and Quirt, 1984), uranium minerals precipitate when oxidized uranium-bearing brines mix with basement-derived reducing fluids or react with reducing minerals in the basement. Geochemically, precipitation of the uranium in most deposits is related to a decrease of oxygen fugacity, generally resulting from the interaction of oxidized uranium-bearing fluids with reductants (Cuney, 2009). In the present study, in order to evaluate the role of a faulted graphite zone in precipitation of uranium, two different reducing mechanisms are examined. The first mechanism, considered by various researchers (Hoeve and Sibbald, 1978; Raffensperger and Garven, 1995b), deals with the precipitation of uraninite involving methane as the reducing agent. Methane can be produced by the alteration of the graphite zone (Hoeve and Sibbald, 1978; Kyser et al., 1989; Raffensperger and Garven, 1995b) at temperatures of typical URU ore forming brines (120-200 °C) through the following reaction:

$$C + \frac{3}{2}H_2O \leftrightarrow \frac{1}{2}H^+ + \frac{1}{2}HCO_3^- + \frac{1}{2}CH_4^0(aq). \qquad (2.1)$$

Which then acts as a reducing agent for the reduction of uraninite through the following reaction:

$$UO_2^{2+} + \frac{3}{4}H_2O + \frac{1}{4}CH_4^0(aq) \leftrightarrow UO_2 + \frac{1}{4}HCO_3^- + \frac{9}{4}H^+. \quad (2.2)$$

The second mechanism is based upon the following redox reaction which does not involve the methane, and oxygen is used for formulating the redox reaction of uraninite precipitation:

$$UO_2^{2+} + H_2O \leftrightarrow UO_2 + 2H^+ + \frac{1}{2}O_2(aq). \quad (2.3)$$

Equation (2.3) implies that water (H_2O) can be used as a reducing agent to precipitate uraninite. This mechanism works only if oxygen fugacity *(f*O_2*)* is low, so the reaction tends to move to the right side according to Le Chatelier's principle (Atkins and De Paula, 2009). Oxygen fugacity can be reduced by other agents present in the system such as H_2S, Fe^{2+}, etc. Reactive mass transport modeling is carried out to examine both mechanisms for the precipitation of uraninite.

2.2 Conceptual model

Based on recent studies (e.g., Raffensperger and Garven, 1995b; Cui et al., 2012), a sandwich-like conceptual model (Fig. 2.1) is considered in this study which consists of 4 hydrostratigraphic units: basement rock, faulted graphite zone, overlying sandstone, and upper confining unit. Various rock properties (Table 2.1) are assigned to these units based on the data used in similar numerical modeling and published compilations (e.g., Freeze and Cherry, 1979; Garven and Freeze, 1984; Raffensperger and Garven, 1995a, b; Mclellan et al., 2004; Yang et al., 2004; Oliver et al., 2006; Cui et al., 2012a). The numerical grid includes 6400 rectangular integral finite difference (IFD) cells. The bottom and side boundaries are modeled as impermeable boundaries, and the top surface

is considered as a permeable boundary by assigning afixed pore pressure of 30 Mpa to it, assuming a hydrostatic condition based on previous studies (e.g., Chi et al, 2013; Cui et al., 2012a; Cui et al., 2012). For heat transport, the top boundary is fixed at 90 °C, whereas the bottom is assigned a value of 240 °C based on a geothermal gradient of 30 °C/km. The side boundaries are assumed to be insulated to heat transport. The hydrostatic pressure condition and thermal field with a gradient of 30 °C/km are used as the initial conditions. Tables 2.2-2.9, which are based on a previous study on URU deposits by Raffensperger and Garven (1995b), show the initial chemical compositions for each hydrostratigraphic unit. These tables summarize the aqueous compositions and volume fractions of minerals for each hydrostratigraphic unit. The top and bottom boundaries are assigned a first-type transport boundary condition. That is, aqueous components concentration and mineral volume fractions are assumed to be constant, which are the same as those of their respective units (Tables 2.2, 2. 3, 2.8, 2.9). For the side boundaries a second-type boundary condition is employed. That is, the normal gradient of the aqueous components' concentrations and mineral volume fractions is assumed to be zero.

The fluid and mineral composition chosen for each hydrostratigraphic unit is based on a previous study on URU deposits by Raffensperger and Garven (1995b). The basement unit is mainly composed of quartz, muscovite, and K-feldspar with accessory anhydrite, chlorite, hematite, pyrite, and kaolinite (Raffensperger and Garven, 1995b; Hoeve and Quirt, 1984; Fayek and Kyser, 1997; Adlakha et al., 2014). Based on the previous study by Raffensperger and Garven (1995b), it is assumed that this unit has moderately reducing (Log fO_2 =-46.834) and acidic (pH=4.541) conditions. The faulted graphite unit is mainly composed of quartz, muscovite, and graphite along with some accessory

minerals like pyrite, kaolinite, and chlorite. This unit is assumed in more reducing (Log fO_2=-51.285) and slightly acidic (pH=4.094) conditions compared to the basement unit (Raffensperger and Garven, 1995b). Based on the previous study on URU deposits by Raffensperger and Garven (1995b), graphite is only included as a primary mineral in the faulted graphite unit and it is not treated as a primary mineral in other hydrostratigraphic units of the system (basement, sandstone, and cover). But, graphite is allowed to precipitate as a secondary mineral through the fluid-rock interaction. The sandstone unit is predominantly composed of quartz and hematite with accessory muscovite, anhydrite, chlorite, K-feldspar, and kaolinite (Tremblay, 1982; Fayek and Kyser, 1997; Hiatt et al., 2007; Alexandre et al., 2009; Adlakha et al., 2014). This unit is assumed to be the uranium source and an initial fluid composition of 1×10^{-4} mol/L ($\simeq$27 ppm) total uranium is assigned. Previous studies (e.g., Richard et al., 2012; Raffensperger and Garven, 1995b) reveal that the concentration of 1×10^{-4} mol/L represents an average aqueous uranium concentration found in fluid inclusions of the URU deposits. For this unit, oxidizing (Log *f*O2 =-22.825) and acidic (pH=5.131) conditions are assigned (based on previous study by Raffensperger and Garven, 1995b). The confining unit is conjectured to be carbonate-rich shale which is mainly composed of calcite, quartz, and kaolinite along with some other minerals. In comparison with the sandstone unit, this unit is in a more oxidizing condition (Log fO_2 =-14.763), and it is in a more or less similar acidic (pH=5.290) condition (Raffensperger and Garven, 1995b).

Based on previous studies (Raffensperger and Garven, 1995b; Gelhar et al., 1992), the longitudinal and transverse dispersion coefficients of 300 m and 30 m are considered, respectively. The molecular diffusion coefficient of 1×10^{-9} m^2/s is assigned to all aqueous

species, representing the average diffusion coefficient for anions and cations in water (Li and Gregory, 1974).

2.3 Simulation approach

In this study, numerical modeling is carried out using the non-isothermal multi-component reactive fluid flow and geochemical transport code TOUGHREACT (Xu and Pruess, 1998, 2001). TOUGHREACT's capabilities in simulating fluid flow, heat and reactive mass transport, and solution techniques for the governing equations (Appendix 1) have been discussed in detail by Xu and Pruess (2001) and Xu et al. (2004a). The code has been successfully applied to describe related processes including supergene copper enrichment (Xu et al., 2001), mineral alteration in hydrothermal systems (Xu and Pruess, 2001; Xu et al., 2004b), and mineral precipitation/dissolution in plug-flow and fracture-flow experiments under boiling conditions (Dobson et al., 2004).

The finite Difference Method (FDM) and Finite Element Method (FEM) are the most widely used methods in hydrogeologic modeling. Each of these methods has its own advantages and disadvantages. The FDM benefits from the simplicity of the theory, the algorithm, and easiness of application. However, due to the strict use of rectangular grids, the refinements of grid and geometry representation are inefficient in this method. The FDM is also not capable of representing the anisotropic properties of the medium. In addition, the FDM suffers from standard method for applying the Neumann Boundary condition; so it is often implemented indirectly using the wells. In FEM, implementing the local grid refinement (adaptive mesh generation) and representation of the spatial variation of anisotropy is easier than FDM due to non rectangular grids. It also benefits

from good accuracy and stability capabilities. However, this method is computationally time consuming and relatively cumbersome in application (Rozos and Koutsoyiannis, 2005). TOUGHREACT employs the Integral Finite Differences (IFD) (Narasimhan and Witherspoon, 1976), a finite volume method (Moridis, 2016). The IFD has the same advantages of FDM, and is characterized by flexible discretization that allows the use of irregular unstructured grids for complex geologic media. These features allow IFD (Appendix 1) to be much faster than the FDM and FEM methods, which makes this method advantageous in the applications where computational time is critical (Rozos and Koutsoyiannis, 2005). In Toughreact, time is discretized fully implicitly as a first-order backward finite difference. The code uses a sequential iteration approach, which solves the transport and the reaction equations separately. After solving the flow equations in each time step, the fluid velocities and phase saturations are used for the chemical transport simulation. Chemical transport is then solved on a component-by-component basis. The resulting concentrations obtained from solving the transport equations are substituted into the chemical reaction model. The system of chemical reaction equations is solved on a grid block by grid block (or element) basis by the Newton-Raphson iteration (Parkhurst et al., 1980; Reed, 1982; Wolery, 1992; Xu et al., 2004a).

In order to solve the fluid flow and heat transport equations accurately, careful attention needs to be given to issues of space discretization and time step. Therefore, independency of the solution on the grid and time step size was tested via running the model for a short time (100,000 years) using various grid and time step sizes, according to the Pecklet ($P_e \leq 2$) and Courant ($C \leq 1$) criteria. First, a coarse grid size of 600 m was selected and then mesh was refined using smaller size grids. It is found that the grid

size less than 100 m shows a good convergence, leading to more or less identical results for the fluid flow pattern and temperature distribution. Selection of a smaller grid size (e.g., 10-50 m) increases the running time of the model dramatically. Based on these numerical experiments, a grid size of 75 m was selected. Similarly, for selecting an appropriate time step size, various time steps were tested and the time step of 1200 seconds (20 minutes) was selected. An automatic time stepping scheme in TOUGHREACT allows to perform larger time steps (greater than 1200 s) towards the end of “quasistationary states" (QSS) (Lichtner, 1988). In this scheme, the time step is dependent on the convergence of the problem. If the system converges properly, the next time step size will increase; otherwise it will reduce automatically.

It is convenient to describe reversible chemical reactions conceptually using either a kinetic or equilibrium approach. The kinetic approach entails describing the temporal progress of the reaction and is usually based upon some model of the elementary reaction mechanisms (Simunek and Valocchi, 2002). Mathematically this leads to a system of ordinary differential equations. On the other hand, the equilibrium approach applies thermodynamic principles to describe the equilibrium state of the reaction (Simunek and Valocchi, 2002); this approach does not require a model for the reaction mechanism and mathematically leads to a system of nonlinear algebraic equations. Since groundwater and soil water are open systems that are subject to fluxes of mass and energy, it is more appropriate to adopt the concepts of “partial” and “local” equilibrium where thermodynamic equilibrium applies to certain subsets of reactions (Knapp, 1989; Bethke, 1996; Lichtner, 1996; Simunek and Valocchi, 2002). Several investigators have studied the question of when local equilibrium conditions apply in a dynamic transport system.

For example, Valocchi (1985, 1988) and Jennings (1987) studied adsorption processes. General reactions, including mineral precipitation and dissolution, were studied by Knapp (1989), Bahr (1990), and Lichtner (1996). These studies show that local equilibrium conditions apply when the chemical reaction rates are much faster than the rates of advection and dispersion processes. The dimensionless Damkohler number (D_a) represents the ratio of a chemical reaction rate to the advection and dispersion rate (Kuhn, 2004; Fogler, 2006). For the cases of $D_a \gg 1$ the solution approaches the equilibrium, and when $D_a < 1$ the local disequilibrium (kinetic) condition prevails (Steefel and Lasaga, 1990; Kuhn, 2004). In TOUGHREACT, aqueous complexation, acid-base, redox, gas dissolution/exsolution, and cation exchange reactions are considered under the local equilibrium assumption. This is due to the fact that rate of these reactions are much higher than the transport rate of the aqueous species involved in the reactions (Xu et al., 2004). The formulation of chemical equilibrium is similar to that by Parkhurst et al. (1980), Reed (1982), Yeh and Tripathi (1991), Wolery (1992), and Steefel and Lasaga (1994). The activity of aqueous species is equal to the product of the activity coefficient and molar concentration. Aqueous species activity coefficients are calculated from the extended Debye–Huckel (DH) equation (Helgeson and Kirkham, 1974) and activities of pure mineral phases and H_2O are assumed to be one. The DH model can deal with solutions having ionic strength from dilutes to moderately saline (up to 6 molal for an Nacl-dominant solution) (Xu and Pruess, 2001; Xu et al., 2004a). For highly saline formations and reservoirs the DH model cannot accurately calculate the activity coefficients of charged aqueous species, and it is required to calculate these coefficients using a more accurate Pitzer model (Pitzer, 1973, 1975). The Pitzer model is a semi-

empirical approach that combines the DH equation with additional terms considering the concentration dependence of the Gibbs energy for highly saline sediments (Kuhn, 2004). In this study, except for the anhydrite and calcite, the kinetic approach is considered for the dissolution and precipitation of the minerals presented in the system. The selection of the equilibrium approach for anhydrite and calcite is based on the fact that they have a typically quite rapid reaction rate (Baermann et al., 2000; Xu et al., 2004a) when they react with aqueous species. However, the chemical dissolution front instability (Zhao et al., 2008b, 2010) is not considered because of the limitation of using the TOUGHREACT code. For kinetically-controlled mineral dissolution and precipitation, TOUGHREACT considers a general form of the rate law (Steefel and Lasaga, 1994):

$$r_m = \pm k_m A_m \left|\left[\left(\frac{Q_m}{K_m}\right)^{\mu} - 1\right]\right|^{n} \tag{2.4}$$

where m is the mineral index, r_m is the dissolution/precipitation rate (positive values indicate dissolution, and negative values precipitation), A_m is the specific reactive surface area per kg of H_2O, k_m is the rate constant (moles per unit mineral surface area and unit time) which is temperature dependent, K_m is the equilibrium constant for the mineral-water reaction written for the destruction of one mole of mineral m, Q_m is the ion activity product, the exponents μ and n are two positive numbers normally determined by experiments, and are usually, but not always, taken equal to one (as in the present work). The temperature dependence of the reaction rate constant (k_m) is expressed via the Arrhenius equation (Lasaga, 1984; Steefel and Lasaga, 1994):

$$k = k_{25} \exp\left[\frac{-E_a}{R}\left(\frac{1}{T} - \frac{1}{298.5}\right)\right] \tag{2.5}$$

where E_a is the activation energy, k_{25} is the rate constant at 25°C, R is the gas constant, and T is the absolute temperature.

The primary thermodynamic database in TOUGHREACT is based on the EQ3/6 V7.2b database (Wolery, 1992). It contains reaction stoichiometries, dissociation constants (log (K)), and regression coefficients of log (K) as a function of temperature. However, it does not incorporate any uranium aqueous species and uranium minerals. In order to simulate uranium precipitation, we modified the existing thermodynamic database by adding aqueous uranium species (e.g., U^{3+}, U^{4+}, UCl^{3+}, UCl_2^{2+}, $UHCO_3^{3+}$, $U(HCO_3)_2^{2+}$, UO_2^{+}, $UO_2Cl(aq)$, $UO_2Cl_2^{-}$, $UO_2HCO_3(aq)$, $UO_2(HCO_3)_2^{-}$, $UO_2(CO_3)_2^{-2}$, UO_2Cl^{+}, $UO_2Cl_2(aq)$, $UO_2CO_3(aq)$, $UO_2HCO_3^{+}$, $UO_2(HCO_3)_2(aq)$, $UO_2HSO_4^{+}$, and $UO_2SO_4(aq)$) and uranium minerals (e.g., Uraninite, Rutherfordine) to it. The selection of these complexes is based on previous studies (Kojima et al., 1994; Raffensperger and Garven, 1995b) on URU deposits showing that uranyl chloride (e.g., UO_2Cl^{+}, $UO_2Cl_2(aq)$), uranyl carbonate (e.g., $UO_2CO_3(aq)$, $UO_2(CO_3)_2^{-2}$), and uranyl sulfates (e.g., $UO_2SO_4(aq)$) are the predominant uranium complexes in the Athabasca Basin.

To represent a geochemical system, it is convenient to select a subset of N_C aqueous species as primary species (or component or basis species). All other species are called secondary species that include aqueous complexes and minerals (Reed, 1982; Yeh and Tripathi, 1991; Steefel and Lasaga, 1994). The number of secondary species must be equal to the number of independent reactions. Generally, chemical components are defined as linearly independent chemical entities, such that every non-component species can be uniquely represented as a combination of these components, yet no component as a combination of other components (Xu et al., 2004a):

$$S_i = \sum_{J=1}^{N_c} v_{ij} S_j \qquad i = 1 \ldots N_R \tag{2.6}$$

where S represents chemical species, j is the basis species index, i is the secondary species index, N_R is the number of reactions (or secondary species), and v_{ij} is the stoichiometric coefficient of jth basis species in the i-th reaction.

Two different geochemical subsystems are considered in this study. In the first one (Appendix 2), uraninite precipitates involving methane as the reducing agent. The thermodynamic database for this geochemical subsystem includes 14 primary species, 46 secondary species and 20 minerals. H^+ is used as a primary species for variation in fluid pH associated with every layer. The second geochemical subsystem (Appendix 3) is based on the redox reaction for uraninite precipitation which does not involves methane. In this geochemical subsystem, methane has not been included as a primary species, and the thermodynamic database includes 14 primary species, 46 secondary species and 20 minerals. The reactions for the secondary species of the uranium and uraninite mineral are different from the first geochemical subsystem. Also, no methane will be produced by the alteration of graphite. In the second geochemical subsystem, water acts as a reductant and oxygen is used for formulating the redox reaction of uraninite precipitation by attributing the oxidizing potential to the dissolved oxygen (Nordstrom and Muñoz, 1986; Wolery, 1992). In contrast to the free electron in the hypothetical electron approach (Yeh and Tripathi, 1991), oxygen can be present and can be transported in natural subsurface flow systems (Xu et al., 2004a), implying that the aqueous oxygen is treated as a primary species in the system.

2.4 Results and discussion

2.4.1 Precipitation of uraninite by the first reducing mechanism

Fig. 2.2A shows the fluid flow regime around the faulted graphite zone at 370,000 years. The maximum flow rate of 5.53×10^{-8} m/s (about 1.7 m/year) occurs along this zone. Fluid flows through the faulted graphite zone into the basement and interacts with the basement rocks. Also, fluid in the basement uses this zone as a conduit to interact with the basin lithology. Fig. 2.2B depicts the fluid flow pattern throughout the model area at 370,000 years. Five convection cells develop in the entire sandstone unit. The flow rate within the sandstone unit (Fig. 2.2B) is about 1.1 m/year, which is in agreement with previous studies (e.g., Raffensperger and Garven, 1995a, b) on the URU deposits in the sedimentary basins. The simulated temperature distribution at 370,000 years is depicted in Fig. 2.2C, showing that temperature ranges from 120 to150 °C within the sandstone unit.

Based on the initial conditions specified for each hydrostratigraphic unit, uraninite precipitates in a small areas (150 m × 125 m), below the unconformity unit away from the faulted graphite zone, forming a basement-hosted ore body within 370,000 years (Fig. 2.3A). Although volume fraction of the precipitated uraninite is not high (about 0.003), as the time passes, more uraninite precipitates with a higher volume fraction (about 0.012) forming significant ore bodies in the basement. Figs. 2.3B, 2.3C, and 2.3D show the precipitation of uraninite from 400,000 years toward 600,000 years.

The results of our numerical simulation show that free convection within the sandstone unit leads to precipitation of significant quantities of uranium ore below the unconformity interface and away from faulted graphite zone within 500,000 years. The

volume fraction of precipitated uraninite (maximum volume fraction is 0.012) is equivalent to a uranium grade of 0.48 % which is comparable with the Rabbit Lake uranium deposit's grade with an average grade of 0.45 % (Raffensperger and Garven, 1995b) in the Athabasca Basin. In addition to those deposits that precipitate away from the fault, some minor uranium also mineralized beside the fault with a smaller volume fraction (about 0.003) which cannot be considered as an economic deposit due to its low grade (about 0.12 %).Uraninite precipitates in the areas when basinal fluids, that leached enough uranium from source rocks via the convection cells, interact with the reducing fluids in the basement or in the fault to provide the redox condition for precipitation of uraninite. Interaction of the uranyl (UO_2^{2+}) (Fig. 2.4A-D) with the aqueous methane (Fig. 2.4E-H) provides the redox condition for precipitation of uraninite. In addition, a suitable physicochemical condition (e.g., temperature, pH, and oxygen fugacity) is required for uranium mineralization. These parameters collectively control the deposition of the uranium from ore-forming brines (Peiffert et al., 1994, 1996; Bali, 2012). As can be seen from Fig. 2.3A and Fig. 2.2C, uraninite starts to precipitate when the temperature of ore-forming brines reaches about 180 °C, which is in agreement with the temperature measured in fluid inclusions of URU deposits (Kotzer, and Kyser, 1995; Renac et al., 2002; Derome et al., 2005; De Veslud et al., 2009; Richard et al., 2012). It should be added that the temperature of ore-forming brines in the locals that uraninite precipitates drops from 200 °C (initial temperature) to 180 °C. This change in temperature promotes the uraninite precipitation. As the time passes, the temperature of these brines further drops, which affects both the size and grade of the uraninite. At 500, 000 years, the temperature reaches 160 °C and consequently uraninite precipitates with a higher volume

fraction (0.012). This confirms the previous findings (e.g. Derome et al., 2005; Wilde and Wall, 1987; Wilde et al., 1989; Raffensperger and Garven, 1995b) that the temperature drop is a key factor in uranium deposition.

PH of the ore-forming brines within the modeled area (Fig. 2.5A-D) shows that a pH of 4-4.5 is in the favor of forming URU deposits, which is in agreement with previous studies (Wilde et al., 1985, 1989; Richard et al., 2012).

In addition to temperature and pH, reduction of oxygen fugacity, resulted from the interaction of oxidized uranium-bearing fluids with reductants, also contributes to precipitation of uraninite. It should be noted that the fugacity concept is not restricted to gases. For liquids and solids, the fugacity of the constituents in the condensed phase would evidently be approximately equal to their partial pressures in the vapor phase (Anderson and Crerar, 1993):

$$fO_2 \approx P \tag{2.7}$$

where P is partial pressure of the gas and fO_2 is oxygen fugacity.

It was found by Henry (1803) that the amount of gas that dissolved in a liquid in contact with it was directly proportional to the partial pressure of the gas (Anderson and Crerar, 1993). Thus

$$P_i = h_i . X_i \tag{2.8}$$

where P_i is the partial pressure of the gas i, X_i is the mole fraction of i in the liquid, and h_i is a constant (the Henry's law constant) which varies with temperature and with the nature of the gas i and the solvent. According to this rule, the variation in the mole fraction of oxygen in the liquid (aqueous oxygen) could be used as an indicator for

variation of oxygen fugacity in the system. Fig. 2.5E shows the variation of oxygen fugacity at 370,000 years throughout the model. There is a moderate decrease on the oxygen fugacity in right side of the basement, and uraninite precipitates with a low volume fraction of 0.003. The dominant downwelling flow in right side of the model area allows the oxidized uranium bearing brine to interact with reducing fluid of the basement, leading to the reduction of oxygen fugacity below the unconformity interface and away from the faulted graphite zone. It should be added that a minor reduction of oxygen fugacity also occurs in the vicinity of the faulted graphite zone wherein the oxidized basinal brine flow into the basement via this zone. Within 400,000 years (Fig. 2.5F), there is a further decrease in oxygen fugacity on the right side of the basement, and consequently uraninite precipitates with a higher volume fraction (about 0.01). This is in agreement with the new finding by Cuney (2009) which states that precipitation of uranium in most deposits is related to a decrease in oxygen fugacity as a result of interaction of oxidized uranium-bearing fluids with reductants (uranium solubility is favored by basinal brines with a high oxygen fugacity). Figs. 2.5G and 2.5H show the variation of oxygen fugacity at 500,000 and 600,000 years, respectively. Variation of oxygen fugacity at these times causes the precipitation of some minor uranium ores in addition to those that were deposited at earlier time (Fig 2.5F). Although dissolution of the graphite zone provides methane which acts as a reducing agent for the reduction of uraninite (refer to reactions 2.1 and 2.2), the lowest oxygen fugacity does not occur along this zone. This is due to the fact that fluid flow transports methane to other areas of the model. In addition, oxygen fugacity in the graphite zone can be affected by other

reactions in this zone such as muscovite and k-feldspar dissolution or precipitation along this zone.

Hydrothermal fluids passing through rocks cause alteration, precipitation, or dissolution of minerals, which changes the composition of the rocks (Zhao et al., 2008a, 2009). Mineralogic changes accompanying ore formation generate alteration halos associated with unconformity-related uranium ores. Minerals most commonly associated with these alteration halos include muscovite, chlorite, quartz, hematite, and pyrite. At 500,000 years, muscovite precipitation (Fig. 2.6A) has formed an alteration halo on both sides of the graphite zone and along the unconformity surface. K-feldspar (Fig. 2.6B) mainly dissolves below the unconformity. Both hematite (Fig. 2.6C) and magnetite (Fig. 2.6D) precipitate due to dissolution of pyrite below the unconformity (Fig. 2.6E) which provides ferrous into solution required for precipitation of hematite and magnetite. Chlorite (Fig. 2.6F) is subject to dissolution below the unconformity, whereas kaolinite (Fig. 2.6G) precipitates along the unconformity and within the cover unit. Graphite (Fig. 2.6H) dissolves along the faulted graphite zone and provides methane into solution to reduce the uranyl which leads to precipitation of uraninite. Other minerals present in the geochemical system also reveal some precipitation and dissolution pattern with time (not shown here).

2.4.2 Precipitation of uraninite by the second reducing mechanism

In the simulation with the second reducing mechanism, five convection cells develop in the entire sandstone unit as in the previous model. The basinal fluids enter through the

faulted graphite zone into the basement to interact with the basement lithology, and fluids in the basement use the faulted graphite zone as a pathway to mix with basinal brines.

Through the second reducing mechanism, uraninite precipitates relatively late (beginning at 395,000 years) in comparison with the first mechanism. As shown in Fig. 2.7A, uranium precipitates below the unconformity interface in the basement after 395,000 years. Figs. 2.7B, 2.7C, and 2.7D show the precipitated uranium deposits at 400,000, 500,000, and 600,000 years, respectively. Although uraninite cannot precipitate with a significant volume fraction until 500,000 years, after this time it precipitates with the considerable volume fraction of about 0.008 (Fig. 2.7D) which is equivalent to a uraninite grade of 0.3 %. The grade of precipitated uraninite by the second mechanism is higher than world average grade (0.2 %, Aben Resources Ltd; World Nuclear Association) and comparable with some unconformity uranium deposits in Canada and Australia (e.g., Collins Bay deposit with a uranium grade of 0.25 %; Jabiluka deposit with a grade of 0.3 %; Ranger deposit with a grade of 0.2 %; Koongarra deposit with a grade of 0.3 %; Raffensperger and Garven, 1995b). Simulation results confirm that the precipitation of uraninite can occur, once again below the unconformity interface and away from the faulted graphite zone, in the absence of methane as the reducing agent. This result can be important for exploration sectors, and explains why some uranium deposits are not associated with graphite, a question that has been asked by the exploration companies for a long time.

In addition to those deposits that precipitate below the unconformity interface in right side of the basement, some minor uranium also deposited in the right side of confining unit with very small volume fractions; but, their grade (0.04 %) is negligible

and they do not have an economic value. These deposits never developed as a high grade uraninite because there were not favorable physicochemical conditions for their precipitation.

Fig. 2.8 shows the pH regime and variations of oxygen fugacity at 395,000, 400,000, 500,000, and 600,000 years. Along with other physicochemical parameters such as a temperature range of about 160-180 ℃ and a pH range of about 4-4.5 (Fig. 2.8A-D), reduction of oxygen fugacity on right side of the basement (Fig. 2.8E-H) provides a suitable condition for precipitation of uraninite. As we disused earlier, these parameters (and their change with time) collectively control the precipitation of uraninite and the deposition of uranium is limited to these areas.

The role of a faulted graphite zone cannot be ignored in serving as a pathway for the fluids to interact with the basement and basin lithologies. This result is in agreement with the recent insights about the potential reducing mechanism of URU deposits (e.g., Alexandre et al., 2005; Yeo and Potter, 2010) that uraninite can precipitate without involving methane as a reductant.

Our numerical simulation results confirm that by employing either reducing mechanism, uraninite can precipitate below the unconformity interface away from a faulted graphite zone regardless of the reducing agent involved in precipitation of it. The alteration of the graphite, which provides methane as a reducing agent, is not required for uraninite precipitation. It is clear that in both mechanisms, mineralization of URU deposits is controlled by physicochemical conditions such as temperature, pH, and reduction of oxygen fugacity. As we discussed earlier, a temperature range of around 160-180 ℃ is required for uranium mineralization. In addition to the temperature, a pH

range of 4-4.5 and a decrease in oxygen fugacity have a profound impact on precipitation of uraninite. Although uraninite can precipitate with the second reducing mechanism (water as a reductant), in comparison with the first reducing mechanism (methane as a reductant) a longer time is required for the precipitation of the uraninite. Also, the volume fraction of precipitated uraninite through the second mechanism (volume fraction about 0.008) is less than the volume fraction of the precipitated uraninite by the first mechanism (volume fraction about 0.012). This means that methane as an organic matter is a better reducing agent for the precipitation of the uraninite.

As the same computation shows, because of the mineralogic changes accompanying the ore formation, the precipitation of muscovite, hematite, magnetite, and kaolinite form alteration halos on both sides of the faulted graphite zone and along the unconformity surface and dissolution of K-feldspar, pyrite, chlorite occur below the unconformity interface (Fig 2.9).

2.5 Conclusions

Reactive mass transport modeling has been carried out in order to evaluate the role of a faulted graphite zone in the formation of URU deposits. Two different reducing mechanisms have been considered for the precipitation of uranium. The first one involves methane, produced by the dissolution of the graphite zone, as the reducing agent, and the second one does not involve methane as the reducing agent, and oxygen is used for formulating the redox reaction of uraninite precipitation. Either reducing mechanisms lead to the precipitation of uraninite in the basement close to the unconformity and away from faulted graphite zone. Physicochemical parameters collectively control the uranium

mineralization. Uranium mineralization occurs in locales experiencing a reduction of oxygen fugacity, and having a temperature of 160-180 ^{o}C and a pH of 4-4.5. Through the second reducing mechanism, a longer time is required for the precipitation of the uraninite, and the volume fraction of the precipitated uraninite is lower than that by the first mechanism.

Our numerical simulations confirm that uraninite can precipitate away from the faulted graphite zone even if methane is not involved as reducing agent. The methane, which could be produced by hydrothermal alteration of graphite, is not required for uraninite precipitation. Mineralogic changes accompanying ore formation produce alteration halos associated with unconformity-related uranium ores. Most importantly, muscovite shows both dissolution and precipitation pattern below the unconformity, whereas k-feldspar only dissolves below the unconformity. Hematite and magnetite are mainly subject to precipitation along the unconformity and within the basement. Pyrite and chlorite present dissolution regime below the unconformity. Kaolinite, as a gangue mineral, precipitates in the cover and along the unconformity. It should be noted that graphite dissolves along the fault and provides methane into the solution. The alteration of the graphite, which provides methane, is not required for uraninite precipitation. These results can be important for exploration companies and provide some insights for exploration of the uranium ore deposits. Exploration geophysicists consider the graphite zone as an indicator for existence of URU deposits since they assume that uranium ore deposits are associated with the graphite zone. They use electromagnetic methods, which are sensitive to conductive zones such as a graphite zone, for localization of uraninite. Our simulation results suggest that they should also investigate the altered minerals (e.g.,

muscovite and chlorite, k-feldspar, pyrite, hematite, and magnetite) which form as a result of diagenetic changes during uranium ore mineralization.

The faulted graphite zone is still important in that it serves as a pathway for the fluids to interact with the basement and basin lithologies. The uranium bearing brines flow into the faulted graphite zone and interact with the basement lithology. Also, fluids in the basement use the faulted graphite zone as a conduit to mix with the basinal fluids. Maximum fluid flow rates take place along the faulted graphite zone due to its higher permeability in comparison with that of the other stratigraphic units present in the model.

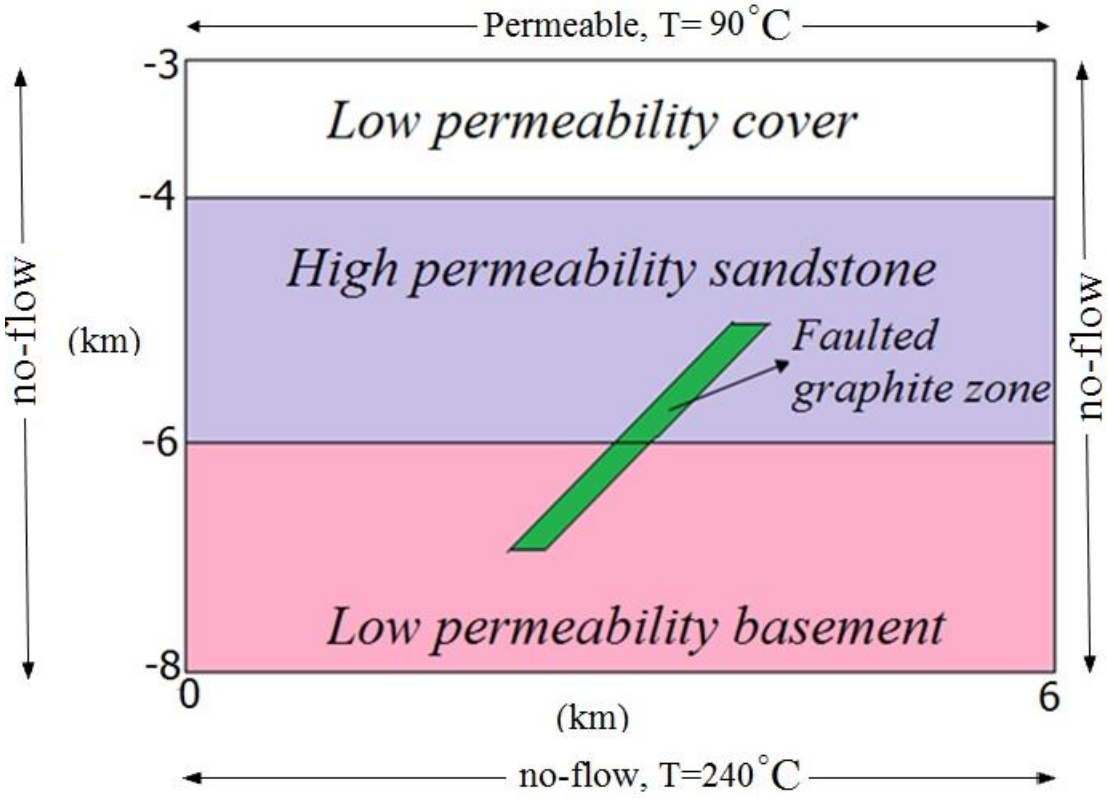

Fig. 2.1. Conceptual model used in the simulation of URU deposits (based on previous studies by Cui et al., 2012 and Raffensperger and Garven, 1995b).

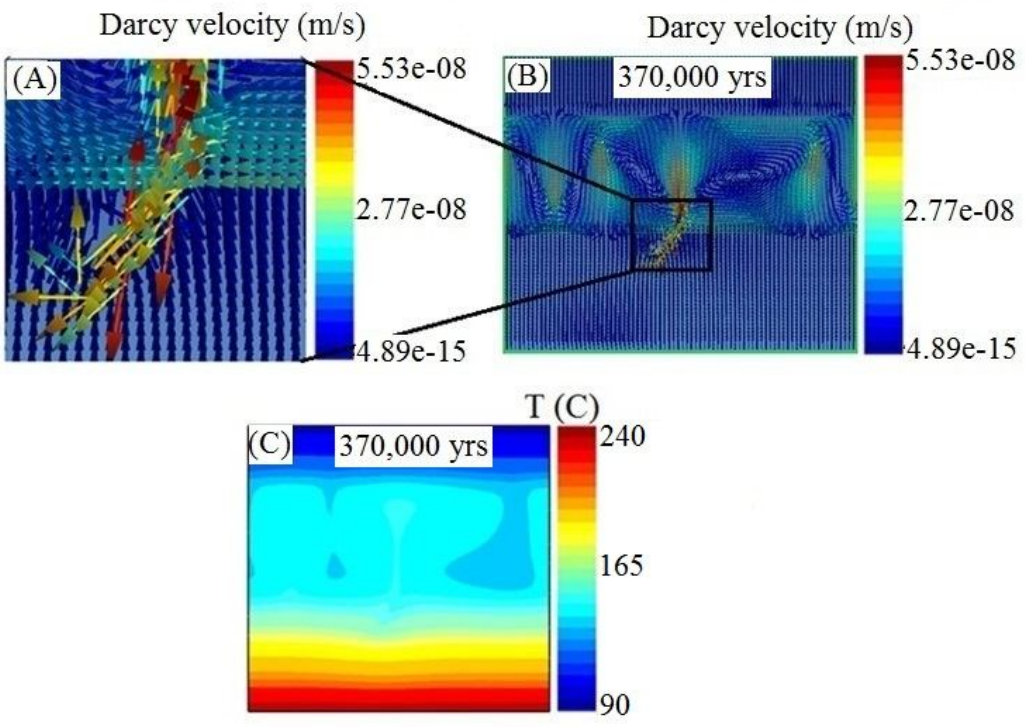

Fig. 2.2. Fluid flow pattern, flow rate, and temperature distribution for the first reducing mechanism (methane as a reductant) at 370,000 years. (A) expanded view of fluid flow regime around the faulted graphite zone, (B) fluid flow pattern and flow flow rate throughout the model area, and (C) temperature distribution.

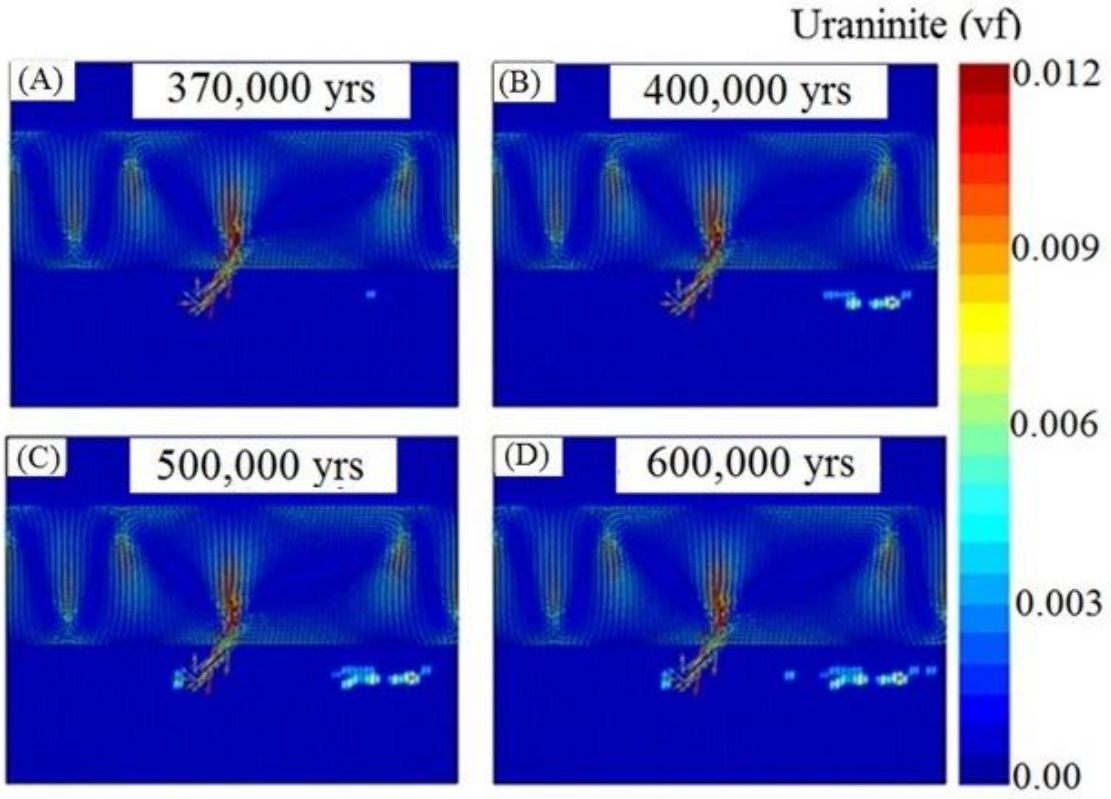

Fig. 2.3. Precipitated uraninite for the first reducing mechanism (methane as a reductant) at different times. (A) at 370,000 years, (B) at 400,000 years, (C) at 500,000 years, and (D) at 600,000 years.

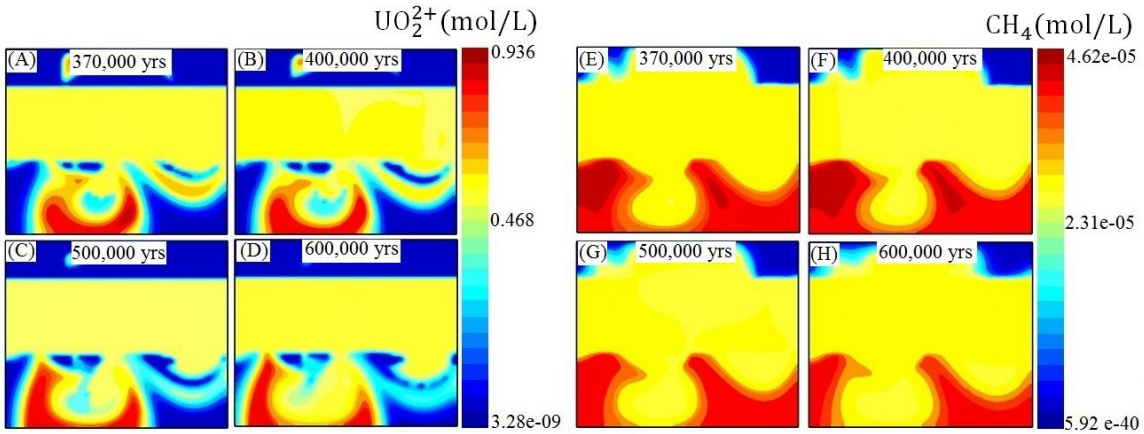

Fig. 2.4. Concentration of uranyl and methane for the first reducing mechanism (methane as a reductant) at different times. (A-D) concentration of uranyl, and (E-H) concentration of methane.

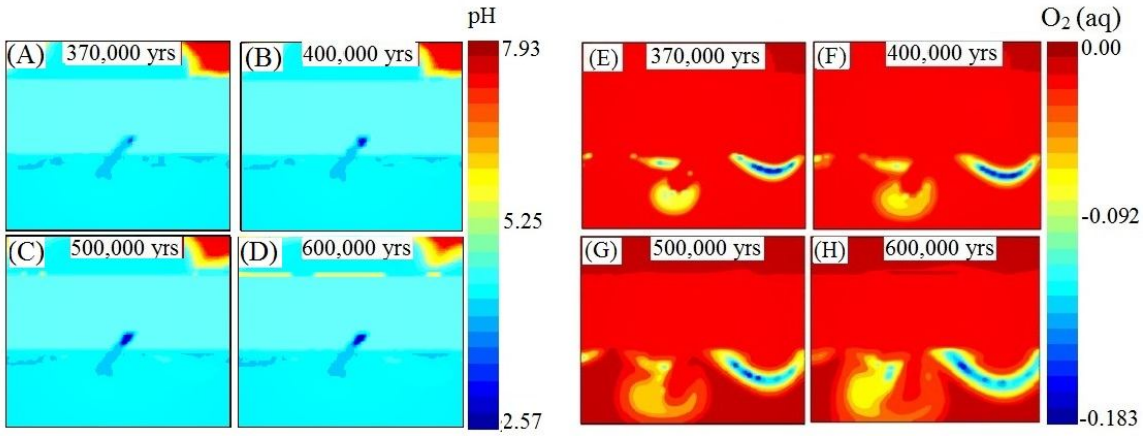

Fig. 2.5. PH and variations of the oxygen fugacity for the first reducing mechanism (methane as a reductant) at different times. (A-D) pH regime, and (E-H) oxygen fugacity variations. Negative values in the legend correspond to a decrease in oxygen fugacity and positive values correspond to an increase in oxygen fugacity.

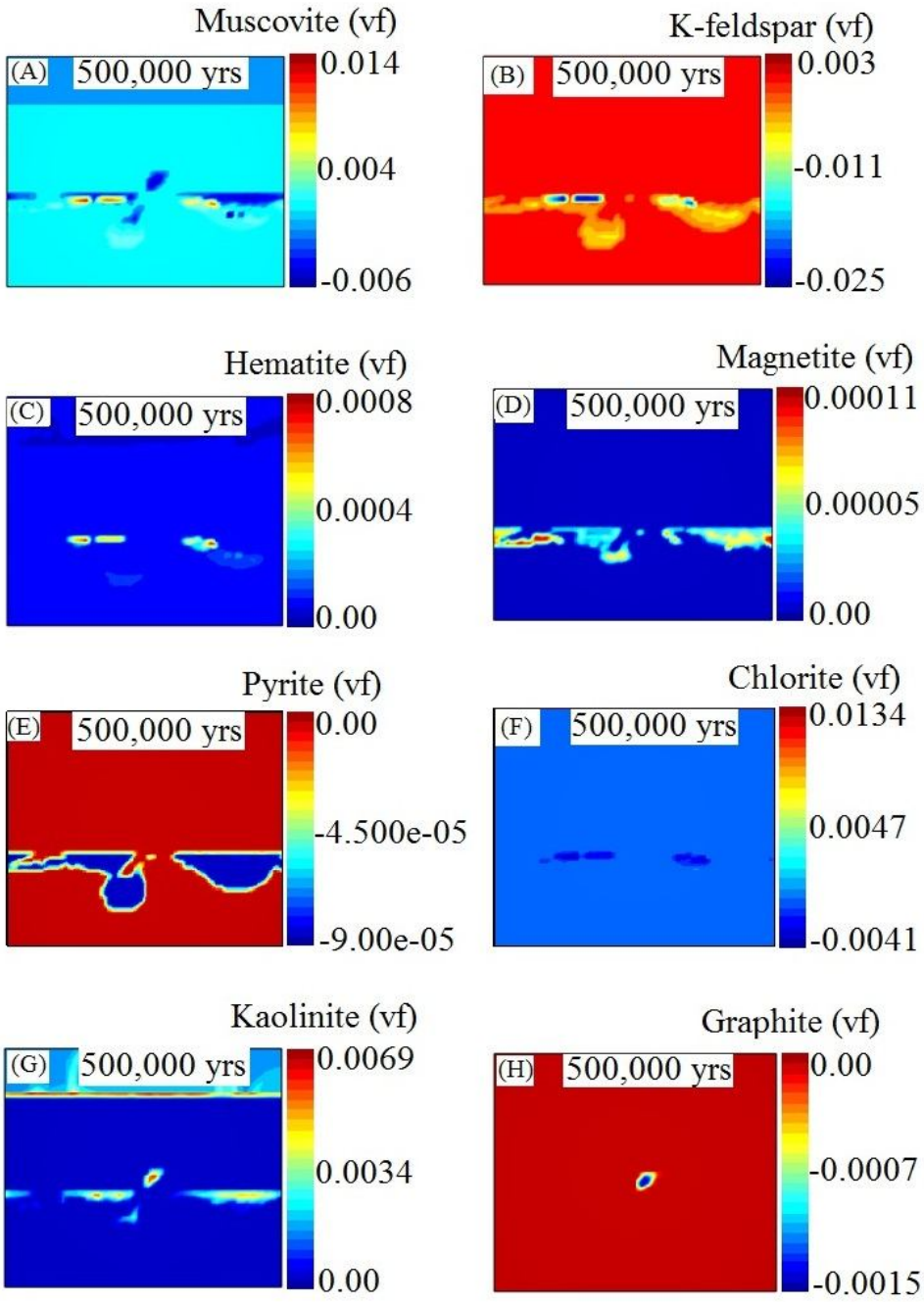

Fig. 2.6. Precipitation and dissolution of minerals at 500,000 years corresponding to first reducing mechanism (methane as a reductant). (A) muscovite alteration, (B) k-feldspar dissolution, (C-D) precipitation of hematite and magnetite, (E-F) dissolution of Pyrite and chlorite, (G) kaolinite precipitation, and (H) graphite dissolution. Positive values in the legend refer to the precipitation, and negative ones refer to the dissolution of the mineral.

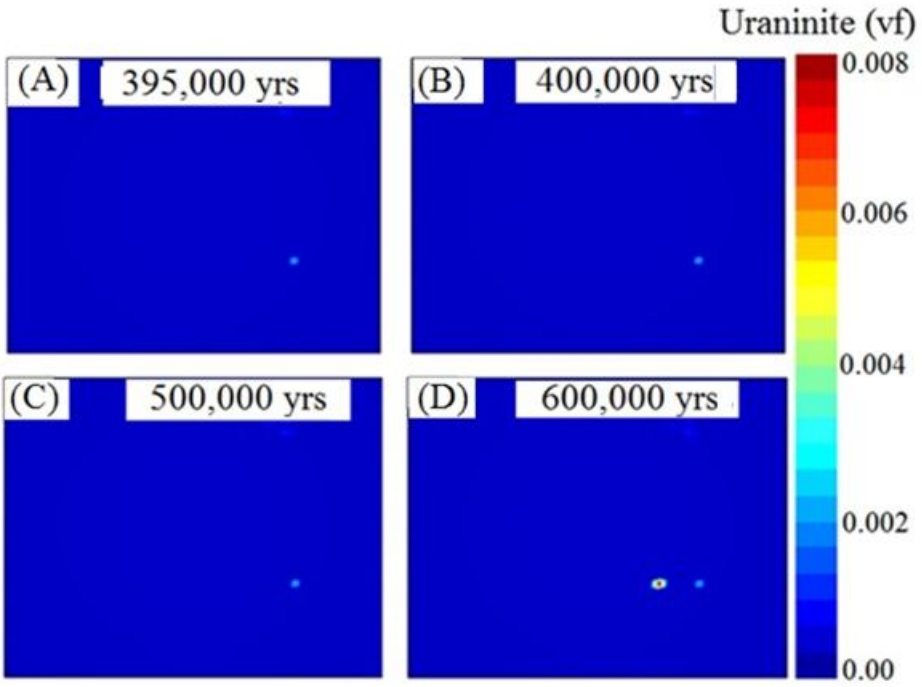

Fig. 2.7. Precipitated uraninite corresponding to second reducing mechanism (water as a reductant) at different times. (A) at 395,000 years, (B) at 400,000 years, (C) at 500,000 years, and (D) at 600,000 years.

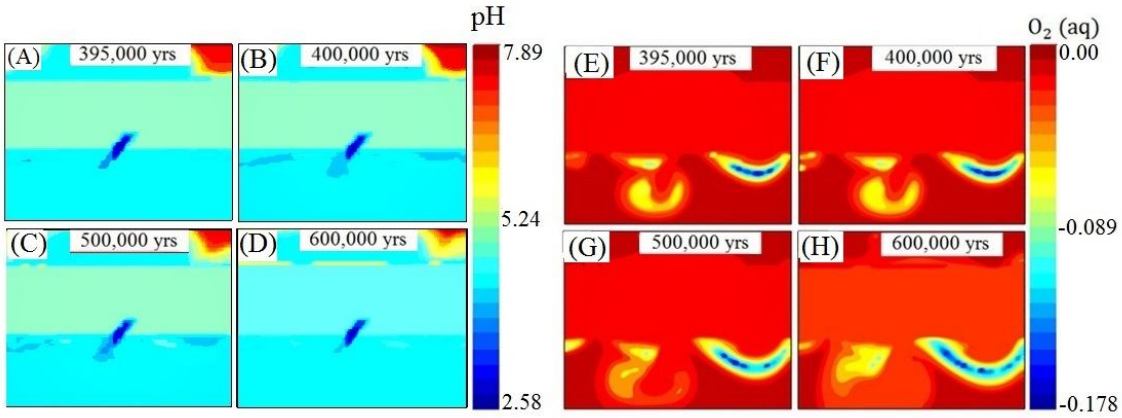

Fig. 2.8. Variations of pH and oxygen fugacity for the second reducing mechanism (water as a reductant) at different times. (A-D) pH regime, and (E-H) oxygen fugacity variations. Negative values in the legend correspond to a decrease in oxygen fugacity and positive values correspond to an increase in oxygen fugacity.

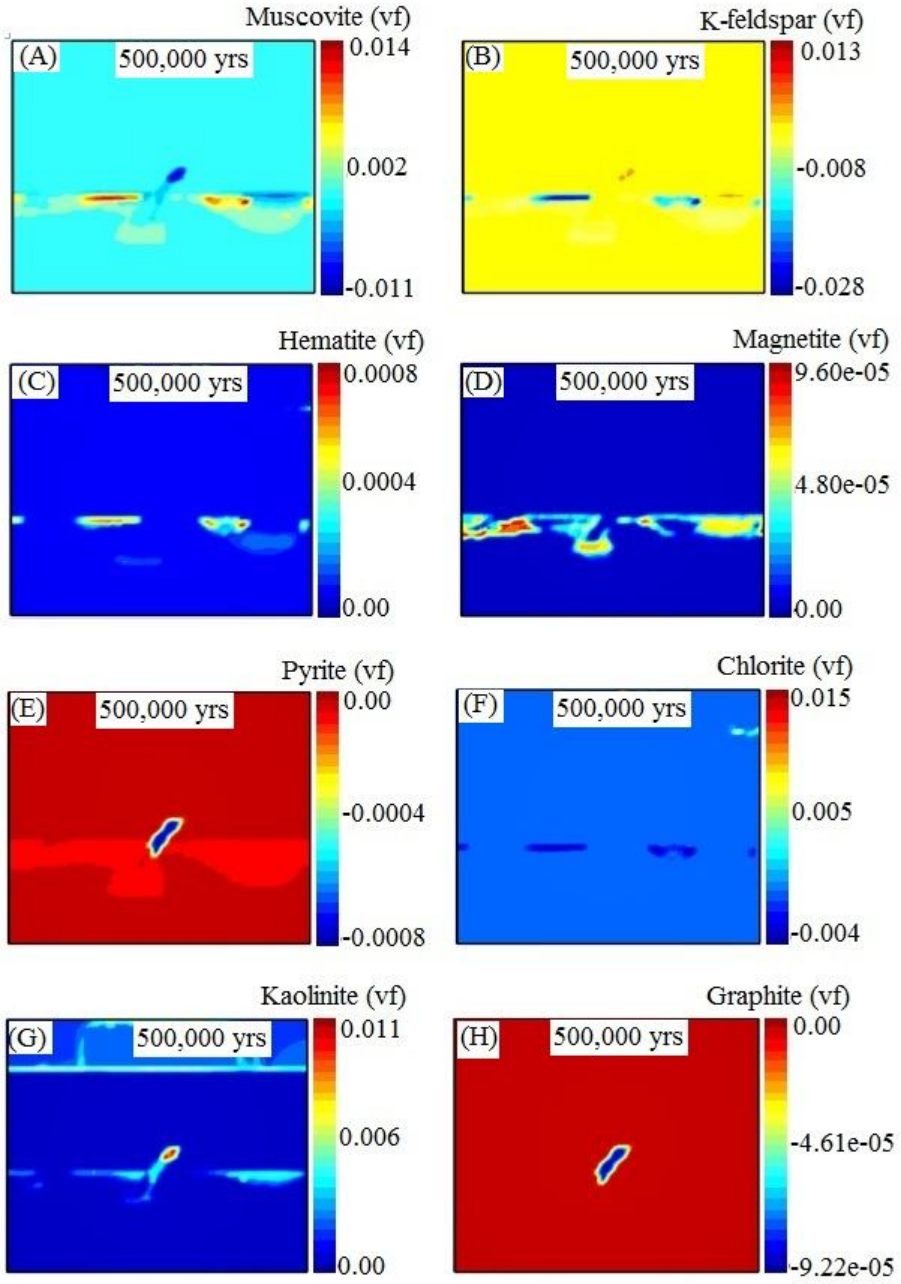

Fig. 2.9. Precipitation and dissolution of minerals at 500,000 years corresponding to second reducing mechanism (water as a reductant). (A) muscovite alteration, (B) k-feldspar dissolution (C-D) precipitation of hematite and magnetite, (E-F) dissolution of Pyrite and chlorite, (G) kaolinite precipitation, and (H) graphite dissolution. Positive values in the legend refer to the precipitation, and negative ones refer to the dissolution of the mineral.

Table 2.1. Major physical properties of various hydrostratigraphic units (based on previous studies by Freeze and Cherry, 1979; Garven and Freeze, 1984; Raffensperger and Garven, 1995a, b; Mclellan et al., 2004; Yang et al., 2004; Oliver et al., 2006; Cui et al., 2012a).

Property	**Confining unit**	**Sandstone unit**	**Basement unit**	**Faulted graphite zone**
Density (kg/m^3)	2400	2500	2650	2400
Porosity	0.15	0.2	0.1	0.2
Permeability (m^2)	1×10^{-15}	3×10^{-13}	3×10^{-16}	1×10^{-12}
Thermal conductivity (W/(m.°C))	2.5	3.5	2.5	4
Specific heat capacity (J/(kg.°C))	803	803	803	803
Pore fluid compressibility (1/Pa)	3.6×10^{-11}	3.1×10^{-11}	2.0×10^{-11}	4.3×10^{-11}
Pore fluid expansivity (1/°C)	8.0×10^{-6}	1.0×10^{-5}	8.0×10^{-6}	1.0×10^{-5}

Table 2.2. Initial condition of the aqueous phase associated with the basement unit (based on previous study on URU deposits by Raffensperger and Garven, 1995b).

Component Species	Concentration (mol/L)
AlO_2^-	0.1
Ca^{2+}	0.853
$CH_4^0(aq)$	1.0
Cl^-	2.7
Fe^{2+}	0.002
H^+	2.8774×10^{-5}
H_2O	1.0
HCO_3^-	0.049
K^+	0.163
Mg^{2+}	0.365
Na^+	0.1
$O_2(aq)$	1.4655×10^{-47}
$SiO_2(aq)$	1.0
SO_4^{2-}	5.6×10^{-4}
UO_2^{2+}	8.2×10^{-11}

Table 2.3. Initial mineral volume fractions, possible secondary mineral phases, and their kinetic properties associated with the basement unit (K25: kinetic rate constant at 25°C, Ea: activation energy and Am: reactive surface area; based on previous study on URU deposits by Raffensperger and Garven, 1995b).

Mineral	**Composition**	**Volume Fraction**	**K_{25} (mol/m^{2}s)**	**E_a (kJ/mol)**	**A_m (cm^2/g)**
Primary:					
Anhydrite*	$CaSO_4$	0.0032	equilibrium	equilibrium	equilibrium
Chlorite	$(Mg_{2.5}Fe_{2.5})Al_2Si_3O_{10}(OH)_8$	0.0056	1×10^{-13}	62.76	151.6
Hematite	Fe_2O_3	0.0005	2.514×10^{-15}	66.2	12.87
K-feldspar	$KAlSi_3O_8$	0.0494	1×10^{-12}	67.83	9.8
Muscovite	$KAl_2(AlSi_3O_{10})(OH)_2$	0.3263	1×10^{-13}	62.76	151.6
Pyrite	FeS_2	0.0001	1×10^{-11}	62.76	12.87
Quartz	SiO_2	0.5148	1.258×10^{-14}	87.5	9.8
Secondary:					
Albite	$NaAlSi_3O_8$	0	1×10^{-12}	67.83	9.8
Anorthite	$CaAl_2Si_2O_8$	0	1×10^{-12}	67.83	9.8

Calcite*	$CaCO_3$	0	equilibrium	equilibrium	equilibrium
Dolomite	$CaMg(CO_3)_2$	0	2.951×10^{-8}	52.2	9.8
Graphite	C	0	1×10^{-12}	67.83	9.8
Halite	NaCl	0	1×10^{-13}	67.83	9.8
Kaolinite	$Al_2Si_2O_5(OH)_4$	0	1×10^{-13}	62.76	151.6
Magnesite	$MgCO_3$	0	4.571×10^{-10}	23.5	9.8
Magnetite	Fe_3O_4	0	1×10^{-13}	67.83	12.87
Siderite	$FeCO_3$	0	1.26×10^{-9}	62.76	9.8
Sylvite	KCl	0	1×10^{-12}	67.83	9.8
Rutherfordine	UO_2CO_3	0	1×10^{-13}	67.83	9.8
Uraninite	UO_2	0	1×10^{-13}	67.83	9.8
Porosity	-	0.1	-	-	-

*Anhydrite and calcite were assumed to react with aqueous species at equilibrium because their reaction rate is typically quite rapid (Xu et al., 2004a). Dissolution and precipitation of other minerals are kinetically controlled.

Table 2.4. Initial condition of the aqueous phase associated with the faulted graphite unit (based on previous study on URU deposits by Raffensperger and Garven, 1995b).

Component Species	Concentration (mol/L)
AlO_2^-	0.1
Ca^{2+}	0.1
$CH_4^0(aq)$	4.0
Cl^-	3
Fe^{2+}	0.0005
H^+	8.0538×10^{-5}
H_2O	1.0
HCO_3^-	1.2×10^{-4}
K^+	0.038
Mg^{2+}	0.88
Na^+	1.0
$O_2(aq)$	5.188×10^{-52}
$SiO_2(aq)$	0.5
SO_4^{2-}	0.0010
UO_2^{2+}	1.6×10^{-6}

Table 2.5. Initial mineral volume fractions, possible secondary mineral phases, and their kinetic properties associated with the faulted graphite unit (based on previous study on URU deposits by Raffensperger and Garven, 1995b).

Mineral	Composition	Volume Fraction	K_{25} (mol/m^{2}s)	E_a (kJ/mol)	A_m (cm^2/g)
Primary:					
Graphite	C	0.0848	1×10^{-12}	67.83	9.8
Chlorite	$(Mg_{2.5}Fe_{2.5})Al_2Si_3O_{10}(OH)_8$	0.0011	1×10^{-13}	62.76	151.6
Kaolinite	$Al_2Si_2O_5(OH)_4$	0.0007	1×10^{-13}	62.76	151.6
Muscovite	$KAl_2(AlSi_3O_{10})(OH)_2$	0.4227	1×10^{-13}	62.76	151.6
Pyrite	FeS_2	0.001	1×10^{-11}	62.76	12.87
Quartz	SiO_2	0.2897	1.258×10^{-14}	87.5	9.8
Secondary:					
Anhydrite	$CaSO_4$	0	equilibrium	equilibrium	equilibrium
Albite	$NaAlSi_3O_8$	0	1×10^{-12}	67.83	9.8
K-feldspar	$KAlSi_3O_8$	0	1×10^{-12}	67.83	9.8

Anorthite	$CaAl_2Si_2O_8$	0	1×10^{-12}	67.83	9.8
Calcite	$CaCO_3$	0	equilibrium	equilibrium	equilibrium
Dolomite	$CaMg(CO_3)_2$	0	2.951×10^{-8}	52.2	9.8
Hematite	Fe_2O_3	0	2.514×10^{-15}	66.2	12.87
Halite	NaCl	0	1×10^{-13}	67.83	9.8
Magnesite	$MgCO_3$	0	4.571×10^{-10}	23.5	9.8
Magnetite	Fe_3O_4	0	1×10^{-13}	67.83	12.87
Siderite	$FeCO_3$	0	1.26×10^{-9}	62.76	9.8
Sylvite	KCl	0	1×10^{-12}	67.83	9.8
Rutherfordine	UO_2CO_3	0	1×10^{-13}	67.83	9.8
Uraninite	UO_2	0	1×10^{-13}	67.83	9.8
Porosity	-	0.2	-	-	-

Table 2.6. Initial condition of the aqueous phase associated with the sandstone unit (based on previous study on URU deposits by Raffensperger and Garven, 1995b).

Component Species	Concentration (mol/L)
AlO_2^-	0.1
Ca^{2+}	1.502
$CH_4^0(aq)$	1.0
Cl^-	5
Fe^{2+}	2.6×10^{-11}
H^+	7.3961×10^{-6}
H_2O	1.0
HCO_3^-	1×10^{-4}
K^+	0.045
Mg^{2+}	0.477
Na^+	1.0
$O_2(aq)$	1.4962×10^{-23}
$SiO_2(aq)$	5.0
SO_4^{2-}	1.5×10^{-3}
UO_2^{2+}	1.0×10^{-4}

Table 2.7. Initial mineral volume fractions, possible secondary mineral phases, and their kinetic properties associated with the sandstone unit (based on previous study on URU deposits by Raffensperger and Garven, 1995b).

Mineral	Composition	Volume Fraction	K_{25} (mol/m^{2}s)	E_a (kJ/mol)	A_m (cm^2/g)
Primary:					
Hematite	Fe_2O_3	0.0114	2.514×10^{-15}	66.2	12.87
Anhydrite	$CaSO_4$	0.0058	equilibrium	equilibrium	equilibrium
K-feldspar	$KAlSi_3O_8$	0.1201	1×10^{-12}	67.83	9.8
Chlorite	$(Mg_{2.5}Fe_{2.5})Al_2Si_3O_{10}(OH)_8$	0.0003	1×10^{-13}	62.76	151.6
Muscovite	$KAl_2(AlSi_3O_{10})(OH)_2$	0.0183	1×10^{-13}	62.76	151.6
Quartz	SiO_2	0.6442	1.258×10^{-14}	87.5	9.8
Secondary:					
Albite	$NaAlSi_3O_8$	0	1×10^{-12}	67.83	9.8
Graphite	C	0	1×10^{-12}	67.83	9.8
Kaolinite	$Al_2Si_2O_5(OH)_4$	0	1×10^{-13}	62.76	151.6

Anorthite	$CaAl_2Si_2O_8$	0	1×10^{-12}	67.83	9.8
Calcite	$CaCO_3$	0	equilibrium	equilibrium	equilibrium
Dolomite	$CaMg(CO_3)_2$	0	2.951×10^{-8}	52.2	9.8
Pyrite	FeS_2	0	1×10^{-11}	62.76	12.87
Halite	NaCl	0	1×10^{-13}	67.83	9.8
Magnesite	$MgCO_3$	0	4.571×10^{-10}	23.5	9.8
Magnetite	Fe_3O_4	0	1×10^{-13}	67.83	12.87
Siderite	$FeCO_3$	0	1.26×10^{-9}	62.76	9.8
Sylvite	KCl	0	1×10^{-12}	67.83	9.8
Rutherfordine	UO_2CO_3	0	1×10^{-13}	67.83	9.8
Uraninite	UO_2	0	1×10^{-13}	67.83	9.8
Porosity	-	0.2	-	-	-

Table 2.8. Initial condition of the aqueous phase associated with the confining unit (based on previous study on URU deposits by Raffensperger and Garven, 1995b).

Component Species	Concentration (mol/L)
AlO_2^-	0.1
Ca^{2+}	2.8×10^{-2}
$CH_4^0(aq)$	0.1
Cl^-	0.1
Fe^{2+}	7.3×10^{-15}
H^+	5.1286×10^{-6}
H_2O	1.0
HCO_3^-	0.396
K^+	0.022
Mg^{2+}	0.0026
Na^+	0.1
$O_2(aq)$	1.7258×10^{-15}
$SiO_2(aq)$	1.0
SO_4^{-2}	1.5×10^{-2}
UO_2^{2+}	1×10^{-5}

Table 2.9. Initial mineral volume fractions, possible secondary mineral phases, and their kinetic properties associated with the confining unit (based on previous study on URU deposits by Raffensperger and Garven, 1995b)**.**

Mineral	**Composition**	**Volume Fraction**	**K_{25} (mol/m^{2}s)**	**E_a (kJ/mol)**	**A_m (cm^2/g)**
Primary:					
Calcite	$CaCO_3$	0.4414	equilibrium	equilibrium	equilibrium
Dolomite	$CaMg(CO_3)_2$	0.0129	2.951×10^{-8}	52.2	9.8
Hematite	Fe_2O_3	0.0003	2.514×10^{-15}	66.2	12.87
Anhydrite	$CaSO_4$	0.0024	equilibrium	equilibrium	equilibrium
Kaolinite	$Al_2Si_2O_5(OH)_4$	0.2967	1×10^{-13}	62.76	151.6
Muscovite	$KAl_2(AlSi_3O_{10})(OH)_2$	0.0011	1×10^{-13}	62.76	151.6
Quartz	SiO_2	0.0952	1.258×10^{-14}	87.5	9.8
Secondary:					
Albite	$NaAlSi_3O_8$	0	1×10^{-12}	67.83	9.8
Graphite	C	0	1×10^{-12}	67.83	9.8

Chlorite	$(Mg_{2.5}Fe_{2.5})Al_2Si_3O_{10}($	0	1×10^{-13}	62.76	151.6
Anorthite	$CaAl_2Si_2O_8$	0	1×10^{-12}	67.83	9.8
K-feldspar	$KAlSi_3O_8$	0	1×10^{-12}	67.83	9.8
Pyrite	FeS_2	0	1×10^{-11}	62.76	12.87
Halite	$NaCl$	0	1×10^{-13}	67.83	9.8
Magnesite	$MgCO_3$	0	4.571×10^{-10}	23.5	9.8
Magnetite	Fe_3O_4	0	1×10^{-13}	67.83	12.87
Siderite	$FeCO_3$	0	1.26×10^{-9}	62.76	9.8
Sylvite	KCl	0	1×10^{-12}	67.83	9.8
Rutherfordine	UO_2CO_3	0	1×10^{-13}	67.83	9.8
Uraninite	UO_2	0	1×10^{-13}	67.83	9.8
Porosity	-	0.15	-	-	-

References

Aben Resources Ltd: www.abenresources.com/s/uranium.asp.

Adlakha, E.E., Hattori, K., Zaluksi, G., Kotzer, T., and Potter, E.G., 2014, Alteration within the basement rocks associated with the P2 fault and the McArthur River uranium deposit, Athabasca Basin: Geological Survey of Canada, Open File 7462. doi: 10.4095/293364.

Alexandre, P., Kyser, K., Thomas, D., Polito, P., and Marlat, J., 2009, Geochronology of unconformity-related uranium deposits in the Athabasca Basin, Saskatchewan, Canada and their integration in the evolution of the basin: Mineralium Deposita, v. 44, p. 41-59.

Anderson, G.M., and Crerar, D.A., 1993, Thermodynamics in geochemistry the equilibrium model: Oxford University Press.

Appold, M.S., and Garven, G., 2000, Reactive flow models of ore formation in the southeast Missouri Pb-Zn-Cu district: Economic Geology, v. 95, p. 1605-1626.

Atkins, P.W., and de Paula, J., 1993, The elements of physical chemistry (5th edition): Oxford University Press.

Awadh, S.M., Ali, K.K., and Alazzawi, A.T., 2013, Geochemical exploration using surveys of spring water, hydrocarbon and gas seepage, and geobotany for determining the surface extension of Abu-Jir Fault Zone in Iraq: A new way for determining geometrical shapes of computational simulation models: Journal of Geochemical Exploration, v. 124, p. 218-229.

Bahr, J.M., 1990, Kinetically influenced terms for solute transport affected by heterogeneous and homogeneous classical reactions: Water Resources Research, v. 26, p. 21-34.

Baermann, A., Kroger, J., Zarth, M., 2000, Anhydrite cement in Rhaetian sadstones in Hamburg: X-ray and NMR tomography studies and leaching tests: Zeitschrift fur angewandte Geologie, v. 46, p. 144-152.

Bali, E., 2012, Uranium-ore giants: Nature Geoscience, v. 5, p. 96-97.

Bethke, C.M., 1996, Geochemical reaction modeling-Concepts and applications: Oxford University Press.

Charifo, G., Almeida, J.A., and Ferreira, A., 2013, Managing borehole samples of unequal lengths to construct a high-resolution mining model of mineral grades zoned by geological units: Journal of Geochemical Exploration, v. 132, p. 209-223.

Chi, G., Bosman, S., and Card, C., 2013, Numerical modeling of fluid pressure regime in the Athabasca basin and implications for fluid flow models related to the unconformity-type uranium mineralization: Journal of Geochemical Exploration, v. 125, p. 8-19.

Cui, T., Yang, J., and Samson, I.M., 2012, Tectonic deformation and fluid flow: Implications for the formation of unconformity-related uranium deposits: Economic Geology, v. 107, p. 147-163.

Cuney, M., 2009, The extreme diversity of uranium deposits: Mineralium Deposita, v. 44, p. 3-9.

De Veslud, C.L.C., Cuney, M., Lorilleux, G., Royer, J.J., and Jébrak, M., 2009, 3D modeling of uranium-bearing solution-collapse breccias in Proterozoic sandstones

(Athabasca Basin, Canada)-Metallogenic interpretations: Computers & Geosciences, v. 35, p. 92-107.

Derome, D., Cathelineau, M., Cuney, M., Fabre, C., Lhomme, T., and Banks, D.A., 2005: Mixing of Sodic and Calcic Brines and Uranium Deposition at McArthur River, Saskatchewan, Canada: A Raman and Laser-Induced Breakdown Spectroscopic Study of Fluid Inclusions: Economic Geology, v.100, p. 1529-1545.

Dobson, P.F., Salah, S., Spycher, N., and Sonnenthal, E.L., 2004, Simulation of water-rock interaction in the Yellowstone geothermal system using TOUGHREACT: Geothermics, v. 33, p. 493-502.

Fayek, M., and Kyser, T.K., 1997, Characterization of multiple fluid-flow events and rare-earth-element mobility associated with formation of unconformity- type uranium deposits in the Athabasca Basin, Saskatchewan: Canadian Mineralogist, v. 35, p. 627-658.

Fogler, S., 2006, Elements of chemical reaction engineering (4th ed.). Upper Saddle River, NJ: Pearson Education.

Fuchs, H., and Hilger, W., 1989, Kiggavik (Lone Gull): An unconformity related uranium deposit in the Thelon Basin, Northwest Territories, Canada: Uranium Resources and Geology of North America: Proceeding of a Technical Committee Meeting, Saskatoon, p. 429-454.

Gow, P., Upton, P., and Hill, K., 2002, Copper-Gold mineralization in the New Guinea: numerical modeling of collision, fluid flow and intrusion-related hydrothermal system: Australian Journal of Earth Science, v. 49, p. 753-771.

He, W., Bao, Z., and Li, T., 1999, One-dimensional reactive transport models of alteration in the tongchang porphyry copper deposit, Dexing district, Jiangxi province, China: Economic Geology, v. 94, p. 302-324.

Helgeson, H.C., and Kirkham, D.H., 1974, Theoretical prediction of the thermodynamic behavior of aqueous electrolytes at high pressures and temperatures: II. Debye-Huckel parameters for activity coefficients and relative partial molal properties: American Journal of Science, v. 274, p. 1199-1261.

Hiatt, E.E., Kyser, T.K., Fayek, M., Polito, P., Holk, G.J., and Riciputi, L.R., 2007, Early quartz cements and evolution of paleohydraulic properties of basal sandstones in three Paleoproterozoic continental basins: Evidence from in situ δ18O analysis of quartz cements: Chemical Geology, v. 238, p. 19-37.

Hobbs, B.E., Zhang, Y., and Ord, A., 2000, Application of coupled deformation, fluid flow, thermal and chemical modeling to predictive mineral exploration: Journal of Geochemical Exploration, v. 69, p. 505-509.

Hoeve, J., and Quirt, D., 1984, Mineralization and host rock alteration in relation to clay mineral diagenesis and evolution of the middle Proterozoic, Athabasca basin, northern Saskatchewan, Canada: Saskatchewan Research Counsel Technical Report, 187p.

Hoeve, J., and Sibbald, T.I.I., 1978, On the genesis of Rabbit Lake and other unconformity-type uranium deposits in northern Saskatchewan, Canada: Economic Geology, v. 73, p. 1450-1473.

Hoeve, J., Rawsthorn, K., and Quirt, D., 1981, Uranium metallogenetic studies: clay mineral stratigraphy and diagenesis in the Athabasca Group: Saskatchewan Research Council Publication, v. 22, p. 76-89.

Jefferson, C.W., Thomas, D.J., Gandhi, S.S., Ramaekers, P., Delaney, G., Brisbin, D., Cutts, C., Quirt, D., Portella, P., and Olson, R.A., 2007, Unconformity associated uranium deposits of the Athabasca Basin, Saskatchewan and Alberta, in Goodfellow, W.D., ed., Mineral Deposits of Canada: A Synthesis of Major Deposit-Types, District Metallogeny, the Evolution of Geological Provinces, and Exploration Methods: Geological Association of Canada, Mineral Deposits Division, Special Publication, v. 5, p. 273-305.

Jennings, A.A., 1987, Critical chemical reaction rates for multicomponent groundwater contamination models: Water Resources Research, v. 23, p. 1775-1784.

Khalil, A., Hanich, I., Bannari, A., Zouhri, I., Pourret, O., and Hakkou, R., 2013, Assessment of soil contamination around an abandoned mine in a semi-arid environment using geochemistry and geostatistics: Pre-work of geochemical process modeling with numerical models: Journal of Geochemical Exploration, v. 125, p. 117-129.

Knapp, R.B., 1989, Spatial and temporal scales of local equilibrium in dynamic fluid-rock systems: Geochimica et Cosmochimica Acta, v. 53, p. 1955-64.

Kojima, S., Takeda, S., and Kogita, S., 1994, Chemical factors controlling the solubility of uraninite and their significance in the genesis of unconformity-related uranium deposits: Mineral. Deposita, v. 29, p. 353-360.

Kotzer, T.G., and Kyser, T.K., 1995, Petrogenesis of the Proterozoic Athabasca basin, northern Saskatchewan, Canada, and its relation to diagenesis, hydrothemal uranium mineralization and Paleohydrogeology: Chemical Geology, v. 120, p. 45-89.

Kotzer, T., and kyser, T. K., 1990, The use of stable and radiogennic isotopes in the identification of fluids and processes associated with unconformity-type uranium ore deposits: Geological Society of Saskatchewan Special publication, v. 10, p. 115-131.

Kuhn, M., 2004, Reactive flow modeling of hydrothermal systems: Springer-Verlag, Berlin.

Kuhn, M., Alt-Epping, P., Gessner, K., and Wilde, A., 2004, Application of reactive transport modelling to the Mount Isa Copper mineralised system: Predictive Mineral Discovery CRC conference, Barossa Valley, Australia, p. 107-110.

Kyser, T.K., Wilson, M.R., and Ruhrmann, G., 1989, Stable isotope constraints on the role of graphite in the genesis of unconformity-type uranium deposits: Canadian Journal of Science, v. 26, p. 490-498.

Lasaga, A.C., 1984, Chemical kinetics of water-rock interactions: Journal of Geophysical Research, v. 89, p. 4009-4025.

Li, Y.H., and Gregory S., 1974, Diffusion of ions in sea-water and in deep-sea sediments: Geochim Cosmochim Acta, v. 38, p. 703-714.

Lichtner, P.C., 1996, Continuum formulation of multicomponent-multiphase reactive transport. p. 1–81. In P.C. Lichtner et al. (ed.) Reactive transport in porous media: Reviews in Mineralogy, v. 34. Mineralogical Society of America, Washington, DC, p. 1-81.

Lichtner, P.C., and Biino, G.G., 1992a, A first principles approach to supergene enrichment of a porphyry copper protore: I. Cu-Fe-S subsystem: Geochimica et Cosmochimica Acta, v. 56, p. 3987-4013.

Lichtner, P.C., and Biino, G.G., 1992b, Genesis of mississippi valley- type (MVT) deposits: Geological Society of America, Abstracts with Programs, v. 24, 324p.

Lin, G., Hobbs, B.E., Ord, A., and Mühlhaus, H.B., 2003, Theoretical and numerical analyses of convective instability in porous media with temperature-dependent viscosity: Communications in Numerical Methods in Engineering, v. 19, p. 787-799.

Lin, G., Zhou, Y., and Wei, X., 2006, Structure controls on fluid flow and related mineralization in the Xiangshan uranium deposit, Southern China: Journal of Geochemical Exploration, v. 89, p. 231-234.

Lin, G., Hobbs, B.E., Zhang, L., and Zhou, Y., 2008, Potential effects of upward through flow on thermal structure models within the continental lithospheric mantle-crust: Chinese Journal of Geophysics, v. 51, p. 393-401.

Lin, G., Peng, M., Zhang, L., Zhang, D., and Liu, S., 2009, Numerical analysis and simulation experiment of lithospheric thermal structures in the South China Sea and the Western Pacific: Journal of Earth Science, v. 20, p. 85-94.

Liu, L., Yang, G., and Peng, S., 2005, Numerical modeling of coupled geodynamical processes and its role in facilitating predictive ore discovery: An example from Tongling, China: Resource Geology, v. 55, p. 21-31.

Liu, L., Shu, Z., Wan, C., Cai, A., and Zhao, Y., 2008, The controlling mechanism of ore formation due to flow-focusing dilation spaces in skarn ore deposits and its

significance for deep-ore exploration: Examples from the Tongling-Anqing district: Acta Petrologica Sinica, v. 24, p. 1848-1856.

Liu, L., and Zhao, Y., 2010, Coupled geodynamics in the formation of Cu skarn deposits in the Tongling-Anqing district, China: computational modeling and implications for exploration: Journal of Geochemical Exploration, v. 106, p. 146-155.

Liu, L., Wan, C., and Zhao, Y., 2011, Geodynamic constraints on orebody localization in the Anqing orefield, China: Computational modeling and facilitating predictive exploration of deep deposits: Ore Geology Reviews, v. 43, p. 249-263.

Mugler, C., Rabouille, C., Bombled, B., and Montarnal, P., 2012, Impact of spatial heterogeneities on oxygen consumption in sediments: Experimental observations and 2D numerical modeling: Journal of Geochemical Exploration, v. 112, p. 76-83.

Narasimhan, T.N., and Witherspoon, P.A., 1976, An integrated finite difference method for analyzing fluid flow in porous media: Water Resource Research, v. 12, p. 57-64.

Nordstrom, D.K., and Muñoz, J.L. (Eds.), 1986, Geochemical Thermodynamics: The Benjamin/Cummings Pub. Co, Menlo Park, California.

Ord, A., Hobbs, B.E., Zhang, Y., Broadbent, G.C., Brown, M., Willetts, G., and Sorjonen-Ward, P., 2002, Geodynamic modeling of the Century deposit, Mt Isa Province, Queensland: Australian Journal of Earth Sciences, v. 49, p. 1011-1039.

Parkhurst, D.L., Thorstenson, D.C., and Plummer, L.N., 1980, PHREEQE: A computer program for geochemical calculations: US Geological Survey, Water Resource Investigation, p. 80-96, 174 p.

Peiffert, C., Cuney, M., and Nguyen-Trung, C., 1994, Uranium in granitic magmas: Part 1. Experimental determination of uranium solubility and fluid-melt partition

coefficients in the uranium oxide-haplogranite- H2O-Na2CO3 system at 720-770°C, 2 kbar: Geochimica et Cosmochimica Acta, v. 58, p. 2495-2507.

Peiffert, C., Nguyen-Trung, C., and Cuney, M., 1996, Uranium in granitic magmas: Part 2. Experimental determination of uranium solubility and fluid-melt partition coefficients in the uranium oxide-haplogranite-H2O-NaX (X =Cl, F) system at 770°C, 2 kbar: Geochimica et Cosmochimica Acta, v. 60, p.1515-1529.

Pitzer, K.S., 1973, Thermodynamics of electrolytes. 1. Theoretical basis and general equations: Journal of Physical Chemistry, v. 77, p. 268-277.

Pitzer, K.S., 1975, Thermodynamics of electrolytes. V. Effect of high order electrostatic terms: Journal of Solution Chemistry, v. 4, p. 249-265.

Pruess, K., 1987, TOUGH user's guide, Nuclear Regulatory Commission: Report NUREG/CR-4645 (also Lawrence Berkeley Laboratory Report LBL-20700, Berkeley, California).

Pruess, K., 1991, TOUGH2: A general numerical simulator for multiphase fluid and heat flow: Lawrence Berkeley Laboratory Report LBL-29400, Berkeley, California.

Pruess, K., Oldenburg, C., and Moridis, G., 1999, TOUGH2 user's guide, Version 2.0: Lawrence Berkeley Laboratory Report LBL-43134, Berkeley, California.

Pruess, K., Oldenburg C., and Moridis G., 2012, TOUGH2 User's Guide, Version 2.1: Report LBNL-43134, Lawrence Berkeley National Laboratory, Berkeley.

Raffensperger, J.P., 1993, Quantitative evaluation of the hydrologic and geochemical processes in the formation of unconformity-type uranium deposits: Unpublished Ph.D. thesis, Baltimore, John Hopkins University, 679 p.

Raffensperger, J.P., Garven, G., 1995a, The formation of unconformity- type uranium ore deposits 1. Coupled ground water flow and heat transport modeling: American Journal of Science, v. 295, p. 581-636.

Raffensperger, J.P., and Garven, G., 1995b, The formation of unconformity- type uranium ore deposits 2. Coupled hydrochemical modeling, American Journal of Science, v. 295, p. 639-696.

Ramaekers, P., 1990, Geology of the Athabasca Group (Helikian) in northern Saskatchewan: Saskatchewan Energy and Mines, Saskatchewan Geological Survey, Report 195, 49 p.

Reed, M.H., 1982, Calculation of multicomponent chemical equilibria and reaction processes in systems involving minerals, gases and aqueous phase: Geochimica et Cosmochimica Acta, v. 46, p. 513-528.

Renac, C., Kyser, T. K., Durocher, K., Dreaver, G., and O'Connor, T., 2002, Comparison of diagenetic fluids in the Proterozoic Thelon and Athabasca Basins, Canada: Implications for protracted fluid histories in stable intracratonic basins: Canadian Journal of Earth Sciences, v. 39, p. 113-132.

Richard, A., Rozsypal, C., Mercadier, J., Cuney, M., Boiron M-C, Cathelineau, M., and Banks, D. A., 2012, Giant uranium deposits formed from exceptionally uranium-rich acidic brines. Nature Geoscience, v. 5, p. 142-146.

Rozos, E., D. and Koutsoyiannis, 2005, Application of the Integrated Finite Difference Method in groundwater flow: Geophysical Research Abstracts, European Geosciences Union, Vienna, 00579, p. 7.

Schmidt Mumm, A., Brugger, J., and Schacht, U., 2010, Fluids in geological processes: The present state and future outlook: Journal of Geochemical Exploration, v. 106, p. 1-7.

Simunek, J. and Valocchi, A.J., 2002, Geochemical Transport, Chapter 6.9 in Methods of Soil Analysis, Part I, Physical Methods , C. Topp and J. Dane, eds: Soil Science Society of America, Madison, WI.

Soler, J.M., and Lasaga, A.C., 1998, An Advection-Dispersion-Reaction Model of Bauxite Formation: Journal of Hydrology, v. 209, p. 311-330.

Sorjonen-Ward, P., and Zhang, Y., 2002, Numerical modelling of orogenic processes and mineralization in the south eastern part of the Yilgarn Craton, Western Australia: Australian Journal of Earth Sciences, v. 49, p. 935-964.

Steefel, C.I., and Lasaga, A.C., 1994, A coupled model for transport of multiple chemical species and kinetic precipitation/dissolution reactions with applications to reactive flow in single phase hydrothermal system: American Journal of Science, v. 294, p. 529-592.

Steefel, C.I., and Lasaga, A.C., 1990, Evolution of dissolution patterns-permeability change due to coupled flow and reaction: In Melchior DC, Bassett RL (eds) ACS symposium series, chemical modeling of aqueous systems II, No. 416, Chap. 2, Amertican Chemical Society, Washington DC, p. 213-225.

Sung, K.Y., Yun, S.T., Park, M.E., Koh, Y.K., Choi, B.Y., Hutcheon, I., and Kim, K.H., 2012, Reaction path modeling of hydrogeochemical evolution of groundwater in granitic bedrocks, South Korea: Journal of Geochemical Exploration, v. 118, p. 90-97.

Tremblay, L.P., 1982, Geology of the uranium deposits related to sub-Athabasca unconformity, Saskatchewan. Geological Society of Canada, Paper 81-20.

Valocchi, A.J., 1985, Validity of the local equilibrium assumption for modeling sorbing solute transport through homogeneous soils: Water Resources Research, v. 21, p. 808-820.

Valocchi, A.J., 1988, Theoretical analysis of deviations from local equilibrium during sorbing solute transport through idealized stratified aquifers: Journal of Contaminant Hydrology, v. 2, p. 191-207.

Wilde, A.R., and Wall, V.J., 1987, Geology of the Nabarlek uranium deposit, Northern Territory, Australia: Economic Geology, v. 82, p. 1152-1168.

Wilde, A.R., Mernagh, T.P., Bloom, M.S., and Hoffman, C.F., 1989, Fluid inclusion evidence on the origin of some Australian unconformity-related uranium deposits: Economic Geology, v. 84, p. 1627-1642.

Wilde, A.R., Bloom, M.S., and Wall, V.J., 1989, Transport and deposition of gold, uranium, platinum-group elements in unconformity- related uranium deposits: Econ. Geol., Monogr., v. 6, p. 637-650.

Wilde, A.R., Wall, V.G., and Bloom, M.S., 1985, Wall-rock alteration associated with unconformity-related uranium deposits Northern Territorry, Australia: implications for uranium transport and depositional mechanisms: Int. Meet. 'Concentration Mechanisms of Uranium in Geological Environments', Nancy, France, pp 231-239.

Wolery, T.J., 1992, EQ3/6: Software package for geochemical modeling of aqueous systems: Package overview and installation guide (version 7.0): Lawrence

Livermore National Laboratory Report UCRL-MA-110662 PT I, Livermore, California.

World Nuclear Association: http://www.world-nuclear.org.

Xing, H.L., and Makinouchi, A., 2008, Three-dimensional finite element simulation of large-scale nonlinear contact friction problems in deformable rocks: Journal of Geophysics and Engineering, v. 5, p. 27-36.

Xu, T., and Pruess, K., 1998, Coupled modeling of non-isothermal multiphase flow, solute transport and reactive chemistry in porous and fractured media: 1. Model development and validation: Lawrence Berkeley National Laboratory Report LBNL-42050, Berkeley, California.

Xu, T., and Pruess, K., 2001, On fluid flow and mineral alteration in fractured caprock of magmatic hydrothermal systems: Journal of Geophysical Research, v. 106, p. 2121-2138.

Xu, T., Ontoy, Y., Molling, P., Spycher, N., Parini, M., and Pruess, K., 2004a. Reactive transport modeling of injection well scaling and acidizing at Tiwi Field Philippines: Geothermics, v. 33, p. 477-491.

Xu, T., Sonnenthal, E., Spycher, N., and Pruess, K., 2004b, TOUGHREACT user's guide: A simulation program for nonisothermal multiphase reactive geochemical transport in variably saturated geologic media: Earth Sciences Division, Lawrence Berkeley National Laboratory Report CA 94720, Berkeley, California.

Xu, T., Sonnenthal, E., Spycher, N., Pruess, K., Brimhall, G., and Apps, J., 2001, Modeling multiphase fluid flow and reactive geochemical transport in variably

saturated fractured rocks: 2. Applications to supergene copper enrichment and hydrothermal flows: American Journal of Science, v. 301, p. 34-59.

Yan, Y., Lin, G., Wang, Y.J., Guo, F., and Li, Z.A., 2003, Apatite fission track age of Mesozoic sandstones from Beipiao basin, eastern China: Implications for basin provenance and tectonic evolution: Geochemical Journal, v. 37, p. 377-389.

Yeh, G.T., and Tripathi, V.S., 1991, A model for simulating transport of reactive multispecies components: model development and demonstration: Water Resource Research, v. 27, p. 3075–3094.

Yeo, G.M., and Potter E.G., 2010, Review of reducing mechanisms potentially involved in the formation of unconformity-type uranium deposits and their relevance to exploration, in summary of investigations: Saskatchewan Geological Survey, Ministry of Energy and Resources 2, Paper A-12.

Zhang, L., Li, Z., Lin, G., and Guo, H., 2011, Numerical simulation of effects of upward throughflow on thermal structure and the thickness of the continental lithosphere: Journal of Geophysics and Engineering, v. 8, p. 322-329.

Zhang, Y., Hobbs, B.E., Ord, A. Barnicoat, A., and Lin, G., 2003, The influence of faulting on host-rock permeability, fluid flow and ore genesis of gold deposits: a theoretical 2D numerical model: Journal of Geochemical Exploration, v. 78, p. 279-284.

Zhang, Y., Schaubs, P.M., Ord, A., Hobbs, B.E., and Barnicoat, A., 2008, Fault-related dilation, permeability enhancement, fluid flow and mineral precipitation patterns: numerical models, in: Wibberley, C.A.J., Kurz, W., Imber, J., Holdsworth, R.E., Collettini, C. (Eds.), The Internal Structure of Fault Zones: Implications for

Mechanical and Fluid-flow Properties: Geological Society 299, Special Publications, London, p. 239-255.

Zhao, C., 2009, Dynamic and Transient Infinite Elements: Theory and Geophysical, Geotechnical and Geoenvironmental Applications. Springer, Berlin.

Zhao, C., Hobbs, B.E., and Ord, A., 2008a. Convective and Advective Heat Transfer in Geological Systems. Springer, Berlin.

Zhao, C., Hobbs, B.E., Hornby, P., Ord, A., Peng, S., and Liu, L., 2008b, Theoretical and numerical analyses of chemical-dissolution front instability in fluid-saturated porous rocks: International Journal for Numerical and Analytical Methods in Geomechanics v. 32, p. 1107-1130.

Zhao, C., Hobbs, B.E., and Ord, A., 2009, Fundamentals of Computational Geoscience: Numerical Methods and Algorithms, Springer, Berlin.

Zhao, C., Hobbs, B.E., and Ord, A., 2010, Theoretical analyses of nonaqueous-phase-liquid dissolution induced instability in two-dimensional fluid-saturated porous media: International Journal for Numerical and Analytical Methods in Geomechanics, v. 34, p. 1767-1796.

Chapter 3[1]

Evaluation of Fe-rich chlorite as a reducing agent in the formation of unconformity-related uranium deposits: insights from reactive flow modeling

3.1 Introduction

World-class unconformity-related uranium (URU) deposits, hosted by the Athabasca Basin in Canada and the Kombolgie Basin in Australia, formed as a result of long-lived diagenetic and hydrothermal fluid systems (Gustafson and Curtis, 1983; Wilde et al., 1989b; Kotzer and Kyser, 1995; Renac et al., 2002). Based on the proposed diagenetic-hydrothermal model for the URU deposits (Hoeve et al., 1981; Hoeve and Quirt, 1984), uranium minerals precipitate when oxidized uranium-bearing brines mix with basement-derived reducing fluids or react with reducing minerals in the basement. It is believed that the interaction of oxidized uranium-bearing fluids with reductants provides favorable geochemical conditions for precipitation of uraninite. Regarding the reducing mechanisms leading to the precipitation of URU deposits, two major reductants have been proposed, including carbon-based and inorganic-based reducing mechanisms (Yeo and Potter, 2010). The carbon-based reductants include detrital organic matter (Yeo et al.,

[1] This chapter has been submitted (under review) to Mineralium Deposita in a slightly modified form, "Aghbelagh, Y., and Yang, J., 2015. Evaluation of Fe-rich chlorite as a reducing agent in the formation of unconformity-related uranium deposits: Insights from reactive flow modeling.

2007), fluid hydrocarbons (McCready et al., 1999; Annesley et al., 2001; Alexandre and Kyser, 2006), methane or CO_2 associated with graphitic pelite (Price, 1997), methane or CO_2 derived from graphitic pelite (Hoeve and Sibbald, 1978; Kyser et al., 1989; Raffensperger and Garven, 1995b), and direct reduction of U^{6+} by graphite (Alexandre et al., 2005). Among these reductants, methane derived from graphite in pelites is popular since most of the known URU deposits in the Athabasca Basin are associated with graphitic basement units, and these units are considered a key exploration parameter for uranium deposits (Jefferson et al., 2007). According to this model, graphitic units in the basement and pre-ore alteration served as both physical (fractured zones) and chemical (reductant) traps for the uranium mineralization (Alexandre et al., 2005). Aghbelagh and Yang (2014) considered methane derived from graphitic pelite as a reducing agent in the formation of URU deposits. Using reactive mass transport modeling, the formation of URU deposits is predicted in the basement close to the unconformity and away (about 2.5 km) from the faulted graphite-rich zone over a time scale of 0.1 to 1 Ma (Aghbelagh and Yang, 2014).

A fluid inclusion study by Derome et al. (2003) indicates that low-salinity CH_4-bearing fluids were derived from the basement in the Kombolgie Basin, but are rarely recorded by fluid inclusions in the Athabasca Basin. In addition, some URU deposits were formed in the absence of graphitic units (Fuchs and Hilger, 1989; Jefferson et al., 2007; Alexandre et al., 2012), suggesting that inorganic reductants may play a role in their precipitation. For example, there is a paucity of graphite in basement lithologies at the Centennial uranium deposit which is located in the south-central Athabasca Basin (Alexandre et al., 2012). Additionally, the mineralization is away from the Dufferin Lake

fault representing a main fluid conduit in the area (Alexandre et al., 2012). The uranium grade of this deposit is lower than that of typical URU deposits such as McArthur River and Cigar Lake in the Athabasca Basin, but is above the world average uranium grade of 0.2 %. Inorganic-based reducing agents proposed for precipitation of URU deposits include hydrogen sulfide (H_2S) from pyrite (Cheney 1985; Ruzicka, 1993), ferrous iron (Fe^{2+}) from Fe-sulfides (Bray et al., 1982), and ferrous iron from alteration of silicates (Komninou and Sverjensky, 1996; Alexandre et al., 2005; Acevedo and Kyser, 2015).

The considered silicate minerals include either metamorphic phases such as Fe-rich garnet, biotite, and hornblende, or Fe-rich chlorite that precipitated during the pre-ore alteration stage. Destruction of Fe-rich chlorite produces Fe^{2+} (aq), and this cation reduces the oxidized aqueous uranium, consequently leading to precipitation of uraninite (Komninou and Sverjensky, 1996). In this paper, Fe-rich chlorite is considered for the precipitation of uraninite through the following reactions:

Destruction of Fe-rich chlorite (Komninou and Sverjensky, 1996; Alexandre et al., 2005; Acevedo and Kyser, 2015) at temperatures of typical URU ore forming brines (120-200 °C) releases Fe^{2+}:

$$(Mg_{2.5}Fe_{2.5})Al_2Si_3O_{10}(OH)_8 + 8H^+ \leftrightarrow 3SiO_2(aq) + \frac{5}{2}Fe^{2+} + \frac{5}{2}Mg^{2+} + 8H_2O + 2AlO_2^-. \quad (3.1)$$

And Fe^{2+} causes the uranium precipitation:

$$UO_2^{2+} + 2Fe^{2+} + 3H_2O \leftrightarrow UO_2 + Fe_2O_3 + 6H^+. \quad (3.2)$$

According to reaction (3.2), Fe^{2+} reduces the aqueous uranium to precipitate uraninite, and then becomes oxidized to precipitate as hematite. Through this mechanism, the uranium carried by the oxidized fluids (e.g., Kotzer and Kyser, 1995) encounters Fe-rich

chlorite alteration zones either in the basement or in the sandstone (Alexandre et al., 2005), leading to the simultaneous precipitation of uraninite and hematite. To date, inorganic reducing agents, including ferrous iron, have not been computationally simulated yet as potential agents in the formation of uraninite.

Differing diagenetic models have proposed two possible uranium sources (Cuney, 2003; Cuney and Kyser, 2009). One considers the overlying basinal sediments as a source of uranium (e.g., Wilson and Kyser, 1987; Kotzer and Kyser, 1995; Raffensperger and Garven, 1995a, b; Fayek and Kyser, 1997), and the other considers the basement as the uranium source (e.g., Annesley and Madore, 1999; Hecht and Cuney, 2000; Mercadier et al., 2010; Richard et al., 2012). The question of where the large amount of uranium is sourced still remains unresolved. Mineralization of URU deposits has been simulated by considering the basinal sandstone as a source of uranium and methane as a reducing agent (Raffensperger and Garven, 1995b; Aghbelagh and Yang, 2014). However, the basement has not been considered yet as a potential source of uranium in computational studies related to mineralization of URU deposits. In the present study, Fe-rich chlorite is simulated as a reducing agent (rather than methane) and both the sandstone and the basement are evaluated, respectively, as the sources of uranium.

Large scale circulation of the fluids within the basinal sandstone is responsible for the transport and deposition of uranium (Hoeve and Sibbald, 1978, Hoeve et al., 1980, Fayek and Kyser, 1997). In addition to fluid flow, heat and reactive mass transport in the porous media are contributing processes for deposition of uranium. Previous studies either focus on fluid flow modeling (e.g., Alexandre and Kyser, 2012; Cui et al., 2010, 2012a, b; Chi et al., 2013, 2014; Li et al., 2014, 2015) or on geochemical modeling (e.g.,

Komninou and Sverjensky, 1996), and few studies have been done on combined fluid flow and chemical reaction modeling (e.g., Raffensperger and Garven, 1995b; Aghbelagh and Yang, 2014). Raffensperger and Garven (1995b) predicted the formation of uranium ore deposits within the sandstone cover in the Athabasca Basin over a time scale of 0.1 to 1 Ma. In their conceptual model, the faults were only limited to the basement. However, it is now clear that they are rooted in the basement and can extend into the basin (McGill, 1999). Also, they conjectured methane which is derived from hydrothermal alteration of graphite as a reducing agent for precipitation of uraninite, and did not examine any other reducing mechanisms. In addition, for the dissolution and precipitation of minerals, their model only considers the simple case of equilibrium conditions. In reality, as is confirmed by laboratory experiments (Baermann et al., 2000), except for a few minerals (e.g., anhydrite and calcite) that have a rapid reaction rate, equilibrium is not always achieved (Xu et al., 2004). In the present study, ferrous iron is considered as a reducing agent rather than methane. In addition, the fault zones are not limited to the basement, and extended into the sandstone unit. Also, except for anhydrite and calcite, the kinetic approach is adopted for the dissolution and precipitation of all minerals.

3.2 Two-dimensional conceptualized models

In order to develop a conceptual model that adequately describes a typical URU deposit in a sedimentary basin at the time of ore deposition, a thorough knowledge of the basin at the deposit scale including its geology, tectonic history, and stratigraphy is required. The Athabasca Basin is one of the most studied basins with URU mineralization (Hoeve et al., 1980; Ramaekers, 1990; Kotzer and Kyser, 1995; Hecht and Cuney, 2000; Renac et al.,

2002; Alexandre et al., 2005; Mercadier et al., 2010; Richard et al., 2010; Acevedo and Kyser, 2015), making it ideal for developing conceptual models. The Athabasca Basin occurs as a series of northeast-southwest oriented sub-basins controlled by major Hudsonian faults rooted in the basement rocks (Hoeve and Sibbald, 1978; Hoeve and Quirt, 1984; Ramaekers, 1990; Kotzer and Kyser, 1995). These faults were reactivated after the Athabasca Basin was formed (Hoeve and Sibbald, 1978; Kotzer and Kyser, 1995) and have remained active until recent times (Hoeve and Quirt, 1984). Although major URU deposits are located in the eastern part of the basin, deposition of the uranium is not limited to the east and some URU deposits have been discovered in the west part of the basin such as in the Shea Creek area. The McArthur River deposit is a type example in the eastern part of the Athabasca Basin. The deposit is structurally controlled by the northeast-trending, southeast dipping, graphite-rich reverse faults which are rooted in the basement and extend several meters over the unconformity surface into the basinal sandstone (McGill, 1999). In the Shea Creek area, three main Paleoproterozoic basement lithostratigraphic units have been identified: a metasedimentary unit (consisting of metapelites and garnetites) in which graphite is mainly concentrated along reverse faults, surrounded by two metaigneous felsic gneiss units, one above and another below the metasedimentary package (De Veslud et al., 2009). By considering these points, and based on previous studies (Raffensperger and Garven, 1995b; Cui et al, 2012a; Aghbelagh and Yang, 2014), a simplified paleo-hydrostratigraphic model is developed for a typical URU deposit. This sandwich-like conceptual model (Fig. 3.1) consists of four hydrostratigraphic units: basement rock, dipping fault zone, overlying sandstone, and upper confining unit; discretized into 80×80 quadrilateral Integral Finite Difference

(IFD) elements. The fault zone is assumed to straddle the unconformity in the central part of the model, with a dimension of 300 m by 1200 m. The hydrostratigraphic units are modeled as homogeneous units, and the physical properties assumed for each unit (Table 2.1) are based on the data used in similar numerical modeling and published compilations (e.g., Freeze and Cherry, 1979; Garven and Freeze, 1984; Raffensperger and Garven, 1995a, b; Mclellan et al., 2004; Yang et al., 2004; Oliver et al., 2006; Cui et al., 2012a; Aghbelagh and Yang, 2014).

Aghbelagh and Yang (2014) simulated the formation of URU deposits in the presence of graphite distributed along the fault zone. Methane is produced by the alteration of the graphite zone (Hoeve and Sibbald, 1978; Kyser et al., 1989; Raffensperger and Garven, 1995b) at temperatures of typical URU ore forming brines (120-200 °C) through the following reaction:

$$C + \frac{3}{2}H_2O \leftrightarrow \frac{1}{2}H^+ + \frac{1}{2}HCO_3^- + \frac{1}{2}CH_4^0(aq). \quad (3.3)$$

Which then acts as a reducing agent for the reduction of uraninite through the following reaction:

$$UO_2^{2+} + \frac{3}{4}H_2O + \frac{1}{4}CH_4^0(aq) \leftrightarrow UO_2 + \frac{1}{4}HCO_3^- + \frac{9}{4}H^+. \quad (3.4)$$

The focus of the present study is to investigate URU deposits that formed in the absence of graphite. Therefore, the fault zone now does not include graphite, and its mineralogical properties are assumed to be same as that of the basement.

The bottom and sides are modeled as impermeable boundaries, and the top surface is assumed to be permeable by assigning a fixed pore pressure of 30 Mpa based on previous studies (e.g., Cui et al., 2012a; Chi et al., 2013; Aghbelagh and Yang, 2014; Li

et al., 2015). The side boundaries are considered to be insulated to heat transport and a constant fixed temperature of 90 °C and 240 °C (corresponding to a geothermal gradient of 30 °C/km) is assumed for the top and bottom of the model, respectively. For the concentration of aqueous components and mineral volume fractions at the top and bottom boundaries, a first-type boundary condition is assigned. That is, the concentration of aqueous components and mineral volume fractions are assumed to be constant, which are the same as those of their respective units (Tables 2.2, 2.3, 2.8, and 2.9). For the side boundaries the second-type boundary condition is employed, where the normal gradients of the concentration of aqueous components and mineral volume fractions are assumed to be zero. For the initial conditions, a hydrostatic pressure gradient of 10 MPa/km (e.g., Cui et al., 2012a; Chi et al., 2013; Aghbelagh and Yang, 2014) and a thermal gradient of 30 °C/km are applied.

Initial chemical compositions for each hydrostratigraphic unit are tabulated in Tables 2.2, 2.3, 2.6, 2.7, 2.8, and 2.9. These tables are based on previous mineralogical studies (e.g., Alexandre et al., 2005) and hydrochemical modeling of URU deposits (Raffensperger and Garven, 1995b; Aghbelagh and Yang, 2014). The basement unit is mainly composed of quartz, muscovite, and K-feldspar with accessory anhydrite, chlorite, hematite, pyrite, and kaolinite (Hoeve and Quirt, 1984; Fayek and Kyser, 1997; Adlakha et al., 2014). Based on a previous study by Raffensperger and Garven (1995b), the basal brines are assumed to be under moderately reducing (Log $fO2$ =-46.834) and acidic (pH=4.541) conditions. The fault zone is assumed to contain the same mineralogical properties as the basement, but with different physical properties (e.g., higher porosity and permeability). The sandstone unit is predominantly composed of quartz and hematite

with accessory muscovite, anhydrite, chlorite, K-feldspar, and kaolinite (Tremblay, 1982; Fayek and Kyser, 1997; Hiatt et al., 2007; Alexandre et al., 2009; Adlakha et al., 2014). For the basinal brines, oxidizing (Log *f*O2 =-22.825) and acidic (pH=5.131) conditions are assigned. The reason for choosing such an oxygen fugacity value is that the fluids responsible for the formation of URU deposits must have had high oxygen fugacities to transport appreciable amounts of uranium (Komninou and Sverjensky, 1996; Raffensperger and Garven, 1995b). Thermodynamic calculations have shown that log fO_2 must have been above -24 at 200 °C to account for dissolved U(VI) (as uranyl complexes), well above the hematite-magnetite buffer (log fO_2=-39.5 at 200 °C) (Komninou and Sverjensky, 1996). Overlying the sandstone unit (confining unit) is a sequence of less permeable marine sandstones, siltstone, and mudstone (Ramaekers, 1990; Kotzer and Kyser, 1995). This unit corresponds to the Wolverine Point formation in the Athabasca Basin. It is mainly composed of calcite, quartz, and kaolinite along with other minerals such as dolomite, muscovite, anhydrite, and hematite (Raffensperger and Garven, 1995b; Aghbelagh and Yang, 2014). In comparison with the sandstone unit, this unit is in a more oxidizing condition (Log *f*O2 =-14.763), with a similar acidic (pH=5.290) condition. The initial volume fraction of Fe-rich chlorite in the basement is assumed to be 0.056 mol/L, higher than that in the sandstone (0.003 mol/L). This is because the basement rocks hosting most URU deposits have been affected by pervasive chloritization (Reid et al., 2010). Similarly, the initial concentration of Fe^{2+} in the basement (0.002 mol/L) is also assumed higher than that in the sandstone and confining units (2.6×10^{-11} mol/L and 7.3×10^{-15} mol/L, respectively).

As for addressing the sources of uranium, two separate models are developed. In the first model, the sandstone is conjectured to be a uranium source by assigning an initial fluid composition of 1×10^{-4} mol/L ($\simeq$ 27 ppm) total uranium therein, according to Raffensperger and Garven (1995b). Richard et al. (2012) analyzed the uranium concentration in the fluid inclusions, selected in the quartz veins contemporaneous with major alteration events and uranium ore deposition, from several basement-hosted deposits such as Rabbit Lake, Eagle Point, P-Patch and Millennium. They found that a uranium concentration of 1×10^{-4} mol/L in ore-forming brines represents an average value found in fluid inclusions. This concentration is reasonable to form such deposits in a time period of 0.1-1 million years (Raffensperger and Garven, 1995b; Richard et al., 2012). In the second model, the basement is considered to be a source of aqueous uranium by assigning the same initial uranium concentration. Both models are compared in terms of their capability in the mineralization of a typical URU deposit.

3.3 Modeling approach

Numerical simulations are performed with the TOUGHREACT code (Xu and Pruess, 2001; Xu et al., 2004a; Xu et al., 2006) which couples fluid flow, heat and reactive mass transport processes (refer to Section 2.3). An extended version of the modeling approach which includes the code's capabilities in simulating these processes, as well as governing equations, and space discretization method is presented in detail in Appendix 1.

The geochemical subsystem (Appendix 4) reflects the reactions considered for secondary aqueous species and minerals, which include aqueous complexation, acid-base, redox, cation exchange, and mineral dissolution/precipitation reactions. The associated

thermodynamic database for this geochemical subsystem consists of 13 primary species, 56 secondary species and 20 minerals (Appendix 4). It should be noted that in this geochemical subsystem, Fe^{2+} is used for formulating the redox reaction of uraninite, and $H^+$is used as a primary species for the variation in fluid pH associated with every layer.

3.4 Results

3.4.1 Sandstone as a source of uranium

Figure 3.2A shows the fluid flow pattern and flow rate (Darcy velocity) around the fault zone at 100,000 years. Due to the larger permeability of the fault zone (Table 2.1) compared with that of the other hydrostratigraphic units, the maximum fluid flow rate of 7×10^{-8} m/s (about 2.2 m/year) occurs along this zone. The uranium-bearing basinal brines flow into the fault zone and interact with the basement lithology. Also, the basal fluids use this zone as a conduit to flow into the sandstone unit and mix with the basinal brines. This process is continuous and provides a mechanism for interaction of the sandstone with the basement. Figures 3.2B-E show the fluid flow pattern and temperature distribution throughout the model area at different times. Fluid flow rate (Darcy velocity) within the sandstone unit reaches the maximum value of 3.5×10^{-8} m/s (about 1.1 m/year, which is in agreement with previous studies (e.g., Raffensperger and Garven, 1995a, b) on the URU deposits in the sedimentary basins. Fluid convection develops in the sandstone unit, and is responsible for leaching uranium from the source rocks. The downwelling parts of the convection cells allow the basinal brines to penetrate into the basement, while the upwelling parts of the convection cells enable the basal fluids to be

brought into the sandstone, as confirmed previously by Cui et al. (2012b). At 10,000 years (Fig. 3.2B), four convection cells develop in the sandstone unit. One major convection cell is located on the right side of the sandstone, while 3 minor ones are located on the left side of the sandstone unit. The dip direction of the fault controls the positions of the convection cells within the sandstone unit, allowing the development of the major convection cell therein. At 340,000 years (Fig. 3.2D), the system approaches a steady-state condition in which the observed pattern of fluid flow remains unchanged. Figures 3.2E depicts the fluid flow regime at 500,000 years, showing that the magnitude and direction of flow are similar to those at 340,000 years. As shown in Figs. 3.2B-3.2E, the temperature is significantly affected by the fluid flow pattern in the system. Convective fluid flow within the basinal sandstone results in a temperature range of 120-150 °C therein. The asymmetric temperature distribution is obviously due to the dipping direction of the fault.

Prior to 100,000 years, no uraninite precipitates in the model area (Fig. 3.2F). Uraninite starts to precipitate at about 100,000 years (Fig. 3.2G) in the basement, 750 meters away from the fault and unconformity interface intersection and 1130 meters below the unconformity. At this time, the convection cells (Fig. 3.2C) are well-established throughout the sandstone. Establishment of the convection cells is required for precipitation of uraninite since it allows sufficient uranium to be leached from the source rock and transported in the form of uranyl-complexes in the basin. The maximum volume fraction of the precipitated uraninite (0.009) is equivalent to uraninite grade of 0.39 % which is higher than the grade of some URU deposits in Canada and Australia (e.g., Collins Bay deposit with a grade of 0.25 %; Fond-du-Lac prospect with a grade of

0.2 %; Jabiluka 1 deposit with a grade of 0.212 %; Ranger 1 and 3 deposits with the grades of 0.271 % and 0.22 %, respectively), and comparable with that of the Rabbit Lake uranium deposit with an average grade of 0.4 % (Tremblay, 1982; Fryer and Taylor, 1984; Thomas et al., 2000; McKay and Miezitis, 2001; Andrade, 2002; Gandhi, 2007; Jefferson et al., 2007; Cameco Annual Report, 2014; AMEC Americas Limited, 2014) in the Athabasca Basin. Precipitation of uraninite away from the fault zone and in the basement is likely due to the dominant downwelling flow and the resultant temperature distribution on the right-hand side of the solution domain (refer to Figs. 3.2C and 3.2G). Figures 3.2H and 3.2I depict the precipitated uraninite at 340000 and 500000 years, respectively, showing no significant change in size, which implies that the precipitation of uraninite stopped sometime after 100,000 years. According to the reaction (3.2), concentration of UO_2^{2+} and Fe^{2+} plays a critical role in the precipitation of uraninite, with UO_2^{2+} as the source and Fe^{2+} as the reducing agent. Figures 3.3A-D show the concentration of UO_2^{2+} throughout the model at 10,000, 100,000, 340,000, and 500,000 years, respectively. The black triangles show the location of the precipitated uraninite projected from Figs. 3.2G-I. It should be pointed out that the system is closed, and no new uranium is provided to the system either from the sides or from below. The uranium source is set up as an initial condition of UO_2^{2+} (refer to the last paragraph of Section 3.2). It can be seen from Figs. 3.3B-C that the concentration of UO_2^{2+} experiences a big drop from 100,000 to 340,000 years throughout the model. This is due to the fact that the initial uranium concentration has been consumed to form the secondary uranium species (e.g., U^{3+}, U^{4+}, UCl^{3+}, UCl_2^{2+}, $UHCO_3^{3+}$, $U(HCO_3)_2^{2+}$, UO_2^{+}, $UO_2Cl(aq)$, $UO_2Cl_2^{-}$, $UO_2HCO_3(aq)$, $UO_2(HCO_3)_2^{-}$, $UO_2(CO_3)_2^{-2}$, UO_2Cl^{+}, $UO_2Cl_2(aq)$,

$UO_2CO_3(aq)$, $UO_2HCO_3^+$, $UO_2(HCO_3)_2(aq)$, $UO_2HSO_4^+$, and $UO_2SO_4(aq)$) and also precipitate uraninite. Interaction of UO_2^{2+} with other aqueous species (Appendix 4), which leads to the formation of secondary uranium species and uranium deposit, reduces the initially assigned UO_2^{2+} to a background concentration of 1.19×10^{-14} mol/L ($\simeq$ 5.157×10^{-9} ppm) (Figs. 3.3C and 3.3D). Figures 3.3E-H show the concentration of Fe^{2+} throughout the model at 10,000, 100,000, 340,000, and 500,000 years, respectively. Similarly, the concentration of Fe^{2+} exhibits an initial quick drop from 100,000 to 340,000 years, and then remains almost the same. The concentration of UO_2^{2+} and Fe^{2+} may explain why the volume fraction of uraninite does not change after 100,000 years. The time required to form a uranium deposit is consistent with previous studies (0.1-1 million years) on URU deposits (Raffensperger and Garven, 1995b; Richard et al., 2012).

In addition to the concentrations of UO_2^{2+} and Fe^{2+}, physicochemical parameters such as temperature, pH, and oxygen fugacity also collectively control whether the metals are deposited to form ore, or remain in the fluids to be transported (Peiffert et al. 1994, 1996). As proposed by Cuney (2009) and confirmed by Aghbelagh and Yang (2014), geochemical precipitation of uranium in most deposits is related to a decrease of oxygen fugacity, generally resulting from the interaction of oxidized uranium-bearing fluids with reductants. In the present study, according to reaction (3.2), Fe^{2+} causes the oxidized uranium to be reduced. Primary mineralization of URU deposits occurs when the fluid temperature drops to ~ 180 °C (Kotzer and Kyser, 1995; Renac et al., 2002; Derome et al., 2005; De Veslud et al., 2009; Richard et al., 2012). Figs. 3.2B-I show that uraninite forms in the areas with temperature of about 180 °C, which is in good agreement with the previous findings. In addition, pH is a key factor contributing to the

precipitation of uraninite (Richard et al., 2012). Different ranges of pH have been proposed for the URU ore forming brines. Wilde et al. (1985, 1989a) suggested a pH of 4.5 at 200 °C for Alligator Rivers' uranium ore forming fluids. Kotzer and Kyser (1995), based on the study in the Shea Creek area in the Athabasca Basin, proposed that syn-ore fluids were in a slightly more alkaline condition. A pH range of 4.8-6 was calculated by Komninou and Sverjensky (1996) for the fluids in equilibrium with the basement schists in the Kongarra uranium deposit. Kojima et al. (1994) suggested that the Athabasca Basin ore forming fluids were in the nearly neutral range of pH (5-7). More recently, Richard et al. (2012) proposed a pH range of 2.5-4.5 for uranium ore-forming brines in the Athabasca Basin. Figures 3.3I-L show the pH of the system at different times (10,000, 100,000, 340,000, and 500,000 years), confirming that uranium deposits form from uranium-bearing acidic brines in a pH range of about 4-4.5.

At zero years, the concentrations of chlorite, muscovite, and hematite are at their initial values (Figs. 3.4A, 3.4F, and 3.4K). Figures 3.4B, 3.4G, and 3.4L show the pre-mineralization alteration of chlorite, muscovite, and hematite occurring at 10,000 years, before the formation of uraninite at 100,000 years. The pre-mineralization alteration includes the subtle precipitation of these minerals at the bottom of the basement. Syn-mineralization alteration of chlorite and muscovite (Figs. 3.4C-E and 3.4H-J), which occurs during precipitation of uraninite, includes precipitation of these minerals in the basement and around the uranium deposit. Chlorite is subject to precipitation in the basement and along the fault zone, whereas precipitation of muscovite occurs only in the basement. Dissolution of the muscovite is prevalent along the fault zone. In both pre- and syn-mineralization stages, hematite precipitates in the basement. It should be noted that in

the pre-ore mineralization stage at 10,000 years, the volume fraction of precipitated hematite at the bottom of the basement (Fig. 3.4L) is less than that in the syn-mineralization alteration stage (Figs. 3.4M-O). During the syn-mineralization alteration stage, hematite precipitates simultaneously with uraninite in the reducing environment of the basement and forms an alteration halo around the uranium ore deposit. In addition, at this stage the volume fraction of precipitated hematite in the basement decreases continuously with time (Figs. 3.4M-O).

3.4.2 Basement as a source of uranium

Figure 3.5A shows the fluid flow pattern and flow rate around the fault zone. Similar to the model with uranium sourced in the sandstone, the maximum flow rate occurs along this zone that serves as a pathway for transporting fluids. Figures 3.5B-E show the fluid flow, temperature distribution and uranium mineralization throughout the model area at different times. At 10,000 years (Fig. 3.5B) and 100,000 years (Fig. 3.5C), two major and three minor convection cells develop within the sandstone unit; whereas at 380,000 years (Fig. 3.5D), one major and four minor convection cells have developed. At this time the system approaches steady-state conditions implying that the fluid flow pattern and temperature distribution do not change after 380,000 years.

Prior to 380,000 years, no uraninite precipitates (Figs. 3.5F and 3.5G). At about 380,000 years (Fig. 3.5H), uraninite begins to precipitate in the basement (800 meters below the unconformity interface and 375 meters away from fault and unconformity interface intersection), with a volume fraction of about 0.0064 (equivalent to a uranium grade of 0.26 %). This grade of uranium is higher than that of well-known basement-

hosted deposits in the Alligator Rivers region, Australia (with an average uranium grade 0.08 to 0.04 % U_3O_8), and comparable with Canadian counterparts such as the Collins Bay deposit in the Athabasca Basin (with an average uranium grade of 0.25 %) (Tremblay, 1982; Fryer and Taylor, 1984). Assuming the uranium source in the basement, uraninite precipitates relatively late in comparison with the model that considers the sandstone as the source of uranium. Permeability of the basement is much lower than that of the sandstone, making the circulation and interaction of the uranium-bearing fluids with the ferrous iron less efficient in the basement. This may explain why uraninite precipitates later relative to the sandstone model. Also, the volume fraction of the precipitated uraninite is now less than that of the sandstone model. Although the same initial concentration of UO_2^{2+} is used in both models, the concentration of UO_2^{2+} surrounding the deposit at the beginning of uraninite precipitation is 6.183×10^{-10} ppm for the second model, almost one order of magnitude lower than that for the first model (5.157×10^{-9} ppm). This may explain why the modeled mineralization has a lower grade in the second model.

Alteration minerals associated with the modeled uranium deposit at 500,000 years are predominantly muscovite (Fig. 3.6A) rather than chlorite (Fig. 3.6B) and muscovite. Muscovite precipitates in the basement (and also around the uranium deposits) and dissolves along the fault zone, whereas chlorite is mainly subject to precipitation along the fault zone. Similar to the model with uranium sourced in the sandstone, hematite (Fig. 3.6C) simultaneously precipitates in the basement and forms an alteration halo in the vicinity of the uranium deposit.

3.4.3 Sensitivity analysis

Faulting and fracturing of the basement and overlying sandstone have an important role in enhancing fluid flow, focusing mineralizing fluids, and controlling the deposition of the ore in all URU deposits (Needham and Stuart–Smith, 1980; Wilson and Kyser, 1987; Raffensperger and Garven, 1995a; Jefferson et al., 2007). In the present study, in order to decipher the effect of the fault zone permeability on the uranium mineralization, a sensitivity analysis is carried out for both models, by assigning higher permeability values (10^{-11} m^2 and 10^{-10} m^2) to the fault zone while remaining the other physical properties are unchanged.

The fluid flow pattern, temperature distribution and uraninite precipitation for the first model at 500,000 years are presented in Figs. 3.7A and 3.7E, subject to a permeability of 10^{-11} m^2 for the fault zone. Figure 3.7C shows the fluid flow vectors around the fault zone, depicting that enhancing the permeability of the fault zone from 10^{-12} m^2 to 10^{-11} m^2 increases the maximum flow rate along this zone (compare Figs. 3.2A with 3.7C) from 7×10^{-8} m/s (2.2 m/year) to 2.2×10^{-7} m/s (6.9 m/year). Now two convection cells develop in the basinal sandstone (Fig. 3.7A), separated by the fault zone. Consequently uraninite precipitates in the basement along the fault zone with a maximum volume fraction of 0.011 (equivalent to a uranium grade of about 0.43 %) (Fig. 3.7E). Figures 3.7B and 3.7F show the simulation results for the first model when the permeability of the fault zone is further increased to a value of 10^{-10} m^2, exhibiting a generally similar fluid flow pattern with a slightly larger uraninite deposit in size and volume fraction. Following this permeability enhancement, the fluid flow rate along the fault zone (Fig. 3.7D) increases substantially with a maximum Darcy velocity of 7.1×10^{-7}

m/s (about 22.3 m/year). For the second model, uraninite precipitation is illustrated in Figs. 3.7G and 3.7H, respectively corresponding to a permeability of 10^{-11} m^2 and 10^{-10} m^2. In Fig. 3.7G, uraninite precipitation occurs along the fault zone slightly below the unconformity with a lower volume fraction of 0.007 (equivalent to a uranium grade of 0.29 %) compared with that of the first model (0.011). It should be pointed out that in the second model, uraninite precipitation occurs not only in the basement along the fault but also extends to above the unconformity when the fault permeability is further increased to 10^{-10} m^2 (Fig. 3.7H). Figures 3.8A-D show the ore forming brines pH regime in the model area, for the first and second models, subject to the fault zone permeabilities of 10^{-11} m^2 and 10^{-10} m^2. Similarly, these figures also show that uraninite precipitates in the areas with a pH of about 4.5.

Alteration minerals for the first model at 500,000 years are depicted in Figs. 3.9A-F, respectively subject to the fault zone permeabilities of 10^{-11} m^2 and 10^{-10} m^2. Chlorite precipitation (Figs. 3.9A-B) is pervasive in the basement; whereas muscovite (Figs. 3.9C-D) shows a precipitation pattern in the basement and a dissolution pattern along the fault zone. For the second model, chlorite (Figs. 3.10A-B) precipitates mainly along the fault zone, while muscovite (Figs. 3.10C-D) dissolves along this zone and precipitates in the basement. Once again, hematite (Figs. 3.9E-F and Figs. 3.10E-F) forms an alteration halo in the basement for both the first and second models when the fault has a greater permeability.

In addition, we also simulated several scenarios with a variety of volume fraction of chlorite in the basement. It was discovered that the higher the volume fraction of chlorite,

the higher the uraninite grade will be; and vice versa. However, the location of the precipitated uraninite does not change with the volume fraction of chlorite.

3.5 **Interpretation**

The fault zone provides a pathway for interaction of the basinal brines with the basement rocks and for the basal fluids with the sandstone lithology. The permeability of the fault zone governs the convection pattern in the sandstone unit and the flow rate within the fault zone. Convective flow driven by the thermally-induced buoyancy develops within the sandstone unit (refer to Figs. 3.2B-E and 3.5B-E), leaches the uranium from the source rocks and interacts with the basement lithology. Aqueous uranium in the sandstone interacts with the other aqueous species through fluid convection to form uranium complexes and also uraninite. This fluid flow pattern is consistent with the genetic model of typical URU deposits in sedimentary basins (e.g., Hoeve and Sibbald, 1978; Hoeve and Quirt, 1984; Sibbald et al., 1991).

The results illustrated in Figs. 3.2G-I and 3.5H-I confirm that uraninite can precipitate in the basement away from the fault zones, which is consistent with some field observations. For instance, the Centennial deposit in the south-central Athabasca Basin is distant from the Dufferin Lake fault that is a major fluid conduit in the area (Alexandre et al., 2012).

The alteration zones for basement-hosted deposits are commonly chlorite and muscovite (Fayek and Kyser, 1997; Thomas et al., 1998; Alexandre et al., 2005; Cloutier et al., 2009). In the present work, pre-mineralization alteration of chlorite (Fig. 3.4B) provides the ferrous iron required for precipitation of uraninite and hematite. The

concentration of Fe^{2+} (Fig. 3.3E) is increased in the basement from an initial concentration of 0.002 to a maximum value of about 0.05. This is because, based on the reaction (3.1), dissolution of pre-mineralization stage chlorite releases the Fe^{2+} into the solution. Consequently, accumulation of Fe^{2+} in the basement contributes to the formation of uraninite and hematite according to the reaction (3.2). For the model with the source of uranium in the sandstone, syn-mineralization alteration minerals are chlorite and muscovite, which are commonly found in basement-hosted deposits in the Athabasca Basin. Whereas for the model with the source of uranium in the basement, the altered minerals are predominantly muscovite rather than chlorite and muscovite, which is similar to the alteration pattern discovered at Millennium uranium deposit in the Athabasca Basin (Cloutier et al., 2009). For both models, there is an association between hematite precipitation and uranium accumulation, and hematite forms an alteration halo surrounding the uranium deposit. This result is reasonable based on the redox mechanism (reaction 3.2) for precipitation of uraninite. Intense clay alteration zones surrounding the deposits such as Cigar Lake constitute natural geological barriers for uranium migration in groundwaters (Percival et al., 1993), and are important geotechnical factors in mining and ore processing (Andrade, 2002; Jefferson et al., 2007). The presence of the clay alteration zones in the vicinity of the uranium ore deposit (e.g., chlorite (Figs. 3.4C-E)) reduces the permeability of the surrounding area of the uranium deposits, acting as geological barriers for uranium migration.

Sensitivity analysis shows that when the fault zone is hydraulically more permeable, uraninite precipitates along the fault zone in the basement and may also extend above the unconformity interface. In the first model, two nearly equal-size convection cells (Figs.

3.7A and 3.7B) develop. The high flow rate along the fault zone allows this zone to act as a structural trap and lead to uraninite precipitation along it (Figs. 3.7E and 3.7F). This pattern of uranium deposition is similar to that of the Eagle Point uranium deposit in the Athabasca Basin. The Eagle Point deposit is hosted in the basement in the structural hanging wall of a reverse fault (Andrade, 1989). In the second model, uraninite precipitates (Figs. 3.7G and 3.7H) along the fault zone and extends to the area above the unconformity interface, which is comparable with the Deilmann deposit at Key Lake mine in the Athabasca Basin (Harvey and Bethune, 2007). At the Deilmann uranium deposit (open pit, mined out), the uranium ore is situated along the fault zone and extends into the unconformity interface, and comprises both basement-hosted and sandstone-hosted unconformity uranium ore deposits (Collier and Yeo, 2001; Harvey and Bethune, 2007). The pH of the ore-forming brines along the fault zone (Fig. 3.8) also has a contributing role in the precipitation pattern of the uraninite. In the first model, with enhanced fault zone permeabilities (1×10^{-11} m^2 and 1×10^{-10} m^2), the pH along the fault zone below the unconformity is about 4.5; whereas it is about 1.9 above the unconformity-interface. This drop in pH causes uraninite to precipitate only along the fault zone that is below the unconformity interface, leading to the formation of a basement-hosted URU deposit. In the second model, however, the pH in the entire fault zone is about 4.5. That is why uraninite precipitates not only along the fault zone in the basement but also extends over the unconformity, and leads to the formation of a hybrid-type URU deposit. In addition, our sensitivity analysis also indicates that the volume fraction of the chlorite in the basement affects the uraninite grade. The lower the chlorite volume fraction, the lower the precipitated uraninite grade; and vice versa. However, the

location of the precipitated uraninite does not change with variations in the chlorite fraction.

This research suggests that the first model favors the formation of large uranium deposits with a high uraninite grade (comparing Fig. 3.2G with Fig. 3.5H, Fig. 3.7E with Fig. 3.7G, and Fig. 3.7F with Fig. 3.7H), and it also shares common features of the basement-hosted URU deposits in terms of alteration zones. In the second model, both the aqueous uranium source and reducing fluids are in the basement. Because of the lower permeability of the basement, interaction of these brines is less efficient compared with that in the first model with the uranium source in the sandstone and the reducing fluids in the basement. This highlights the importance of the sandstone aquifer as the uranium source in the formation of giant URU deposits.

This research along with our previous study (Aghbelagh and Yang, 2014) represents the first computational attempt to understand the formation of basement-hosted URU deposits. Recent works (e.g., Cloutier et al., 2009; Reid et al., 2010) reveal that even for similar types of URU deposits, mineralization features could be different from one deposit to another. The Centennial deposit located in the south-central part of the Athabasca Basin, for example, shares similarities with its counterparts in the eastern part of the basin, but also incorporates distinguished features (Reid et al., 2010). Association of the deposit with the basement units, clay alteration enveloping the mineralization and a brittle deformation zone extending from the basement into the sandstone are considered as features which are similar to other URU deposits (Reid et al., 2010). The features that distinguish this deposit from others include insignificant amounts of graphite in basement rocks that underlie mineralization and lack of significant post-Athabasca structural

displacement (Reid et al., 2010). The Millennium uranium deposit is another atypical example of URU deposits (Cloutier et al., 2009). In this deposit, the associated alteration zone mainly includes muscovite rather than the chlorite and muscovite commonly found in the other basement-hosted deposits of the Athabasca Basin (Cloutier et al., 2009). Hence, more up-to-date geochemical and mineralogical data would be crucial and beneficial in developing realistic reactive mass transport models in order to gain better insight into the ore-forming processes. From an exploration point of view, this research confirms that URU deposits can be formed in the absence of graphitic zones. In addition, it provides an additional insight for precipitation of the uraninite either along the fault zone or away from this zone. Lastly, it highlights the importance of the alteration mineralogy and geochemistry of the URU deposits and the host rocks in exploration of these deposits.

3.6 Conclusions

Fe-rich chlorite has been evaluated as an inorganic-based reducing agent in the formation of URU deposits by incorporating the redox process of uraninite precipitation in a reactive transport model. Our simulation results confirm that Fe^{2+}, released into solution by the destruction of Fe-rich chlorite, is capable of reducing the oxidized uranium present in the solution and leading to precipitation of uraninite, even if there is no graphite present. Two reactive mass transport models are developed: one considers the sandstone as a source of uranium, and the other assumes the basement as the uranium source. Our simulation results also show that permeability of the fault zone controls the location of uraninite. A hydraulically more permeable fault tends to precipitate the uraninite along

the fault zone in the basement and above the unconformity interface, and a relatively less permeable fault likely gives rise to a distal locale of uranium mineralization from the fault. Both models account for uranium mineralization. The first model produces a higher grade of uraninite, and shares common features of basement-hosted URU deposits in terms of alteration zones. It exhibits chlorite and muscovite alteration zones, as discovered in most of the basement-hosted URU deposits, whereas the alteration zones in the second model are predominantly in the form of muscovite. Favorable physicochemical conditions such as pressure, temperature, oxygen fugacity and pH are also important for the formation of uranium deposits. Uraninite precipitates simultaneously with hematite in the areas experiencing a reduction of oxygen fugacity and having a temperature of 180 °C and a pH range of about 4-4.5. The result of this study is of importance for mineral exploration companies. Traditionally the exploration sector makes use of faulted graphite zones as indicators of URU deposits since some of the more well-known URU deposits are associated with graphitic units. However, the present work confirms that URU deposits can form in the absence of any graphite zones. Therefore, the exploration sector should also consider running discovery programs in areas not exhibiting the presence of graphitic units. In addition, our research also reveals the importance of the alteration mineralogy and geochemistry of URU deposits and the host rocks as exploration signatures.

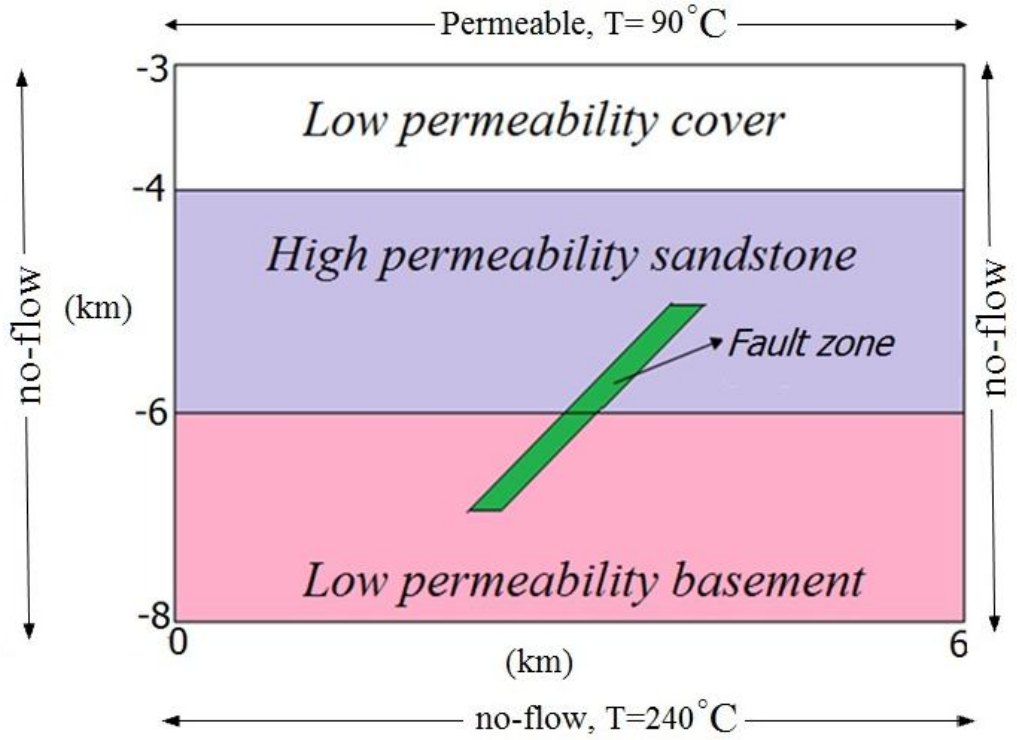

Fig. 3.1. Conceptual model used in the simulation of URU deposits (based on previous studies by Raffensperger and Garven, 1995b, Cui et al., 2012, and Aghbelagh and Yang, 2014).

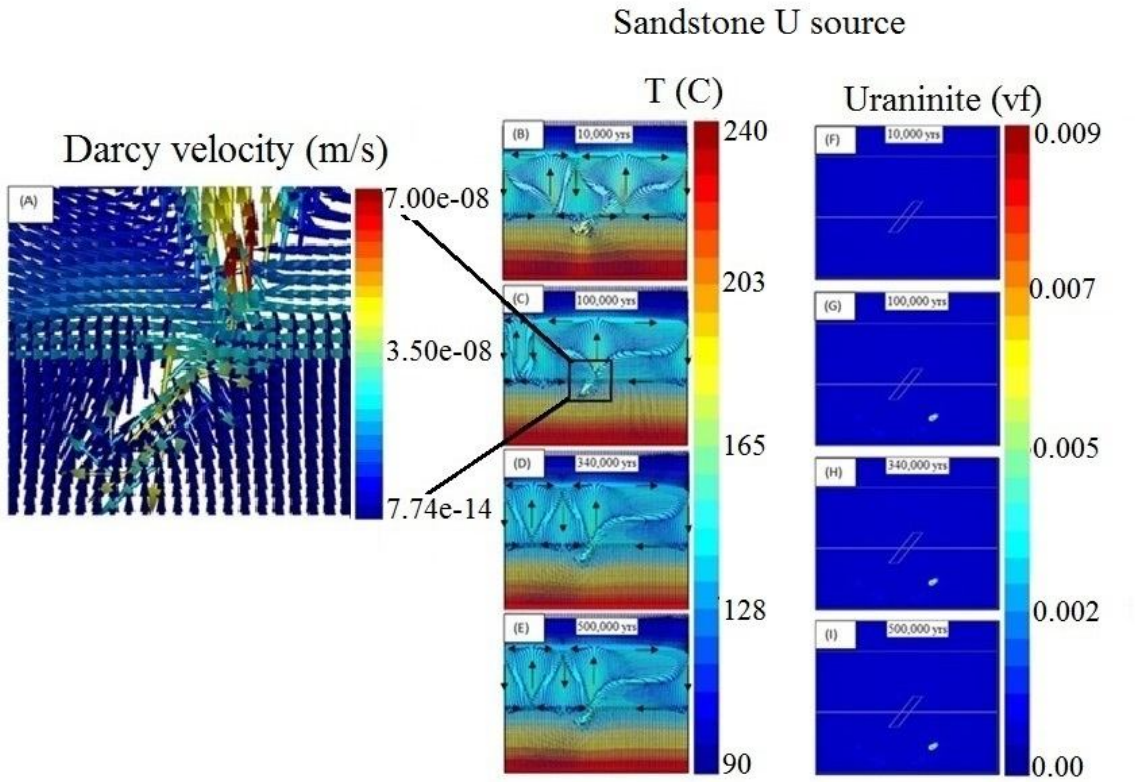

Fig. 3.2. Fluid flow pattern and flow rate, temperature distribution, and uraninite precipitation for the first model (sandstone as a uranium source) at different times. (A) Fluid flow pattern and flow rate around the fault zone for at 100,000 years, (B-E) fluid flow pattern and temperature distribution at 10,000, 100,000, 340,000, and 500,000 years, and (F-I) uraninite precipitation at 10,000, 100,000, 340,000, and 500,000 years.

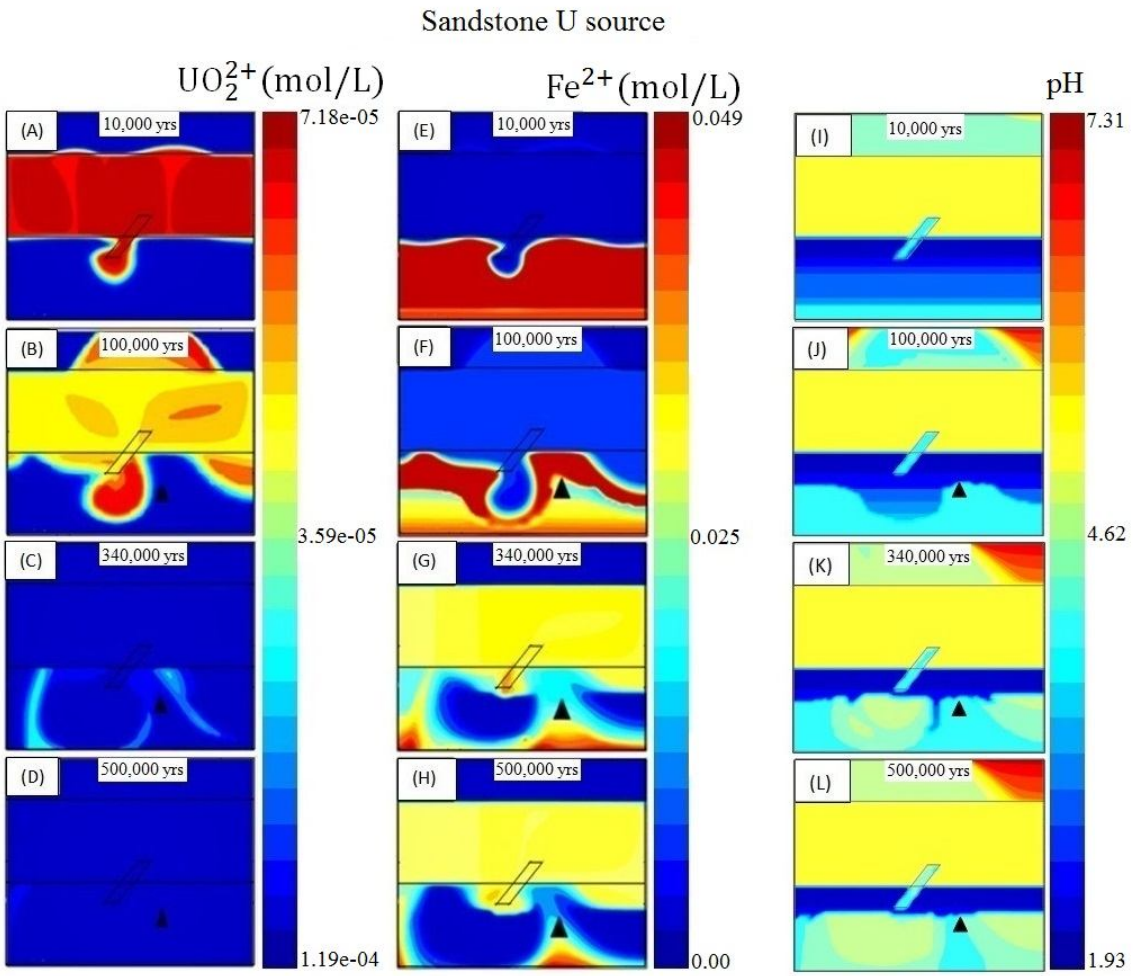

Fig. 3.3. Concentration of UO_2^{2+} and Fe^{2+}, and pH regime for the first model (sandstone as a uranium source) at different times. (A-D) concentration of UO_2^{2+} at 10,000, 100,000, 340,000, and 500,000 years, (E-H) concentration of Fe^{2+} at 10,000, 100,000, 340,000, and 500,000 years, and (I-L) pH at 10,000, 100,000, 340,000, and 500,000 years. The black triangle shows the location of the precipitated uraninite.

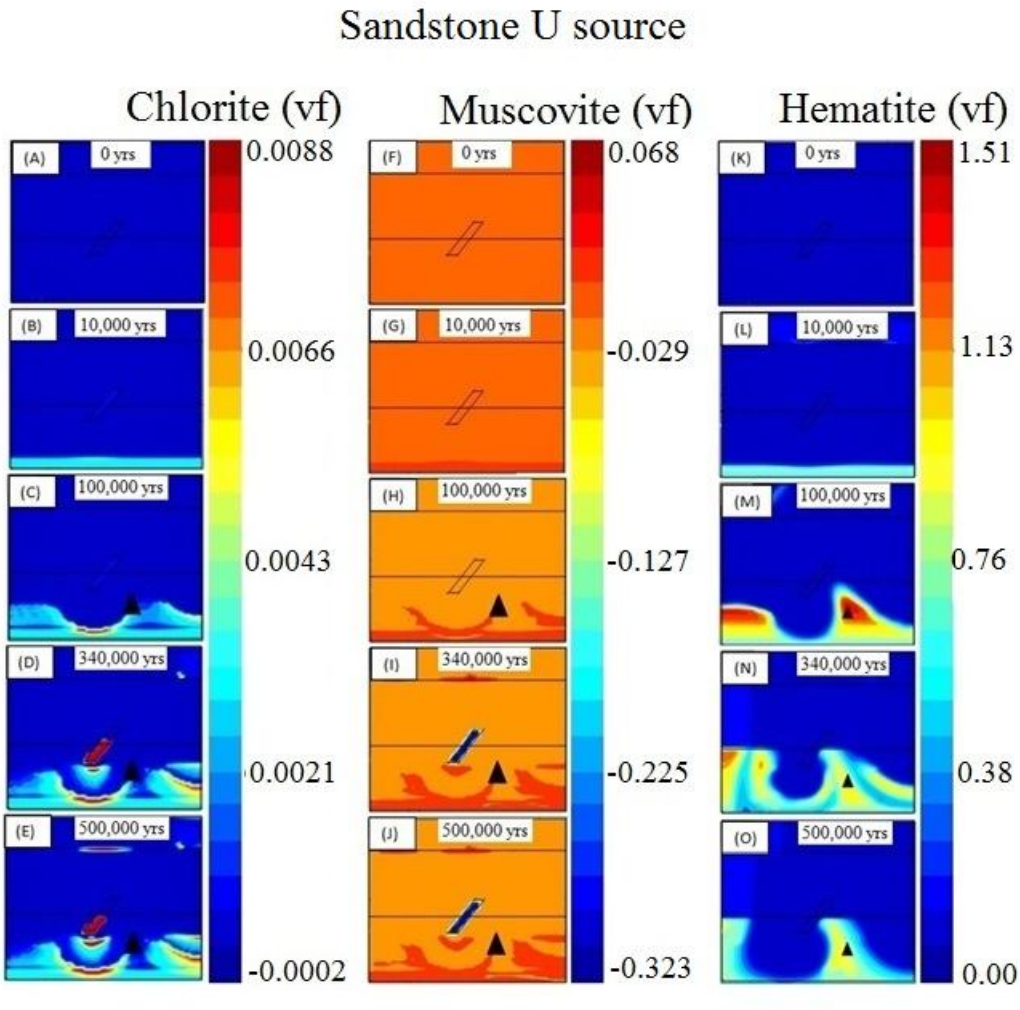

Fig. 3.4. Pre-mineralization (at 0 and 10,000 years) and syn-mineralization alterations (at 100,000, 340,000, and 500,000 years) of the chlorite, muscovite, and hematite for the first model (sandstone as a uranium source). (A-B) chlorite pre-mineralization alterations, (C-E) chlorite syn-mineralization alterations, (F-G) muscovite pre-mineralization alterations, (H-J) muscovite syn-mineralization alterations, (K-L) hematite pre-mineralization alterations, and (M-O) hematite syn-mineralization alterations. Positive values for the volume fraction refer to precipitation of the mineral and negative values refer to dissolution of the mineral. The black triangle shows the location of the precipitated uraninite.

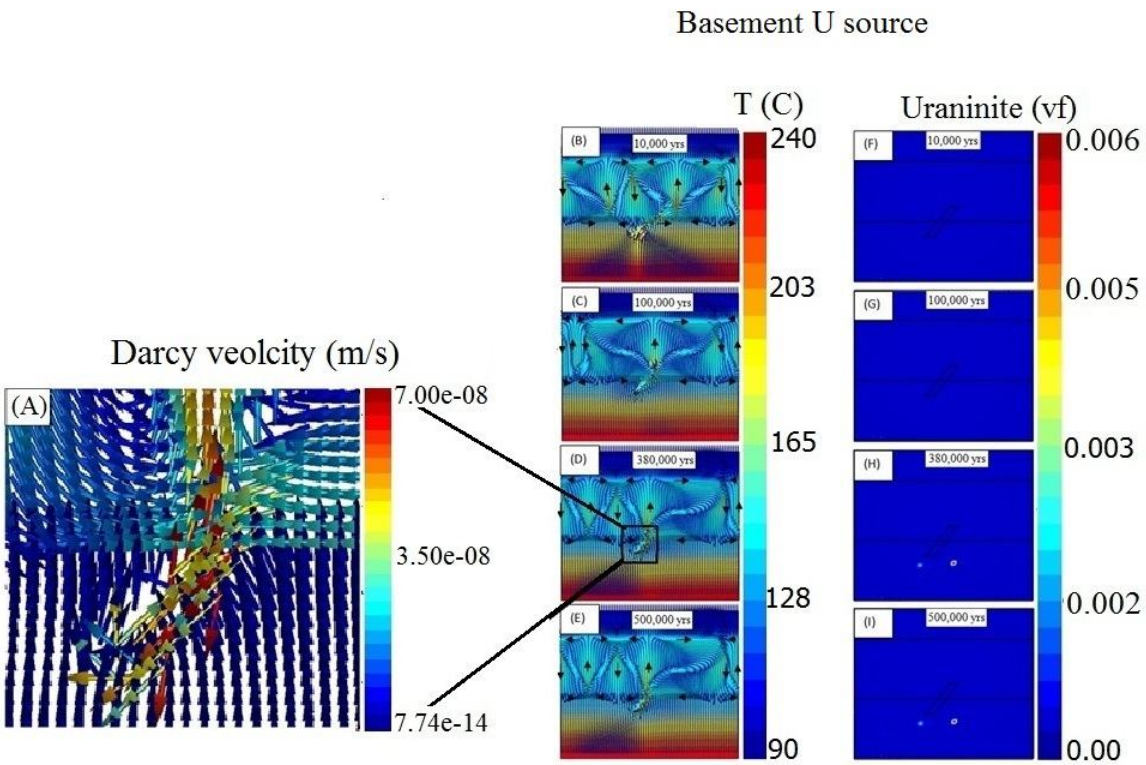

Fig. 3.5. Fluid flow pattern and flow rate, temperature distribution, and uraninite precipitation for the second model (basement as a uranium source) at different times. (A) Fluid flow pattern and flow rate around the fault zone at 380,000 years, (B-E) fluid flow pattern and temperature distribution at 10,000, 100,000, 380,000, and 500,000 years, and (F-I) uraninite precipitation at 10,000, 100,000, 380,000, and 500,000 years.

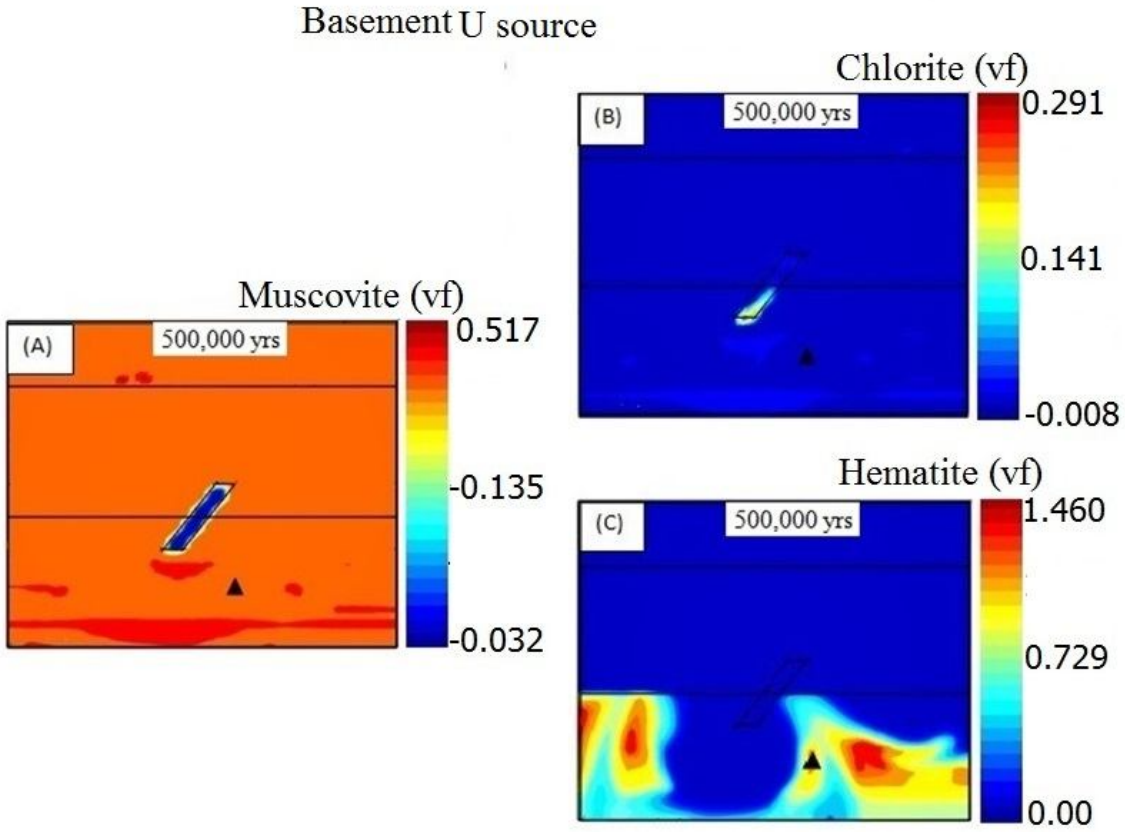

Fig. 3.6. Alteration minerals for the second model (basement as a uranium source) at 500,000 years. (A) muscovite alterations (B) chlorite alterations, and (C) hematite alterations. Positive values for the volume fraction refer to precipitation of the mineral and negative values refer to dissolution of the mineral. The black triangle shows the location of the precipitated uraninite.

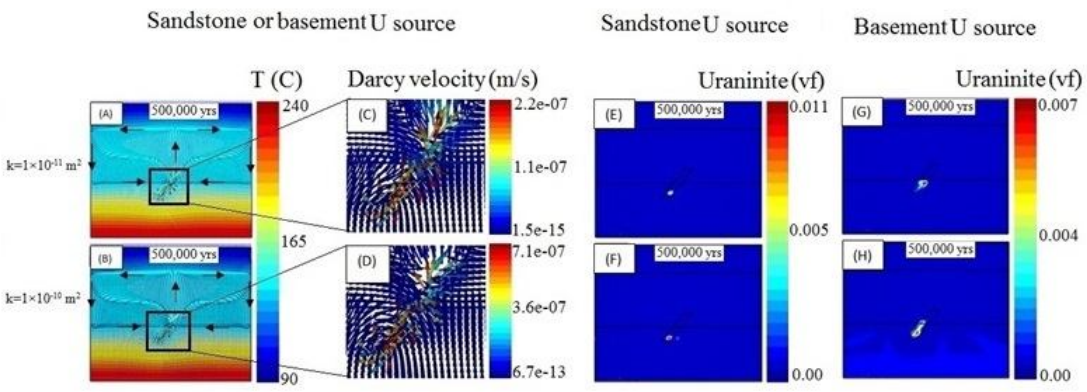

Fig. 3.7. Fluid flow pattern and flow rate, temperature distribution, and uraninite precipitation in the first (sandstone as a uranium source) and second (basement as a uranium source) models at 500,000 years, subject to a permeability of 10^{-11} m^2 and 10^{-10} m^2 for the fault zone. (A-B) fluid flow pattern and temperature distribution, (C-D) fluid flow vectors around the fault zone, (E-F) uraninite precipitation for the first model, and (G-H) uraninite precipitation for the second model.

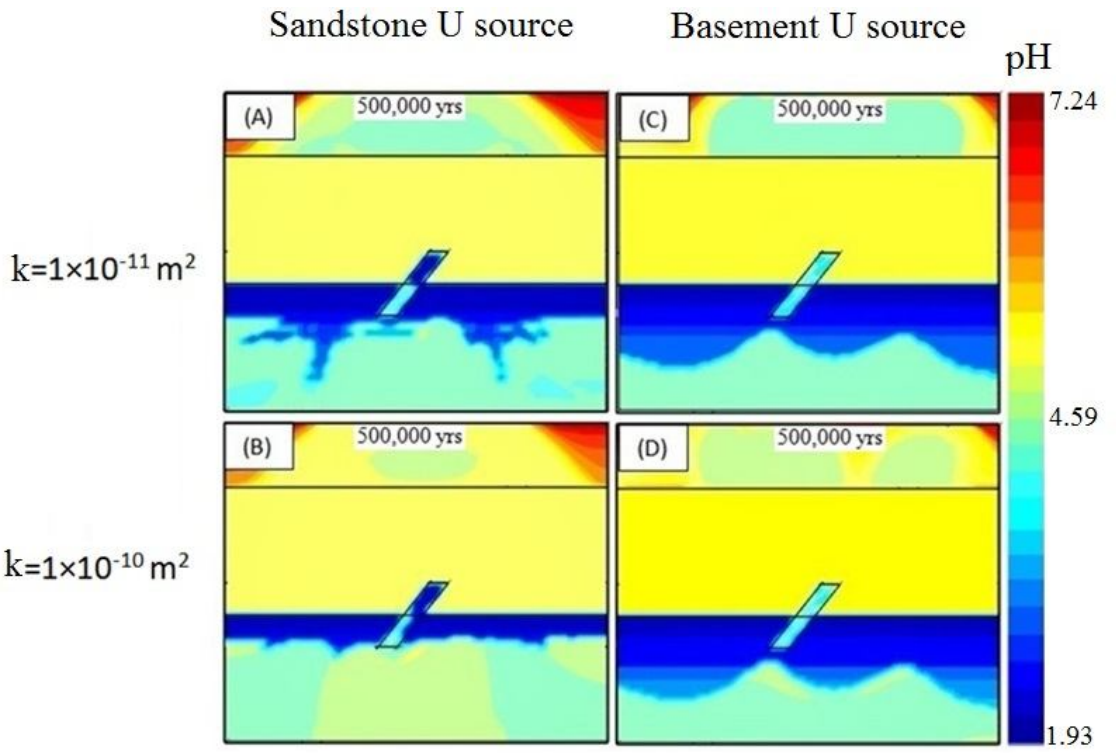

Fig. 3.8. pH regime for the first (sandstone as a uranium source) and second (basement as a uranium source) models at 500,000 years, subject to a permeability of 10^{-11} m^2 and 10^{-10} m^2 for the fault zone. (A-B) for the first model, and (C-D) for the second model.

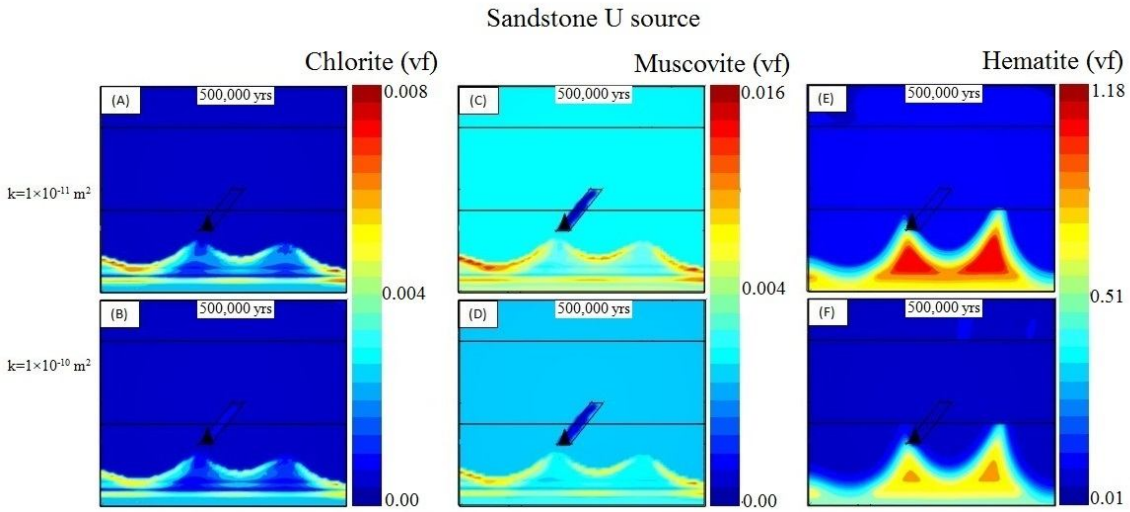

Fig. 3.9. Alteration minerals for the first model (sandstone as a uranium source) at 500,000 years, subject to a permeability of 10^{-11} m^2 and 10^{-10} m^2 for the fault zone. (A-B) chlorite alterations, (C-D) muscovite alterations, and (E-F) hematite alterations. Positive values for the volume fraction refer to precipitation of the mineral and negative values refer to dissolution of the mineral. The black triangle shows the location of the precipitated uraninite.

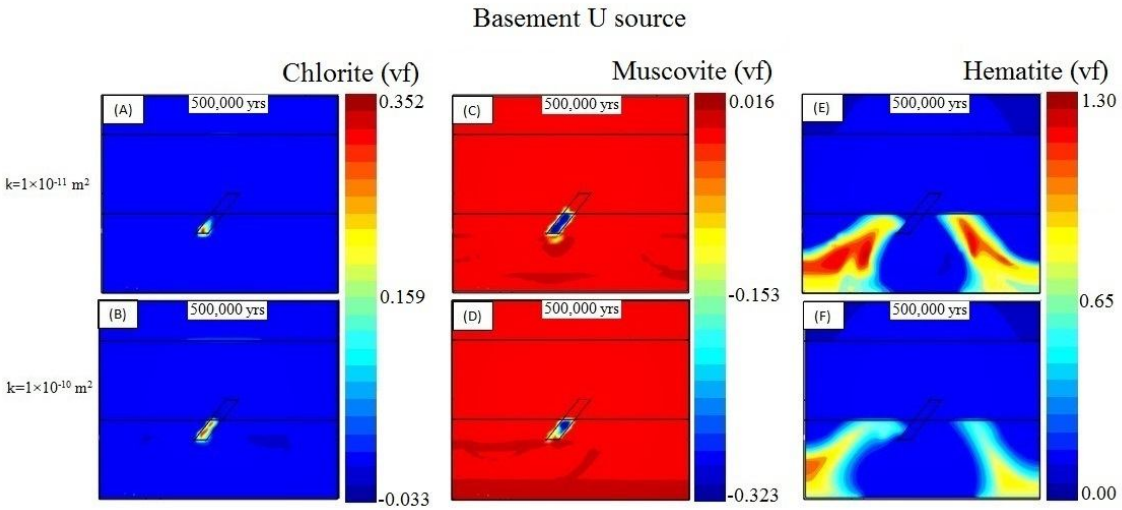

Fig. 3.10. Alteration minerals for the second model (basement as a uranium source) at 500,000 years, subject to a permeability of 10^{-11} m^2 and 10^{-10} m^2 for the fault zone. (A-B) chlorite alterations, (C-D) muscovite alterations, and (E-F) hematite alterations. Positive values for the volume fraction refer to precipitation of the mineral and negative values refer to dissolution of the mineral.

References

Acevedo, A. and Kyser, T.K., 2015, Fe Isotopic Composition of Alteration Minerals From McArthur River Zone 4 Deposit, Athabasca Basin, Saskatchewan, in Targeted Geoscience Initiative 4: unconformity-related uranium systems, (ed.) E.G. Potter and D.M. Wright: Geological Survey of Canada, Open File 7791, p. 61-73. doi:10.4095/295776.

Adlakha, E.E., Hattori, K., Zaluksi, G., Kotzer, T., and Potter, E.G., 2014, Alteration within the basement rocks associated with the P2 fault and the McArthur River uranium deposit, Athabasca Basin; Geological Survey of Canada, Open File 7462, 35 p. doi:10.4095/293364.

Aghbelagh, Y. B., and Yang, J., 2014, Effect of graphite zone in the formation of unconformity-related uranium deposits: Insights from reactive mass transport modeling: Journal of Geochemical Exploration, v. 144, p. 12-27.

Alexandre, P., and Kyser, K., 2006, Geochemistry of uraniferous bitumen in the southwest Athabasca basin, Saskatchewan, Canada: Economic Geology, v. 101, p. 1605-1612.

Alexandre, P., Kyser, K., Jiricka, D., and Witt, G., 2012, Formation and evolution of the Centennial unconformity-related uranium deposit in the South-Central Athabasca Basin, Canada: Economic Geology, v. 107, p. 385-400.

Alexandre, P., Kyser, K., Polito, P., and Thomas, D., 2005, Alteration mineralogy and stable isotope geochemistry of Paleoproterozoic basement-hosted unconformity-type deposits in the Athabasca Basin, Canada: Economic Geology, v. 100, p. 1547-1563.

Alexandre, P., Kyser, K., Thomas, D., Polito, P., and Marlat, J., 2009, Geochronology of unconformity-related uranium deposits in the Athabasca Basin, Saskatchewan, Canada and their integration in the evolution of the basin: Mineralium Deposita, v. 44, p. 41-59.

AMEC Americas Limited, 2014. Uranium Mining Supply Chain Requirement Guide, Saskatchewan Ministry of the Economy, AMEC file: 176123RE006.

Andrade, N., 2002, Geology of the Cigar Lake uranium deposit, in Andrade, N., Breton, G., Jefferson, C.W., Thomas, D.J., Tourigny, G., Wilson, W., and Yeo, G.M., eds., The Eastern Athabasca Basin and Its Uranium Deposits: Field Trip A-1 Guidebook: Saskatoon: Geological Association of Canada and Mineralogical Association of Canada, p. 53-72.

Andrade, N., 1989, The Eagle Point uranium deposits, northern Saskatchewan, Canada: Uranium Resources and Geology of North America, Technical Committee Meeting, Saskatoon, Vienna, 1-3 September, 1987, Proceedings, p. 429-454.

Annesley, I.R., and Madore, C. 1999, Leucogranites and pegmatites of the sub-Athabasca basement, Saskatchewan: U protore? In Mineral deposits: processes to processing. Edited by C.J. Stanley et al. Balkema, Rotterdam, The Netherlands, v. 1, p. 297–300.

Annesley, I.R., Madore, C., and Cutler, J., 2001, Synchrotron X-ray analyses of graphitic pelitic gneisses in the vicinity of unconformity-type uranium mineralization, in Summary of Investigations, Volume 2: Saskatchewan Geological Survey, Miscellaneous Report 2001-4.2, p. 132-140.

Bahr, J.M., 1990, Kinetically influenced terms for solute transport affected by heterogeneous and homogeneous classical reactions: Water Resources Research, v. 26, p. 21-34.

Bear, J. 1972, Dynamics of fluids in porous materials: New York, Elsevier (reprinted by Dover Publications, 1988), 784 p.

Bethke, C.M., 1996, Geochemical reaction modeling-Concepts and applications. Oxford University Press, New York, NY.

Boiron, M. C., Cathelineau, M., and Richard, A, 2010, Fluid flows and metal deposition near basement/cover unconformity: Lessons and analogies from Pb-Zn-F-Ba systems for the understanding of Proterozoic U deposits: Geofluids, v. 10, p. 270-292.

Bray, C. J., Spooner, E. T. C., Golightly, J. P., and Saracoglu, N., 1982, Carbon and sulphur isotope chemistry of unconformity-related uranium mineralization, McClean Lake deposits, N., Saskatchewan, Canada: Geological Society of America, Abstracts with programs, v. 14, 451 p.

Cameco annual report, 2014, www.cameco.com/annual_report/2014/

Cheney, E.S., 1985, Similarities between roll-front and Athabasca unconformity-type uranium deposits and the possible role of sulphides in their origin: In Geology of Uranium Deposits, Edited by T.I.I. Sibbald and W. Petruk, CIM special volume. 32, 268 p.

Chi, G., Bosman, S., and Card, C., 2013, Numerical modeling of fluid pressure regime in the Athabasca basin and implications for fluid flow models related to the unconformity-type uranium mineralization: Journal of Geochemical Exploration, v. 125, p. 8-19.

Cloutier, J., Kyser, K., Olivo, G. R., Alexandre, P., and Halaburda, J., 2009, The Millennium uranium deposit, Athabasca Basin, Saskatchewan, Canada: An atypical basement-Hosted unconformity-related uranium deposit: Economic Geology, v. 104, p. 815-840.

Collier, B., and Yeo, G.M., 2001, Stratigraphy of the Paleoproterozoic Manitou Falls B member at the Deilmann Pit, Key Lake, Saskatchewan: in Summary of Investigations, 2001, Volume 2: Saskatchewan Geological Survey, Saskatchewan Energy and Mines, Report 2001-4.2, p. 297-305.

Cui, T., Yang, J., and Samson, I. M., 2012a, Tectonic deformation and fluid flow: Implications for the formation of unconformity-related uranium deposits: Economic Geology, v. 107, p. 147-163.

Cui, T., Yang, J., and Samson, I. M., 2012b, Uranium transport across basement/cover interfaces by buoyancy-driven thermohaline convection: implications for the formation of unconformity-related uranium deposits: American Journal of Science, v. 312, p. 994-1027.

Cuney, M., 2009, The extreme diversity of uranium deposits: Mineralium Deposita, v. 44, p. 3-9.

Cuney, M., and Kyser, K., 2009, Recent and not-so-recent developments in uranium deposits and implications for exploration: Mineralogical Association of Canada, Short Course Series, v. 39, 257 p.

De Veslud, C.L.C., Cuney, M., Lorilleux, G., Royer, J.-J., and Jébrak, M., 2009, 3D modeling of uranium-bearing solution-collapse breccias in Proterozoic sandstones

(Athabasca Basin, Canada)-Metallogenic interpretations: Computers & Geosciences, v. 35, p. 92-107.

Derome, D., Cathelineau, M., Cuney, M., Fabre, C., Lhomme, T., and Banks, D. A., 2005, Mixing of Sodic and Calcic Brines and Uranium Deposition at McArthur River, Saskatchewan, Canada: A Raman and Laser-Induced Breakdown Spectroscopic Study of Fluid Inclusions: Economic Geology, v.100, p. 1529-1545.

Derome, D., Cuney M., Cathelineau, M., Dubessy, J., and Bruneton, P., 2003, A detailed fluid inclusion study in silicified breccias from the Kombolgie sandstones (Northern Territory, Australia): Application to the genesis of Middle-Proterozoic unconformity-type uranium deposits: Journal of Geochemical Exploration, v. 80, p. 259-275.

Derome, D., Cuney, M.L., Cathelineau,M., Fabre, C., Lhomme, T., 2002, Reconstitution of individual fluid inclusion composition using microthermometry, Raman and laser induced breakdown spectroscopy. Application to the Shea Creek U deposit (Saskatchewan, Canada) (poster): In: Proceedings of the Geological Association of Canada, Mineralogical Association of Canada Annual Meeting, Saskatoon, 27pp.

Fayek M. and Kyser T. K., 1997, Characterization of multiple fluid events and rare-earth-element mobility associated with formation of unconformity-type uranium deposits in the Athabasca Basin, Saskatchewan: Canadian Mineralogist, v. 35, p. 627–658.

Freeze, R. A., and Cherry, J. A., 1979, Groundwater: Englewood Cliffs, N. J., Prentice Hall, 604 p.

Fryer, B. J., and Taylor, R. P., 1984, Sm-Nd direct dating of the Collins Bay hydrothermal uranium deposit, Saskatchewan: Geology, v. 12, p. 479-482.

Fuchs, H., and Hilger, W., 1989, Kiggavik (Lone Gull): An unconformity related uranium deposit in the Thelon Basin, Northwest Territories, Canada: Uranium Resources and Geology of North America: Proceeding of a Technical Committee Meeting, Saskatoon, p. 429-454.

Garven, G., and Freeze, R. A., 1984, Theoretical analysis of the role of groundwater flow in the genesis of stratabound ore deposits: 2. Quantitative results: American Journal of Science, v. 284, p. 1125-1174.

Gustafson, L.B., and Curtis, L.W., 1983, Post-Kombolgie metasomatism at Jabiluka, NT, Australia, and its significance in the formation of high-grade uranium mineralization in Lower Proterozoic rocks: Economic Geology, v. 78, p. 26–56.

Harvey, S.E., and Bethune, K., 2007, Context of the Deilmann orebody, Key Lake mine, Saskatchewan, in Jefferson, C.W., and Delaney, G., eds., EXTECH IV: Geology and Uranium Exploration Technology of the Proterozoic Athabasca Basin, Saskatchewan and Alberta: Geological Survey of Canada, Bulletin 588, (also Geological Association of Canada, Mineral Deposits Division, Special Publication 4; Saskatchewan Geological Society, Special Publication 18), p. 249-266.

Hecht, L., and Cuney, M., 2000, Hydrothermal alteration of monazite in the Precambrian crystalline basement of the Athabasca Basin (Saskatchewan, Canada): implications for the formation of unconformity-related uranium deposits: Mineralium Deposita, v. 35, p. 791-795.

Hiatt, E. E., Kyser, T. K., Fayek, M., Polito, P., Holk, G. J., and Riciputi, L. R., 2007, Early quartz cements and evolution of paleohydraulic properties of basal sandstones

in three Paleoproterozoic continental basins: Evidence from in situ δ18O analysis of quartz cements: Chemical Geology, v. 238, p. 19-37.

Hoeve, J., and Quirt, D., 1984, Mineralization and host rock alteration in relation to clay mineral diagenesis and evolution of the middle Proterozoic, Athabasca basin, northern Saskatchewan, Canada: Saskatchewan Research Counsel Technical Report, 187 p.

Hoeve, J., Rawsthorn, K., and Quirt, D., 1981, Uranium metallogenetic studies: clay mineral stratigraphy and diagenesis in the Athabasca Group: Saskatchewan Research Council Publication, v. 22, p. 76–89.

Hoeve, J., and Sibbald, T.I.I., 1978, On the genesis of Rabbit Lake and other unconformity-type uranium deposits in northern Saskatchewan, Canada: Economic Geology, v. 73, p. 1450–1473.

Hoeve, J., Sibbald, T.I.I., Ramaekers, P., and Lewry, J.F., 1980, Athabasca Basin unconformity-type uranium deposits: a special class of sandstone-type uranium deposit: in Uranium in the Pine Creek Geosyncline (J. Ferguson & A.B. Goleby, eds.). Int. Atomic Energy Agency (Vienna), 575-594.

Jefferson, C.W., Thomas, D.J., Gandhi, S.S., Ramaekers, P., Delaney, G., Brisbin, D., Cutts, C., Quirt, D., Portella, P., and Olson, R.A., 2007, Unconformity associated uranium deposits of the Athabasca Basin, Saskatchewan and Alberta, in Goodfellow, W.D., ed., Mineral Deposits of Canada: A Synthesis of Major Deposit-Types, District Metallogeny, the Evolution of Geological Provinces, and Exploration Methods: Geological Association of Canada, Mineral Deposits Division, Special Publication, v. 5, p. 273-305.

Jennings, A.A., 1987, Critical chemical reaction rates for multicomponent groundwater contamination models: Water Resources Research, v. 23, p. 1775–1784.

Knapp, R.B., 1989, Spatial and temporal scales of local equilibrium in dynamic fluid-rock systems: Geochimica et Cosmochimica Acta 53, 1955-64.

Kojima, S., Takeda, S., and Kogita, S., 1994, Chemical factors controlling the solubility of uraninite and their significance in the genesis of unconformity-related uranium deposits: Mineral Deposita, v. 29, p. 353-360.

Komninou, A., and Sverjensky, D.A., 1996, Geochemical modeling of the formation of an unconformity-type uranium deposit: Economic Geology, v. 91, p. 590-606.

Kotzer, T.G., and Kyser, T.K., 1995, Petrogenesis of the Proterozoic Athabasca Basin, northern Saskatchewan, Canada, and its relation to diagenesis, hydrothermal uranium mineralization and Paleohydrology: Chemical Geology, v. 120, p. 45–89.

Kyser, T. K., Wilson, M. R., and Ruhrmann, G., 1989, Stable isotope constraints on the role of graphite in the genesis of unconformity-type uranium deposits: Canadian Journal of Science, v. 26, p. 490-498.

Lasaga, A.C., 1984, Chemical kinetics of water-rock interactions: Journal of Geophysical Research, v. 89, p. 4009–4025.

Li, Z., Chi, G., Bethune, K.M., Bosman, S.A., and Card, C.D., 2015, Geometric and Hydrodynamic Modelling and Fluid-structural Relationships in the Southeastern Athabasca Basin and Significance for Uranium Mineralization, in Targeted Geoscience Initiative 4: unconformity-related uranium systems, (ed.) E.G. Potter and D.M. Wright: Geological Survey of Canada, Open File 7791, p. 103–114. Doi:10.4095/295776.

Lichtner, P.C., 1996, Continuum formulation of multicomponent-multiphase reactive transport. p. 1–81: In P.C. Lichtner et al. (ed.) Reactive transport in porous media. Reviews in Mineralogy 34, Mineralogical Society of America, Washington, DC.

McCready, A.J., Annesley, I.R., Parnell, J., and Richardson, L.C., 1999, Uranium-bearing Carbonaceous Matter, McArthur River Uranium Deposit, Saskatchewan, in Summary of Investigations 1999: Saskatchewan Geological Survey, Saskatchewan Energy and Mines, p. 110-120.

McGill, B., 1999, The MacArthur River Deposit-A Geological Update, in Uranium Deposit Studies and Exploration Techniques: Saskatchewan Geological Society Special Publication Number 14: MINEXPO'96 SYMPOSIUM - Advances in Saskatchewan Geology and Mineral Exploration, Proceedings of a Symposium, Saskatoon, Saskatchewan, 21-22 November.

Mclellan, J.G., Oliver, N. H. S., and Schaubs, P. M., 2004, Fluid flow in extensional environments: Numerical modelling with an application to Hamersley iron ores: Journal of Structural Geology, v. 26, p. 1157-1171.

Mercadier, J., Richard, A., Boiron, M.C., Cathelineau, M., and Cuney, M., 2010, Migration of brines in the basement rocks of the Athabasca Basin through microfracture networks (P-Patch U deposit, Canada): Lithos, v. 115, p. 121–136.

Narasimhan, T. N., and Witherspoon, P. A., 1976, An integrated finite difference method for analyzing fluid flow in porous media: Water Resource Research, v. 12, p. 57–64.

Needham, R.S., and Stuart –Smith, P.G., 1980, Geology of the alligator River uranium field, in Ferguson, J., and Goleby, A. B., eds., Uranium in the Pine Creek geosyncline: Vinnea, International Atomic Energy Agancy, p. 233-257.

Oliver, N. H. S., McLellan, J. G., Hobbs, B. E., Cleverley, J. S., Ord, A., and Feltrin, L., 2006, Numerical models of extensional deformation, heat transfer, and fluid flow across basement- over interfaces during basin-related mineralization: Economic Geology, v. 101, p. 1-31.

Pagel, M., 1975, De´termination des conditions physico-chimiques de la silicification diage´ne´tique des gre`s Athabasca (Canada) au moyen des inclusions fluides. Comptes Rendus de l'Acade´mie des Sciences, Paris, v. 280, p. 2301–2304.

Parkhurst, D. L., Thorstenson, D. C., and Plummer, L. N., 1980, PHREEQE: A computer program for geochemical calculations: US Geological Survey., Water Resources Investigations Report, p. 80-96, 174 pp.

Peiffert, C., Cuney, M., and Nguyen-Trung, C., 1994, Uranium in granitic magmas: Part 1. Experimental determination of uranium solubility and fluid-melt partition coefficients in the uranium oxide-haplogranite- H2O-Na2CO3 system at 720-770°C, 2 kbar: Geochimica et Cosmochimica Acta, v. 58, p. 2495-2507.

Peiffert, C., Nguyen-Trung, C., and Cuney, M., 1996, Uranium in granitic magmas: Part 2. Experimental determination of uranium solubility and fluid-melt partition coefficients in the uranium oxide-haplogranite-H2O-NaX (X =Cl, F) system at 770°C, 2 kbar: Geochimica et Cosmochimica Acta, v. 60, p.1515-1529.

Percival, J.B., Bell, K., and Torrance, J.K., 1993, Clay mineralogy and isotope geochemistry of the alteration halo at the Cigar Lake uranium deposit: Canadian Journal of Earth Sciences, v. 30, p. 689-704.

Price, L.C., 1997, Minimum thermal stability levels and controlling parameters of methane, as determined by C15+ hydrocarbon thermal stabilities: U.S. Geological Survey, Bulletin 2146-K, p. 136-176.

Raffensperger, J.P., and Garven, G., 1995a, The formation of unconformity- type uranium ore deposits 1. Coupled ground water flow and heat transport modeling: American Journal of Science, v. 295, p. 581-636.

Raffensperger, J.P., and Garven, G., 1995b, The formation of unconformity- type uranium ore deposits 2. Coupled hydrochemical modeling: American Journal of Science, v. 295, p. 639-696.

Ramaekers, P., 1990, Geology of the Athabasca Group (Helikian) in northern Saskatchewan. Saskatchewan Energy and Mines: Saskatchewan Geological Survey, Report 195, 49 p.

Reed, M. H., 1982, Calculation of multicomponent chemical equilibria and reaction processes in systems involving minerals, gases and aqueous phase: Geochimica et Cosmochimica Acta, v. 46, p. 513-528.

Reid, K., Ansdell K., Jiricka, D., Witt, G., and Card, C., 2010, Regional Setting and General Characteristics of the Centennial Unconformity-related Uranium Deposit, Athabasca Basin, Saskatchewan: GeoCanada 2010.

Renac, C., Kyser, T.K., Durocher, K., Dreaver, G., and O'Connor, T., 2002, Comparison of diagenetic fluids in the Proterozoic Thelon and Athabasca Basins, Canada: implications for protracted fluid histories in stable intracratonic basins: Canadian Journal of Earth Sciences, v. 39, p. 113-132.

Richard, A., Pettke, T., Cathelineau, M., Boiron, M. C., Mercadier, J., Cuney, M., and Derome, D., 2010, Brine–rock interaction in the Athabasca basement (McArthur River U deposit, Canada): consequences for fluid chemistry and uranium uptake: Terra Nova, v. 22, p. 303-308.

Richard, A., Rozsypal, C., Mercadier, J., Cuney, M., Boiron M-C, Cathelineau, M., and Banks, D. A., 2012, Giant uranium deposits formed from exceptionally uranium-rich acidic brines. Nature Geoscience, v. 5, p. 142-146.

Rozos, E., and Koutsoyiannis, D., 2005, Application of the Integrated Finite Difference Method in groundwater flow. Geophysical Research Abstracts, European Geosciences Union, Vienna, v. 7, no. 00579.

Ruzicka, V., 1993, Unconformity-type uranium deposits; in Kirkham, R.V., Sinclair, W.D., Thrope, R.I., and Duke, J.M., eds., Mineral Deposits Modeling: Geological Association of Canada, Special paper, v. 40, p. 125-149.

Sibbald, T.I.I., Quirt, D.H., and Gracie, A.J., 1991, Uranium deposits of the Athabasca Basin, Saskatchewan (Field Trip 11): Geological Survey of Canada Open File 2166, 56 p.

Simunek, J. and Valocchi, A.J., 2002, Geochemical Transport, Chapter 6.9 in Methods of Soil Analysis, Part I, Physical Methods , C. Topp and J. Dane, eds. Soil Science Society of America, Madison, WI.

Steefel, C.I., and Lasaga, A.C., 1994, A coupled model for transport of multiple chemical species and kinetic precipitation/dissolution reactions with applications to reactive flow in single phase hydrothermal system: American Journal of Science, v. 294, p. 529–592.

Thomas, D.J., Matthews, R.B., and Sopuck, V.J., 1998, Athabasca basin unconformity-type uranium deposits: A synopsis of the empirical model and review of exploration and production trends: Canadian Institute of Mining, Metallurgy and Petroleum meeting, Montreal 1998, May 3-7, 1998, Proceedings, CD-ROM.

Tremblay, L.P., 1982, Geology of the uranium deposits related to sub-Athabasca unconformity, Saskatchewan: Geological Society of Canada, Paper 81-20.

Valocchi, A.J., 1985, Validity of the local equilibrium assumption for modeling sorbing solute transport through homogeneous soils: Water Resources Research, v. 21, p. 808–820.

Valocchi, A.J., 1988, Theoretical analysis of deviations from local equilibrium during sorbing solute transport through idealized stratified aquifers: Journal of Contaminant Hydrology, v. 2, p. 191-207.

Wilde, A.R., Bloom, M.S., and Wall, V.J., 1989a, Transport and deposition of gold, uranium, platinum-group elements in unconformity- related uranium deposits: Econ. Geol., Monogr., v. 6, p. 637-650.

Wilde, A.R., Mernagh, T.P., Bloom, M.S., and Hoffmann, C.F., 1989b, Fluid inclusion evidence on the origin of some Australian unconformity-related uranium deposits: Economic Geology, v. 84, p. 1627–1642.

Wilde, A.R., Wall, V.G., and Bloom, M.S., 1985, Wall-rock alteration associated with unconformity-related uranium deposits Northern Territorry, Australia: implications for uranium transport and depositional mechanisms: Int. Meet. 'Concentration Mechanisms of Uranium in Geological Environments', Nancy, France, pp 231-239.

Wilson, M. R., and Kyser, T.K., 1987, Stable isotope geochemistry of alteration associated with key lake uranium deposit, Canada: Economic Geology, v. 82, p. 1540-1557.

Wolery, T.J., 1992, EQ3/6: Software package for geochemical modeling of aqueous systems: Package overview and installation guide (version 7.0). Lawrence Livermore National Laboratory Report UCRL-MA-110662 PT I, Livermore, California.

Xu, T., and Pruess, K., 2001, On fluid flow and mineral alteration in fractured caprock of magmatic hydrothermal systems: Journal of Geophysical Research, v. 106, p. 2121–2138.

Xu, T., Ontoy, Y., Molling, P., Spycher, N., Parini, M., Pruess, K., 2004b, Reactive transport modeling of injection well scaling and acidizing at Tiwi Field Philippines: Geothermics, v. 33, p. 477-491.

Xu, T., Sonnenthal, E., Spycher, N., and Pruess, K., 2004a, TOUGHREACT user's guide: A simulation program for nonisothermal multiphase reactive geochemical transport in variably saturated geologic media: Earth Sciences Division, Lawrence Berkeley National Laboratory Report CA 94720, Berkeley, California.

Xu, T., E.L. Sonnenthal, N. Spycher, and Pruess, K., 2006, TOURGHREACT: A simulation program for nonisothermal multiphase reactive geochemical transport in variably saturated geologic media: Computer & Geoscience, v. 32, p. 145-165.

Yang, J., Large, R. R., and Bull, S. W., 2004, Factors controlling free thermal convection in faults in sedimentary basins: Implications for the formation of zinc-lead mineral deposits: Geofluids, v. 4, p. 237-247.

Yeh, G.T., and Tripathi, V.S., 1991, A model for simulating transport of reactive multispecies components: model development and demonstration: Water Resource Research, v. 27, p. 3075–3094.

Yeo, G. M., J.B., Jefferson, C. W., Ickert., and Hunt., P., 2007, Environmental significance of oncoids and crypto-microbial laminites from late paleoproterzoic Athabasca Group, Saskatchewan and Alberta; in Jefferson, C. W. and Delaney, G. (eds.), EXTECH IV: Geology and Uranium Exploration Technology of the Proterozoic Athabasca Bain, Saskatchewan and Alberta: Geological Survey of Canada, Bulletin 588, p. 315-339.

Yeo, G.M., and Potter, E.G., 2010, Review of reducing mechanisms potentially involved in the formation of unconformity-type deposits and their relevance to exploration; in summary of investigations 2010, volume 2: Saskatchewan Geological Survey, Saskatchewan Ministry of Energy and Resources, Misc Report: 2010-4.2, Paper A-12.

Zhao, C., Hobbs, B.E., and Ord, A., 2008, Convective and Advective Heat Transfer in Geological Systems. Springer, Berlin.

Chapter 4[1]

Role of hydrodynamic factors in controlling the formation and location of unconformity-related uranium deposits: insights from reactive flow modeling

4.1 Introduction

Unconformity-related uranium (URU) deposits, hosted by Paleoproterozoic sedimentary basins in Canada and Australia, have formed by large-scale circulation of diagenetic brines that percolated between basinal sandstone and underlying basement rocks (Kyser and Cuney, 2009; Boiron et al., 2010; Morichon et al., 2010; Richard et al., 2012). In these deposits, uranium minerals precipitate via interaction of oxidized uranium-bearing brines with basement-derived reducing fluids or reducing minerals in the basement (redox) according to diagenetic-hydrothermal model (Hoeve et al., 1981; Hoeve and Quirt, 1984). In addition to redox, favorable physicochemical conditions (e.g., temperature, pressure, pH, and oxygen fugacity) are required to form URU deposits over

---

[1] This chapter has been submitted (under review) to the Hydrogeology Journal in a slightly modified form, "Aghbelagh, Y., and Yang, J., 2016. Role of hydrodynamic factors in controlling the formation and location of unconformity-related uranium deposits: insights from reactive flow modeling.

a period of 0.1-1 million years (Raffensperger and Garven, 1995b; Richard et al., 2012; Aghbelagh and Yang, 2014, 2015).

Numerical modeling has provided valuable insights into the formation of URU deposits. Thermal convection has been proposed, for example, by Raffensperger and Garven (1995a) and Cui et al. (2010) as a driving force for circulating fluids in the sandstone and leaching uranium from the source rocks. Cui et al. (2012a) investigated the effect of tectonic deformation on the fluid flow and uranium ore mineralization, and suggested that thermal convection is a dominant driving mechanism for fluid flow in the absence of tectonic deformation. Others (Boiron et al., 2010; Mercadier et al., 2010; Richard et al., 2010; Cui et al., 2012b; Li et al., 2015) have shown that convective flow not only circulates within the sandstone unit, but also percolates into the underlying basement to some depth. Location of the faults in the basement and fault spacing also influence the flow convection pattern within the basinal sandstone (Li et al., 2015).

Understanding the factors controlling the formation and location of URU deposits in sedimentary basins is a major scientific challenge. Hydrodynamic modeling (Chi et al., 2011, 2013; Cui et al., 2012a; Chi and Xue, 2014; Li et al., 2015) showed that during compressive deformation, fluids squeeze upward along faults and form sandstone-hosted deposits (egress type), while during extensional deformation, fluids migrate downward along faults and form basement-hosted deposits (ingress type). In weakly overpressured or zero overpressure regimes, the uranium mineralization occurs near the unconformity interface (Chi et al., 2011, 2013; Chi and Xue, 2014; Li et al., 2015). According to these studies, uraninite can precipitate only along fault zones either in the basement or sandstone, but not in other parts of basin. However, recent geological records (e.g.,

Thomas et al., 2000; Jefferson et al., 2007; Alexandre and Kyser, 2012; Alexandre et al., 2012) show that uranium mineralization can also occur away from fault zones. This is confirmed by our recent numerical modeling studies (e.g., Aghbelagh and Yang, 2014, 2015). Aghbelagh and Yang (2014), assuming methane as a reducing agent in precipitation of uraninite, showed that uraninite could precipitate away from fault zones and below the unconformity. Aghbelagh and Yang (2015) confirmed that ferrous iron, released by destruction of Fe-rich chlorite, could be an efficient reducing agent in the precipitation of uraninite. They discovered that the permeability of fault zones has a controlling role in the location of precipitated uraninite, and a uranium deposit can form in the basement either away or along fault zones, depending on the fault permeability.

In the Athabasca Basin, the dip angle and direction of faults differ from one deposit to another (Finch, 1996; Hajnal et al., 2005). For example, in the McArthur River deposit, the major fault is a northeast-trending, southeast dipping, graphite-rich reverse fault (McGill, 1999; Derome et al., 2005); whereas in the Dragon Lake area, the major fault is a left-lateral strike-slips structure (Hoeve and Sibbald, 1978), and in the Rabbit Lake deposit, the fault is a thrust-type with a low dip angle (Hoeve and Sibbald, 1978). Also, faults may become more permeable after reactivation (Lorilleux et al., 2003; Dieng et al., 2013), which is a common process in the Athabasca Basin.

The permeability of various hydrostratigraphic units in sedimentary basins is another primary factor controlling the fluid flow dynamics, and consequently the thermal regime (Hitchon, 1969a, b; Senger and Fogg, 1987; Belitz and Bredehoeft, 1988), and it can be altered through different processes. Seismic reactivation may rejuvenate the permeability periodically (Lorilleux et al., 2003; Rutqvist et al., 2013). Active deformation concurrent

with hydrothermal activity also regenerates the permeability following mineral precipitation (Lonergan and Wilkinson, 2000; Vajdova et al., 2004; Kwon et al., 2005). In addition, geochemical reactions leading to the dissolution or precipitation of minerals can decrease or increase the permeability of the medium (Kuhn et al., 2004; Lai et al., 2012; Nogues et al., 2013).

Previous numerical studies have not yet conducted systematic investigation into the effect of the above stated parameters on URU mineralization. This paper therefore aims to fill the gap, in particular addressing the role of a variety of hydrodynamic factors, including the fault dip angle, the fault dip direction and the permeability of various hydrostratigraphic units, in controlling the formation and location of uranium deposits.

Recent studies (Pascal et al., 2015; Potter and Wright, 2015; Wang et al., 2015) confirm that graphite disaggregates and depletes in proximity to the uranium mineralization (i.e., at Dufferin Lake zone and Phoenix deposit). Thus methane, produced from dissolution of graphite, could be a reductant in the formation of URU deposits. Based on these findings and previous studies (Hoeve and Sibbald, 1978; Bray et al., 1988; Kyser et al., 1989; Raffensperger and Garven, 1995b; Aghbelagh and Yang, 2014), the present work assumes a reducing condition is provided via hydrothermal alteration of graphite as follows.

Methane is first produced by the dissolution of graphite (Hoeve and Sibbald, 1978; Kyser et al., 1989; Raffensperger and Garven, 1995b) at temperatures of typical URU ore forming brines (120-200 °C):

$$C + \frac{3}{2}H_2O \leftrightarrow \frac{1}{2}H^+ + \frac{1}{2}HCO_3^- + \frac{1}{2}CH_4^0(aq). \quad (4.1)$$

Which then acts as a reductant for the reduction of uraninite:

$$UO_2^{2+} + \frac{3}{4}H_2O + \frac{1}{4}CH_4^0(aq) \leftrightarrow UO_2 + \frac{1}{4}HCO_3^- + \frac{9}{4}H^+. \quad (4.2)$$

This is a valid redox mechanism for precipitation of uraninite in the presence of graphite which is considered to be concentrated primarily along fault zones (Kotzer and Kyser, 1995; McGill, 1999; De Veslud et al., 2009).

4.2 Two-dimensional conceptual model

Although the complete cross-section of the Athabasca Basin is not available due to significant erosion, this basin is characterized by the following features: 1. Primary mineralization of URU deposits began when the fluid temperature reached about 200 °C (Kotzer and Kyser, 1995; Renac et al., 2002; Derome et al., 2005; De Veslud et al., 2009; Richard et al., 2012), depicting that the sedimentary fill must have been 6-7 km thick assuming a typical intracontinental geothermal gradient of 30 °C/km (Fridleifsson et al., 2008); 2. The bedrock consists of Archean and Paleo-Proterozoic gneisses overlain unconformably by approximately 1,500 m of flat-lying, unmetamorphosed sandstones and conglomerates of the mid-Proterozoic age; 3. The permeable sandstones and conglomerates are covered by relatively less permeable shallow marine sedimentary facies; 4. Graphite is primarily concentrated along the fault zones (Kotzer and Kyser, 1995; McGill, 1999; De Veslud et al., 2009); and 5. The faults occur predominantly in the basement rocks but often extend several meters up into the Athabasca Group (McGill, 1999; Derome et al., 2005). These faults were reactivated after filling the basin (Hoeve and Sibbald, 1978; Kotzer and Kyser, 1995), and have remained active until recent times (Hoeve and Quirt, 1984). By considering these features and based on previous studies

(Raffensperger and Garven, 1995b; Cui et al., 2012a; Aghbelagh and Yang, 2014, 2015), a sandwich-like conceptual model is developed which includes four major hydrostratigraphic units (Fig. 4.1): a vertical fault, a lower basement layer, an intermediate sandstone layer, and an upper confining layer. The fault is assumed to straddle the unconformity in the central part of the model, with a dimension of 300m by 1200m.

The model area is discretized into 80×80 quadrilateral Integral Finite Difference (IFD) elements. Various rock properties assigned for each unit (Table 2.1) are based on the data used in similar numerical modeling studies and published compilations (e.g., Freeze and Cherry, 1979; Garven and Freeze, 1984; Raffensperger and Garven, 1995a, b; Mclellan et al., 2004; Oliver et al., 2006; Cui et al., 2012a; Aghbelagh and Yang, 2014, 2015). The fault dip angle and direction, and the permeability shown in Table 2.1 for different hydrostratigraphic units will be adjusted in the following numerical case studies.

The upper boundary is assigned a fixed pore pressure of 30 MPa (assuming hydrostatic conditions based on previous studies, e.g., Cui, 2012; Cui et al., 2012a; Chi et al., 2013; Aghbelagh and Yang, 2014, 2015). The side and bottom boundaries are assumed to be impermeable to fluid flow. For heat transport, the top and bottom boundaries are assigned temperatures of 90 °C and 240 °C, respectively, corresponding to a geothermal gradient of 30 °C/km. The side boundaries are assumed to be insulated to heat transport. For aqueous component concentrations and mineral volume fractions at the top and bottom boundaries, a first-type boundary condition is assigned. That is, aqueous component concentrations and mineral volume fractions are assumed to be constant, which are the same as those of their respective units (Tables 2.2, 2.3, 2.8, 2.9).

For the side boundaries, a second-type boundary condition is employed with the normal gradient of the aqueous component concentrations and mineral volume fractions equal to zero.

For the initial conditions, a hydrostatic pressure gradient of 10 MPa/km and a thermal gradient of 30 °C/km are applied (Cui et al., 2012a; Chi et al., 2013; Aghbelagh and Yang, 2014, 2015). Initial chemical compositions for each hydrostratigraphic unit are tabulated in Tables 2.2-2.9. These tables, which summarize the aqueous compositions and volume fractions of minerals for each hydrostratigraphic unit, are based on previous mineralogical studies in the Athabasca basin (e.g., Alexandre et al., 2005) and hydrochemical modeling of URU deposits (e.g., Raffensperger and Garven, 1995b; Aghbelagh and Yang 2014, 2015). The basement unit is mainly composed of quartz, muscovite, and K-feldspar with accessory anhydrite, chlorite, hematite, pyrite, and kaolinite (Raffensperger and Garven, 1995b; Hoeve and Quirt, 1984; Fayek and Kyser, 1997; Adlakha et al., 2014). It is assumed that this unit initially has moderately reducing ($\log fO_2$ =-46.834) and acidic (pH=4.541) conditions. The fault is mainly composed of quartz, muscovite, and graphite, with accessory pyrite, kaolinite, and chlorite (Raffensperger and Garven, 1995b). This unit is assumed under more reducing ($\log fO_2$=-51.285) and slightly more acidic (pH=4.094) conditions compared to the basement unit. The sandstone unit is predominantly composed of quartz and hematite with accessory muscovite, anhydrite, chlorite, K-feldspar, and kaolinite (Tremblay, 1982; Fayek and Kyser, 1997; Hiatt et al., 2007; Alexandre et al., 2009; Adlakha et al., 2014). For this unit oxidizing, ($\log fO_2$ =-22.825) and acidic (pH=5.131) conditions are assigned. The selection of such high oxygen fugacity is based on the fact that the uranium ore-forming

fluids must have had high oxygen fugacities to transport appreciable amounts of uranium (Komninou and Sverjensky, 1996; Raffensperger and Garven, 1995b). The thermodynamic study by Komninou and Sverjensky (1996) showed that log fO_2 must have been above -24 at 200 °C to account for dissolved U(VI) (as uranyl complexes), well above the hematite-magnetite buffer (log fO2=-39.5 at 200 °C). The sandstone unit is assumed to be a uranium source by assigning an initial fluid composition of 1×10^{-4} mol/L ($\simeq$ 27 ppm) total uranium (Raffensperger and Garven, 1995b; Richard et al., 2012). The upper confining unit is a sequence of less permeable marine sandstones, siltstone, and mudstone (Ramaekers, 1990; Kotzer and Kyser, 1995). It is mainly composed of calcite, quartz, and kaolinite along with other minerals such as dolomite, muscovite, anhydrite, and hematite (Raffensperger and Garven, 1995b; Aghbelagh and Yang, 2014, 2015). In comparison with the intermediate sandstone layer, this unit is in a more oxidizing state (log fO_2 =-14.763) but with a similar acidic (pH=5.290) condition.

4.3 Numerical modeling scheme

Numerical simulations are performed using the TOUGHREACT code which is applicable to chemically-reactive nonisothermal flows of fluids in porous and fractured media (Xu et al., 2004). Physical and chemical process capabilities and solution techniques of the code have been discussed in detail by Xu and Pruess (2001) and Xu et al. (2004). The governing equations and Integral Finite Differences (IFD) space discretization method (Narasimhan and Witherspoon, 1976) are presented in Appendix 1.

Aqueous complexation, acid-base, and redox reactions proceed under the local equilibrium assumption. For dissolution and precipitation of the minerals (except for

anhydrite and calcite), a kinetic approach is adopted. The selection of the equilibrium approach for anhydrite and calcite is based on the fact that they have a typically quite rapid reaction rate (Xu et al., 2004) when they react with aqueous species. For kinetically-controlled mineral dissolution and precipitation, a general form of the rate law (Steefel and Lasaga, 1994) is used:

$$r_m = \pm k_m A_m \left|\left[\left(\frac{Q_m}{K_m}\right)^{\mu} - 1\right]\right|^{n} \quad (4.3)$$

where m is the mineral index, r_m is the dissolution/precipitation rate (positive values indicate dissolution, and negative values correspond to precipitation), A_m is the specific reactive surface area per kg of H_2O, k_m is the rate constant (moles per unit mineral surface area and per unit time) which is temperature dependent, K_m is the equilibrium constant for the mineral-water reaction written for the destruction of one mole of mineral m, Q_m is the ion activity product, the exponents μ and n are two positive numbers normally determined by experiments, and are usually, but not always, taken equal to one (as in the present work). The reaction rate constant (k_m) is considered to be a function of temperature (Lasaga, 1984; Steefel and Lasaga, 1994) using the Arrhenius equation:

$$k_m = k_{25} \exp\left[\frac{-E_a}{R}\left(\frac{1}{T} - \frac{1}{298.5}\right)\right] \quad (4.4)$$

where E_a is the activation energy, k_{25} is the rate constant at 25°C, R is the gas constant, and T is the absolute temperature. The geochemical subsystem (Appendix 2) includes 14 primary species, 46 secondary species, and 20 minerals. H^+ is used as a primary species for variation in fluid pH associated with every layer.

The thermodynamic database in the code is originally based on the equilibrium constants for aqueous species and minerals given in the EQ3/6 V7.2b database (Wolery,

1992), containing component species data, reaction stoichiometries and log (K) data entries. The EQ3/6 database is one of the most commonly used thermodynamic databases for geochemical modeling; however, it does not incorporate any uranium aqueous species and uranium minerals. In order to simulate uranium mineralization, a number of uranium aqueous species (e.g., U^{3+}, U^{4+}, UCl^{3+}, UCl_2^{2+}, $UHCO_3^{3+}$, $U(HCO_3)_2^{2+}$, UO_2^{+}, $UO_2Cl(aq)$, $UO_2Cl_2^{-}$, $UO_2HCO_3(aq)$, $UO_2(HCO_3)_2^{-}$, $UO_2(CO_3)_2^{-2}$, UO_2Cl^{+}, $UO_2Cl_2(aq)$, $UO_2CO_3(aq)$, $UO_2HCO_3^{+}$, $UO_2(HCO_3)_2(aq)$, $UO_2HSO_4^{+}$, and $UO_2SO_4(aq)$) and uranium minerals (e.g. Uraninite, Rutherfordine) are added to the existing primary thermodynamic database (EQ3/6 V7.2b database; Wolery, 1992) in TOUGHREACT. The selection of these complexes is based on previous studies on URU deposits (Kojima et al., 1994; Raffensperger and Garven, 1995b) showing that uranyl chloride (e.g. UO_2Cl^{+}, $UO_2Cl_2(aq)$), uranyl carbonate (e.g. $UO_2CO_3(aq)$, $UO_2(CO_3)_2^{-2}$), and uranyl sulfates (e.g. $UO_2SO_4(aq)$) are predominant uranium complexes in the Athabasca Basin. Refer to our recent publications (Aghbelagh and Yang, 2014, 2015) for further details of the modeling approach.

4.4 Results

4.4.1 Effect of fault dip angle and direction

Figure 4.2A shows the fluid flow and flow rate at 500,000 years around the fault zone. The high permeability of the fault zone leads to a maximum flow rate of 9.95×10^{-8} m/s (about 3.1 m/year) within it. This zone acts as a pathway for the downward migration of basinal brine into the basement, and also for the upward migration of basal fluids into the basinal sandstone so as to facilitate the interaction between the sandstone and basement

fluids. The fluid flow pattern throughout the model area at 500,000 years is depicted in the Fig. 4.2B. At the unconformity interface the flow direction is nearly horizontal, except for the intersection of this interface with the fault and for the regions where convection cells attempt to interact with the basement lithology via the downwelling and upwelling flow. Two equally-sized fluid convection cells develop within this unit, which is due to the fluid density variation as a result of the thermal gradient (Kuhn and Gessner, 2009). These cells control the transport of the aqueous species within the sandstone unit, and are responsible for leaching the uranium from the sandstone and transporting it down into the basement. The redox condition for precipitation of uraninite is provided through the interaction of uranium-bearing brines with aqueous methane in the system. The downwelling parts of the convection cells allow the basinal brines to penetrate into the basement; while the upwelling parts of the convection cells enable the basal fluids to be brought into the sandstone. This confirms the previous findings that basinal brines can penetrate into the underlying basement to some depth (Boiron et al., 2010; Richard et al., 2010; Cui et al., 2012b), and also highlights the importance of the convection cells in transferring the mass between the sandstone and underling metamorphic basement. The flow rate in the basinal sandstone is moderate (about 1.6 m/year), while in the basement it is much less (about 4.7×10^{-4} m/year) due to its very low permeability compared with that of the other units (refer to Table 2.1). The thickness and permeability of the sandstone, and the thermal gradient are determining parameters for the flow rate within the sandstone (Hanor, 1987; Evans and Nunn, 1989; Garven, 1995; Raffensperger and Garven, 1995a, b).

The temperature distribution throughout the model area at 500,000 years is also depicted in Fig. 4.2B. Fluid convection results in a temperature range of 120-150 °C within the sandstone unit. Temperature is one of the most important factors that affect the uranium mineralization (Kotzer and Kyser, 1995; Renac et al., 2002; Derome et al., 2005; De Veslud et al., 2009; Richard et al., 2012; Aghbelagh and Yang, 2014, 2015), which controls the transport and deposition of the aqueous uranium in the ore-forming fluids (Barnes, 1997).

Figure 4.2C shows the uranium mineralization at 500,000 years. Uraninite precipitates with a maximum volume fraction of 0.012 in a small area at the bottom of the fault in the basement. The high flow rate along the fault zone allows this zone to act as a structural trap, and causes the uranium mineralization therein. This volume fraction is equivalent to a uranium grade of 0.48 %, comparable with the average grade of the Rabbit Lake uranium deposit (0.45 %) (Hoeve and Sibbald, 1978; Raffensperger and Garven, 1995b), Cluff Lake OP zone (0.425 %), and West Bear uranium deposit (0.44 %) (Jefferson et al., 2007) in the Athabasca Basin.

Figure 4.2D shows the fluid flow pattern and rate at 500,000 years around the fault zone, when the fault dips 45° to the right. The flow rate along the fault is lower than that of the vertical fault scenario (compare Fig. 4.2D with Fig. 4.2A). Figure 4.2E depicts the fluid flow pattern and temperature distribution throughout the model area at 500,000 years. One major and four minor convection cells develop within the sandstone unit, with the major convection cell located in the left. Temperature within this unit ranges from 120 to150 °C, similar to that of the previous case. At 500,000 years (Fig. 4.2F), uraninite precipitates mainly away from the fault (in its footwall) and below the unconformity

interface, with a maximum volume fraction of 0.012. In addition to these major orebodies in the left of the solution domain, a minor orebody also forms beside the fault (in its hanging wall), but with a very small volume fraction (about 0.003).

Aghbelagh and Yang (2014) previously considered a fault that dips 45° to the left. The result is illustrated in Figs. 4.2G-I for comparison. It can be seen that Figs. 4.2G-I are nearly a reflection image of Figs. 4.2D-F. The subtle difference between the two cases is probably due to the difference in numerical approximations of the integral terms in the mass and energy conservation equations (refer to Xu et al., 2004). Again at 500,000 years, major uraninite (Fig. 4.2I) precipitation occurs away from the fault (also in its footwall) and below the unconformity interface, but now in the right part of the solution domain. The major uranium orebodies also have a maximum volume fraction of 0.012.

Diagenetic changes during uranium mineralization generate alteration halos associated with uranium deposits. Minerals associated with the alteration halos for some of the URU deposits in the Athabasca Basin are presented in Table 4.1, showing that the altered minerals differ from one deposit to the other. In spite of the difference, common altered minerals include muscovite, chlorite, hematite, quartz, and pyrite (Raffensperger and Garven, 1995b). The simulated alteration minerals when the fault is vertical are presented in Fig. 4.3. Muscovite (Fig. 4.3A) shows several episodes of precipitation and dissolution below the unconformity interface and around the precipitated uraninite. Dissolution of muscovite is prevalent in the cover unit and along the fault zone; precipitation mainly occurs below the unconformity interface and around the uranium deposit. Precipitation of muscovite is a consequence of k-feldspar dissociation (Fig. 4.3B) below the unconformity interface which increases the concentration of K^+,

$SiO_2(aq)$ and AlO_2^- species in the basement, and leads to precipitation of muscovite through the following reactions:

K-feldspar dissociation:

$$KAlSi_3O_8 \leftrightarrow K^+ + 3SiO_2(aq) + AlO_2^-. \quad (4.5)$$

Precipitation of muscovite:

$$K^+ + 3SiO_2(aq) + 3AlO_2^- + 2H^+ \leftrightarrow KAl_2(AlSi_3O_{10})(OH)_2. \quad (4.6)$$

Hematite (Fig. 4.3C) precipitation follows a trend more or less similar to muscovite, precipitating below the unconformity interface and around the uranium deposit. Pyrite alteration (Fig. 4.3D) mainly consists of dissolution below the unconformity interface. Dissolution of this mineral releases Fe^{2+} into solution below the unconformity, and results in precipitation of hematite as follows:

Dissolution of pyrite:

$$FeS_2 + \frac{11}{4}H_2O + \frac{7}{4}HCO_3^- \leftrightarrow Fe^{2+} + 2SO_4^{2-} + \frac{1}{4}H^+ + \frac{7}{4}CH_4. \quad (4.7)$$

Hematite precipitation:

$$2Fe^{2+} + \frac{1}{4}HCO_3^- + \frac{9}{4}H_2O \leftrightarrow Fe_2O_3 + \frac{15}{4}H^+ + \frac{1}{4}CH_4. \quad (4.8)$$

In addition to hematite, magnetite (Fig. 4.3E) also precipitates below the unconformity because of pyrite dissolution through the following reaction:

$$3Fe^{2+} + 3H_2O + \frac{1}{2}O_2(aq) \leftrightarrow Fe_3O_4 + 6H^+. \quad (4.9)$$

At 500,000 years, chlorite (Fig. 4.3F) mainly dissolves below the unconformity interface. It is observed from Figs. 4.3A and 4.3F that the alteration zones associated with the

uranium deposit are similar to those of the basement-hosted Millennium deposit in the Athabasca Basin, consisting of muscovite rather than the chlorite and muscovite (Cloutier et al., 2009). Kaolinite (Fig. 4.3G) precipitates along the unconformity and within the fault zone, forming an alteration halo around the precipitated uraninite as a result of water-rock interaction. Graphite (Fig. 4.3H) dissolution, which occurs along the fault zone, releases aqueous methane into solution (refer to reactions 4.1 and 4.2). It should be noted that albite and anorthite do not precipitate in the modeled area, which is in agreement with the field observations in the Athabasca Basin (Cloutier 2015, personal communication).

Figure 4.4 shows the alteration minerals at 500,000 years for the case when the fault dips 45° to the right. Muscovite (Fig. 4.4A) precipitation is pervasive in the basement and surrounding the uranium deposit, as a result of K-feldspar dissociation (Fig. 4.4B) below the unconformity interface. Hematite (Fig. 4.4C) precipitates below the unconformity on both sides of the fault zone, which is due to the dissolution of pyrite (Fig. 4.4D). In addition to the hematite, some magnetite is also formed below the unconformity as a consequence of pyrite dissolution. Chlorite (Fig. 4.4F) is mainly subject to dissolution below the unconformity. Kaolinite (Fig. 4.4G) predominantly precipitates in the cover unit and on the unconformity interface, and graphite (Fig. 4.4H) dissolves along the fault zone. When the fault dips 45° to the left, the simulated alteration minerals have a pattern (not shown) as a reflection image of Fig. 4.4.

It should be pointed out that regardless of the fault dip angle and direction, dissolution of the graphite produces aqueous methane (Figs. 4.5A, 4.5E and 4.5I) that reduces the oxidized uranium (Figs. 4.5B, 4.5F and 4.5J) in the solution and leads to the

precipitation of uraninite (Figs. 4.2C, 4.2F and 4.2I). In addition, the uranium-bearing brines also have physicochemical conditions that are in favor of the formation of URU deposits, including a pH range of about 4-4.5 (Figs. 4.5C, 4.5G and 4.5K), a temperature of about 160-180 °C (Figs. 4.2B, 4.2E, and 4.2H), and a reduction of the oxygen fugacity (Figs. 4.5D, 4.5H, and 4.5L), as confirmed in our previous studies (Aghbelagh and Yang, 2014, 2015).

4.4.2 Effect of the permeability of the hydrostratigraphic units

Here we only consider the case when the fault dips 45° to the left. Figure 4.6A shows the fluid flow pattern and flow rate around the fault zone at 500,000 years when the fault permeability is reduced one order in magnitude (from 1×10^{-12} m^2 to 1×10^{-13} m^2). Following this permeability reduction, the flow rate drops substantially from 5.53×10^{-8} m/s (1.7 m/year) (refer to Fig. 4.2G) to 4.31×10^{-19} m/s (1.4×10^{-11} m/year). Fig. 4.6B illustrates the fluid flow and temperature distribution throughout the model area. The maximum flow rate (1.37 m/year) now occurs within the sandstone unit rather than in the fault zone. This is because the fault is now less permeable than the sandstone unit. One major and three minor convection cells develop within the sandstone unit, with the major cell localized in the right. In comparison with the case when the fault permeability is equal to 1×10^{-12} m^2, the major convection cell is shifted to the edge of the solution domain (compare Fig. 4.6B with Fig. 4.2H). The temperature distribution (Fig. 4.6B) is modified as well, following the change in flow pattern. At 500,000 years, uraninite (Fig. 4.6C) precipitates below the unconformity interface and away from the fault zone. In accordance with the major convection cell shift, uraninite now precipitates closer to the

right edge as well. The maximum volume fraction of precipitated uraninite (0.003) is less than that of the case with the fault permeability of 1×10^{-12} m^2, which is likely due to the lower flow rate along the fault zone and the resultant weaken interaction of the oxidized basinal brines with the basement lithology. Further reduction of the fault permeability to 1×10^{-14} m^2 leads to a very small flow rate (2.3×10^{-11} m/year) along this zone (Fig. 4.6E), that now serves as a barrier for mass transport between the sandstone and basement. One major and five minor convection cells develop within the sandstone, with the major cell positioned immediately above the fault zone. The maximum flow rate is 1.1 m/year, again occurring in the sandstone unit but less than that of the previous case. The temperature distribution within this unit (Fig. 4.6F) is modified, following the further reduction of flow rate. No uraninite (Fig. 4.6G) precipitates in the model area. This is mainly due to the fact that the less permeable fault zone prevents mass transport from the basinal sandstone into the basement, and the basinal brines mainly interact with the basement via the convection cells but at a much lower flow rate (1.1 m/year) than that in the previous case. It should be noted that oxygen fugacity (Fig. 4.6H) shows no reduction below and around the unconformity interface. Moreover, no graphite is dissolved along the fault zone, implying that no methane is provided to reduce the oxidized uranium in the solution. This is also another reason why no uraninite precipitates in the model area.

Aghbelagh and Yang (2015), with consideration of ferrous iron as a reducing agent, conducted a sensitivity analysis to investigate the role of the fault permeability in the precipitation of uraninite. Their results showed that enhancing the fault permeability leads to a higher flow rate along the fault and the development of two equally-sized convection cells within the sandstone. In the present work a similar study is implemented

by assigning higher permeabilities (10^{-11} m^2 and 10^{-10} m^2) to the fault zone, but considering methane as a reductant. Our results show that the flow rates along the fault zone are increased to 2.2×10^{-7} m/s (about 7 m/year) and 7.3×10^{-7} m/s (23 m/year), respectively (Figs. 4.6I and 4.6M), and two symmetric convection cells develop within the sandstone (Figs. 4.6J and 4.6N). Uranium mineralization occurs along the fault in the basement (Figs. 4.6K and 4.6O). The simulation results are similar to those of Aghbelagh and Yang (2015), implying that location of the precipitated uraninite is not a function of the reducing agent, but is controlled by the hydraulic properties of the fault zone. It should be noted that when the fault permeability is equal to 10^{-10} m^2, the volume fraction of the precipitated uraninite (Fig. 4.6O) is slightly higher than that when the permeability is equal to 10^{-11} m^2 (Fig. 4.6K). It is also observed from Figs. 4.6D, 4.6L, and 4.6P that uraninite precipitates in the areas experiencing a reduction of the oxygen fugacity.

The sandstone unit, as a prime medium accommodating basinal fluid circulation that leaches uranium, plays an important role in the formation of URU deposits. One order reduction of its permeability (from 3×10^{-13} m^2 to 3×10^{-14} m^2), while other properties remain the same, leads to no deposition of uranium in the solution domain. Only a single convection cell (Fig. 4.7A) develops, and the temperature distribution (Fig. 4.7A) is modified accordingly..The less permeable sandstone leads to a low flow rate (about 9.5×10^{-4} m/year), thus the basinal brines (including aqueous oxidized uranium) cannot easily flow within this unit and thus cannot penetrate downwards to interact with the basement lithology. As a result, the aqueous uranium oxide cannot be efficiently delivered to proper sites for precipitation of uraninite. Additionally, oxygen fugacity (Fig. 4.7C) is also not reduced in the solution domain. Consequently, no uraninite precipitates

in the model area. Similarly, with two orders of reduction in permeability of the sandstone unit (from 3×10^{-13} m^2 to 3×10^{-15} m^2) a single convection cell (Fig. 4.7B) develops and the flow rate becomes even smaller (4.7×10^{-4} m/year). Since the permeability of the sandstone unit is now close to that of the cover (1×10^{-15} m^2), the convection cell extends to the cover unit. The temperature distribution (Fig. 4.7B) is similar to that in the previous case, and once again no uraninite precipitates in the modeled area.

One order of magnitude increase in permeability of the sandstone (from 3×10^{-13} m^2 to 3×10^{-12} m^2) leads to the development of one major and three minor convection cells (Fig. 4.7D). These cells are confined in the sandstone unit, and the strongest flow occurs within the sandstone rather than in the fault zone (with a maximum rate of 7.2 m/year) since the sandstone is now more permeable. Thermally-induced convective flow results in a temperature (Fig. 4.7D) range of 120-150 °C within the sandstone. Similar to the case when the sandstone permeability is 3×10^{-13} m^2, the downwelling and upwelling parts of the convection cells contribute to the interaction of the basinal sandstone and basement fluids, in addition to the mass transport along the fault zone (compare Fig. 4.7D with Fig. 4.2H). Uraninite (Fig. 4.7E) precipitates away from the fault zone and below the unconformity interface where the dominant downwelling flow interacts with the basement lithology. Also, it is observed from Fig. 4.7F that oxygen fugacity is reduced in that area. It should be pointed out, however, that the volume fraction of the precipitated uraninite (maximum 0.0008) is now very small compared with that when the sandstone permeability is 3×10^{-13} m^2 (compare Fig. 4.7E with Fig. 4.2I). This volume fraction is equivalent to a uranium ore grade of 0.03 %, which is much lower than the world average

uranium grade (0.2 %) (Aben Resources Ltd) and is not economical. Further increasing the permeability from 3×10^{-13} m^2 to 3×10^{-11} m^2 leads to the development of two convection cells within the sandstone unit (Fig. 4.7G). The flow rate (maximum 15 m/year) is even higher than that of the previous case. No uraninite precipitates near the unconformity interface. Uranium mineralization occurs mainly on the boundary between the cover and the sandstone units (Fig. 4.7H) with a negligible volume fraction (maximum 2.00×10^{-6}), which is due to the reduction of oxygen fugacity in that boundary (Fig. 4.7I). The flow rate within the sandstone unit is now so high that the circulating flow in the vicinity of the unconformity interface is almost parallel to this interface, reducing the penetration of basinal brines into the basement. This may explain why no uraninite precipitates near the unconformity interface.

The permeability of the metamorphic basement also has an important role in the formation of URU deposits since it influences the interplay between the basal fluids and the basinal brines. Figure 4.8A presents the flow pattern at 500,000 years when the permeability of the basement is decreased one order in magnitude (from 3×10^{-16} m^2 to 3×10^{-17} m^2), while other parameters remain unchanged. Two major and two minor convection cells now develop within the sandstone, and the flow rate in the basement is reduced. These cells are positioned symmetrically within the sandstone unit. No uraninite precipitates close to the unconformity interface, except for a negligible volume fraction (maximum 2.03×10^{-6}) along the sandstone-cover interface (Fig. 4.8B) where the oxygen fugacity (Fig. 4.8C) is reduced. With two orders of magnitude reduction in its permeability (from 3×10^{-16} m^2 to 3×10^{-18} m^2), three convection cells develop in the sandstone (Fig. 4.8D). Once again no significant uranium mineralization occurs (Fig.

4.8E), and oxygen fugacity distribution has a pattern (Fig. 4.8F) similar to that shown in Fig. 4.8C.

For the case when the permeability of the basement is increased one order of magnitude (from 3×10^{-16} m^2 to 3×10^{-15} m^2), the fluid flow and temperature distribution at 500,000 years are presented in Fig. 4.9A. Following this permeability enhancement, the basal fluids also circulate in the basement. This is in agreement with previous studies (e.g., Kuhn et al., 2004; Kuhn and Gessner, 2006) that thermally-driven free convection may occur in the low permeable strata, in addition to the convective flow within the basinal sandstone. Two equally-sized convection cells now develop in the sandstone and basement units. Temperature is greatly affected by the horizontal and vertical flow in the basement. Uranium mineralization occurs along the sandstone-cover boundary (Fig. 4.9B), but with a negligible volume fraction (maximum 1.89×10^{-6}), in which ore-forming fluids experience a reduction in oxygen fugacity (Fig. 4.9C). Further increasing the basement permeability to 3×10^{-14} m^2 leads to a more or less similar fluid flow pattern, temperature distribution, oxygen fugacity regime, and uranium mineralization pattern (Figs. 4.9D-F).

It should be noted that the less permeable basement unit does not allow the basinal brines to easily interact with it. In other words, the aqueous uranium (UO_2^{2+}) assigned to the sandstone (1.0×10^{-4} mol/L) hardly flows into the basement via the convection cells or along the fault (Figs. 4.10A and 4.10C). This results in an extremely low concentration for aqueous uranium in the basement (about 8.9×10^{-40} mol/L) which is not sufficient for precipitation of uraninite (compare Figs. 4.10A and 4.10C with Fig. 4.5J). Similarly, no methane (Figs. 4.10B and 4.10D) can easily move within the basement, and the

concentration of this species remains almost unchanged. The low concentration of aqueous uranium in the basement explains why no uranium precipitates in the vicinity of the unconformity. On the other hand, the more permeable basement allows ore-forming brines to circulate in both the sandstone and the basement (refer to Figs. 4.9A and 4.9D). This makes the aqueous uranium (Figs. 4.10E and 4.10G) and methane (Figs. 4.10F and 4.10H) evenly distributed within these units. The concentration of aqueous uranium (3.25×10^{-5}) is high enough, but the concentration of methane (0.575 mol/L) is not sufficient for precipitation of uraninite (Compare Figs. 4.10F and 4.10H with 4.5I). This may explain why no uranium deposit can be formed when the basement is more permeable.

4.5. Discussion

The numerical results show that the fault dip angle and direction control the basinal fluid convection and temperature distribution within the sandstone unit, which in turn determines the location of precipitated uraninite. When the fault is vertical, uraninite always precipitates at the bottom of the fault zone (Fig. 4.2C); when the fault is inclined, uraninite precipitates below the unconformity interface either away from or along the fault zone, dependent upon the fault permeability. Regardless of the reducing agent, hydraulically more permeable fault zones tend to lead to precipitation of uraninite in the basement along the fault zones, while less permeable faults induce uraninite precipitation away from the fault zones and in the footwall (refer to Figs. 4.2I, 4.6C, 4.6K, and 4.6O). Exploration companies currently take advantage of fault zones as an indicator of URU deposits. This research suggests that the structural and hydraulic analysis of fault zones

(i.e. determining their dip angle, dip direction, and hydraulic properties) would also be beneficial in localizing the orebodies.

Uraninite tends to precipitate (refer to Figs. 4.2B-C, 4.2E-F, and 4.2H-I) in the locales where dominant downwelling basinal brines interact with the basement lithology. This study along with the previous studies (e.g., Wilde et al., 1985, 1989a; Walshe, 1986; Kotzer and Kyser, 1995; Komninou and Sverjensky, 1996; Kojima et al., 1994; Cuney, 2009; Richard et al., 2010, 2012; Aghbelagh and Yang, 2014, 2015) also confirms that these locales have physicochemical conditions that are in favor of uranium mineralization, including a pH of 4-4.5 (Figs. 4.5C, 4.5G, and 4.5K), a temperature of about 160-180 °C (Figs. 4.2B, 4.2E, and 4.2H), and a reduction of the oxygen fugacity (Figs. 4.5D, 4.5H, and 4.5L). These parameters collectively determine whether the metals are deposited to form ore, or remain in the fluids to be transported elsewhere (Peiffert et al., 1994, 1996; Bali, 2012).

The permeability of different hydrostratigraphic units also plays an important role in uranium ore mineralization. When the sandstone unit is less permeable, a single convection cell (refer to Figs. 4.7A and 4.7B) develops and spreads to the cover unit. However, no uranium mineralization occurs in the solution domain. This is likely due to the very low flow rate within the sandstone that is unfavorable for mass transport between the sandstone and basement. When the sandstone permeability is increased to 3×10^{-12} m^2, four convection cells (refer to Fig. 4.7D) develop within the sandstone unit, but the precipitated uraninite has a very small volume fraction (not economic) and is located away from the fault zone below the unconformity interface (Fig. 4.7E). Further increasing the sandstone permeability to 3×10^{-11} m^2 leads to a higher flow rate and the

development of two convection cells within the basinal sandstone (Fig. 4.7G). Again, no economic URU deposit is formed in the basement, and uranium mineralization occurs mainly along the sandstone-cover interface (Fig. 4.7H) with a negligible volume fraction.

Reducing the permeability of the basement also modifies the fluid flow and temperature distribution (Figs. 4.8A and 4.8D). No uranium mineralization occurs around the unconformity when the basement permeability is reduced. Uraninite precipitation tends to occur along the sandstone-cover, but has no economic value (Figs. 4.8B and 4.8E). Increasing the permeability of the basement leads to fluid circulation in both the basement and the sandstone unit (Figs. 4.9A and 4.9D). Once again, however, uraninite precipitates only in the cover unit with a negligible volume fraction (Figs. 4.9B and 4.9E).

For the cases leading to uranium mineralization along the sandstone-cover interface, the grade of the precipitated uraninite is much less than that of the cases leading to the formation of URU deposits in the basement (compare Fig. 4.8B with Fig. 4.2I). This is mainly due to the fact that the reduction of oxygen fugacity along the sandstone-cover boundary is several orders less than that in other cases (compare Fig. 4.8C with Fig. 4.5L). Additionally, the temperature along the sandstone-cover interface is less than that in the basement. Therefore physicochemical parameters not only control the location of the precipitated uraninite, but also affect the grade of orebodies.

Although the Athabasca and Thelon Basins have a similar sedimentology and evolutionary record (Miller, 1995; Renac et al., 2002), the size and grade of precipitated uraninite are different in these basins. The Athabasca Basin accommodates the world's highest grade URU deposits such as at McArthur River and Cigar Lake with an average

grade of 22.28 % and 15.4 %, respectively (Jefferson et al., 2007). This basin also hosts some lower grade URU deposits such as McClean Lake (with an average ore grade of 2.78 %), Millennium deposit (2.304 %), and Rabbit Lake mine (0.27 %) (Jefferson et al., 2007). In contrast, the Thelon Basin seems to host lower grade URU deposits (Renac et al., 2002) with the Boomerang Lake prospect (0.5 %) and the Kiggavik deposit (0.4 %) at the eastern and western margin, respectively (Jefferson et al., 2007). Our numerical results indicate that the variation in size and grade of the uranium deposits in these two basins may be due to the difference in fluid flow patterns and physicochemical conditions, which likely result from the change in structural features and hydraulic properties of the stratigraphic units involved.

4. 6. Conclusion

Flow and reactive transport modeling has been conducted to address the role of hydrodynamic factors in controlling the formation and location of URU deposits. The simulation results show that the fault dip angle and direction, and the permeability of the stratigraphic units control the fluid flow pattern and rate in the fault, the basinal sandstone and the basement. This in turn influences the mass and energy exchange between the sandstone and the basement, and consequently the location of precipitated uraninite. For a vertical fault, uranium mineralization occurs at its bottom in the basement; whereas for a dipping fault, uranium mineralization occurs either away from or along the fault zone, depending on the fault permeability. A more permeable, dipping fault tends to lead to uranium mineralization along this zone, while a less permeable fault

likely results in the precipitation of uraninite away from it. A sandstone unit with either a very low or a very high permeability seems to be unfavorable for the formation of an economic URU deposit, and so does a basement unit with such a hydraulic condition, which suggests that both the sandstone and the basement seem to have an optimal window of permeability (~ 3×10^{-13} m^2 for the sandstone, and ~ 3×10^{-16} m^2 for the basement) in order for an economic deposit to be formed. This study also reveals that the variation in size and grade of URU deposits in sedimentary basins is likely due to the difference in fluid flow patterns and physicochemical conditions caused by the change in structural features and hydraulic properties of the stratigraphic units involved. From an exploration point of view, this research highlights the importance of the fault dip angle and direction, and the permeability of various hydrostratigraphic units in determining the location of the uranium orebodies.

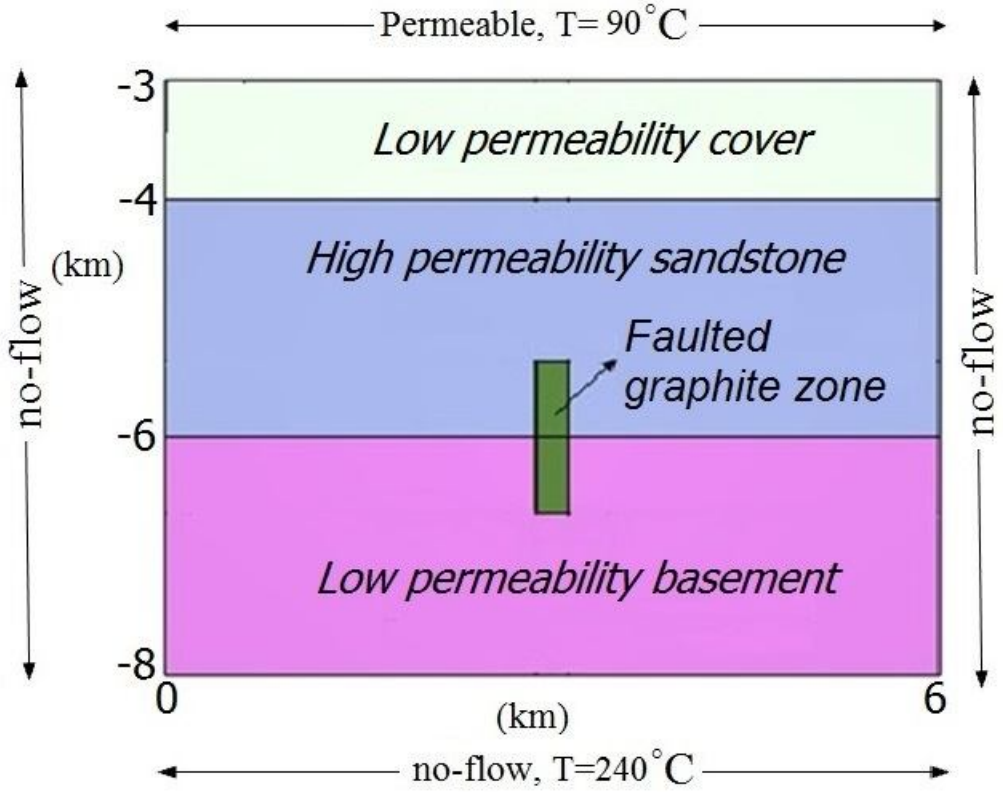

Fig. 4.1. Conceptual model used in the simulation of URU deposits (based on previous studies by Cui et al., 2012a and Aghbelagh and Yang, 2014, 2015).

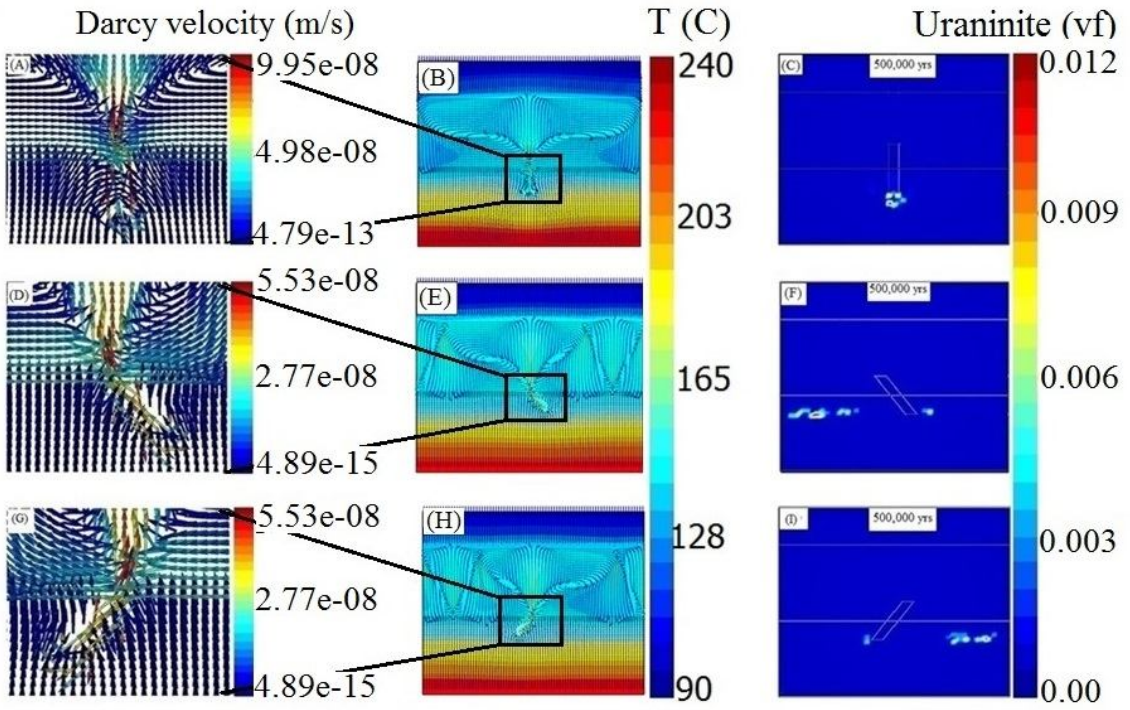

Fig. 4.2. Fluid flow regime around the fault, fluid flow pattern and temperature distribution, and precipitated uraninite throughout the model area at 500,000 years. (A-C) when the fault is vertical, (D-F) when the fault dips 45° to the right, and (G-I) when the fault dips 45° to the left.

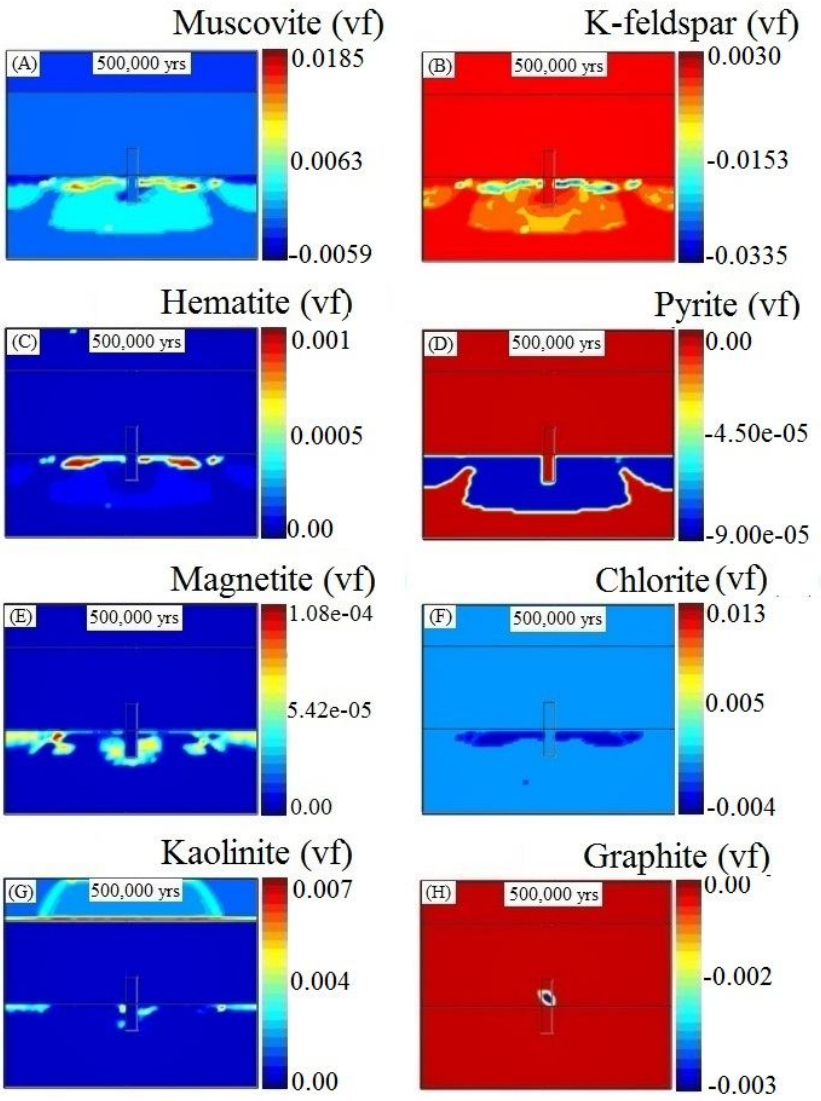

Fig. 4.3. Alteration minerals when the fault is vertical at 500,000 years. (A) muscovite, (B) k-feldspar, (C) hematite, (D) pyrite, (E) magnetite, (F) chlorite, (G) kaolinite, and (H) graphite alterations. Positive values for the volume fraction refer to precipitation of the mineral and negative values refer to dissolution of the mineral.

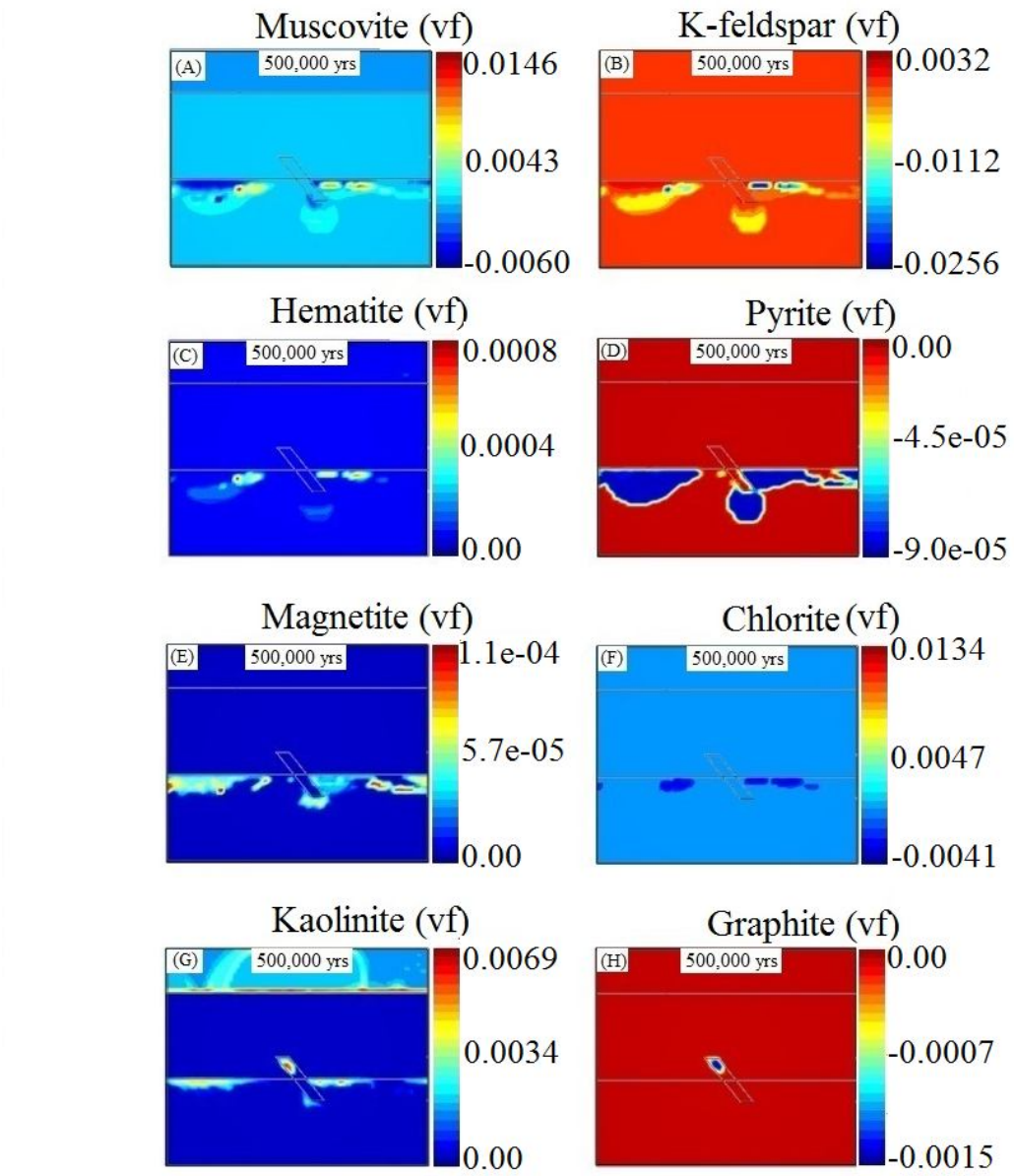

Fig. 4.4. Alteration minerals when the fault dips 45° to the right at 500,000 years. (A) muscovite, (B) k-feldspar, (C) hematite, (D) pyrite, (E) magnetite, (F) chlorite, (G) kaolinite, and (H) graphite alterations. Positive values for the volume fraction refer to precipitation of the mineral and negative values refer to dissolution of the mineral.

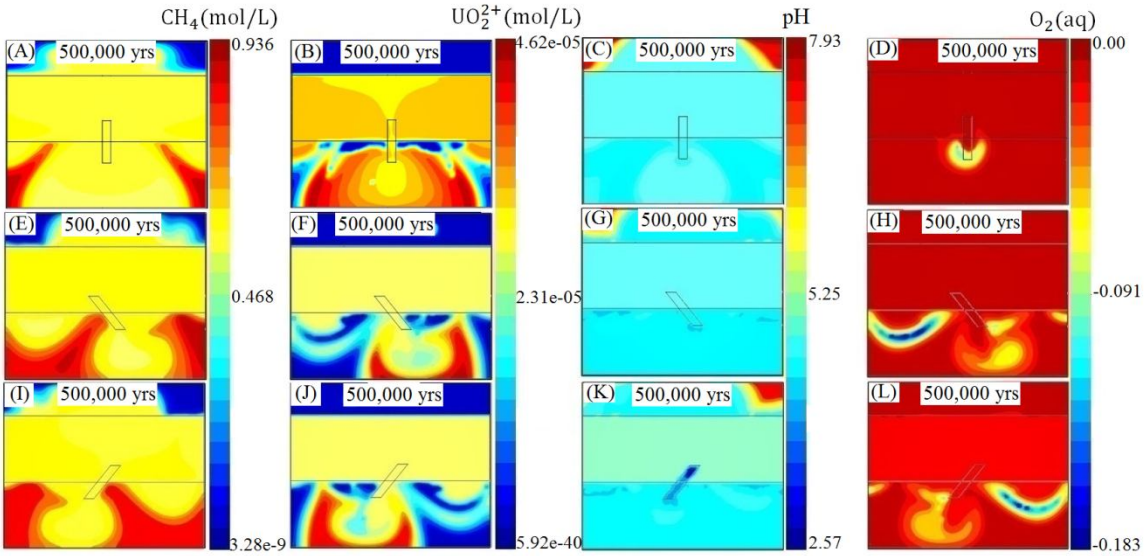

Fig. 4.5. Concentration of $CH_4(aq)$, UO_2^{2+}, pH regime, and variation of oxygen fugacity at 500,000 years. (A-D) when the fault is vertical, (E-H) when the fault dips 45° to the right, and (I-L) when the fault dips 45° to the left.

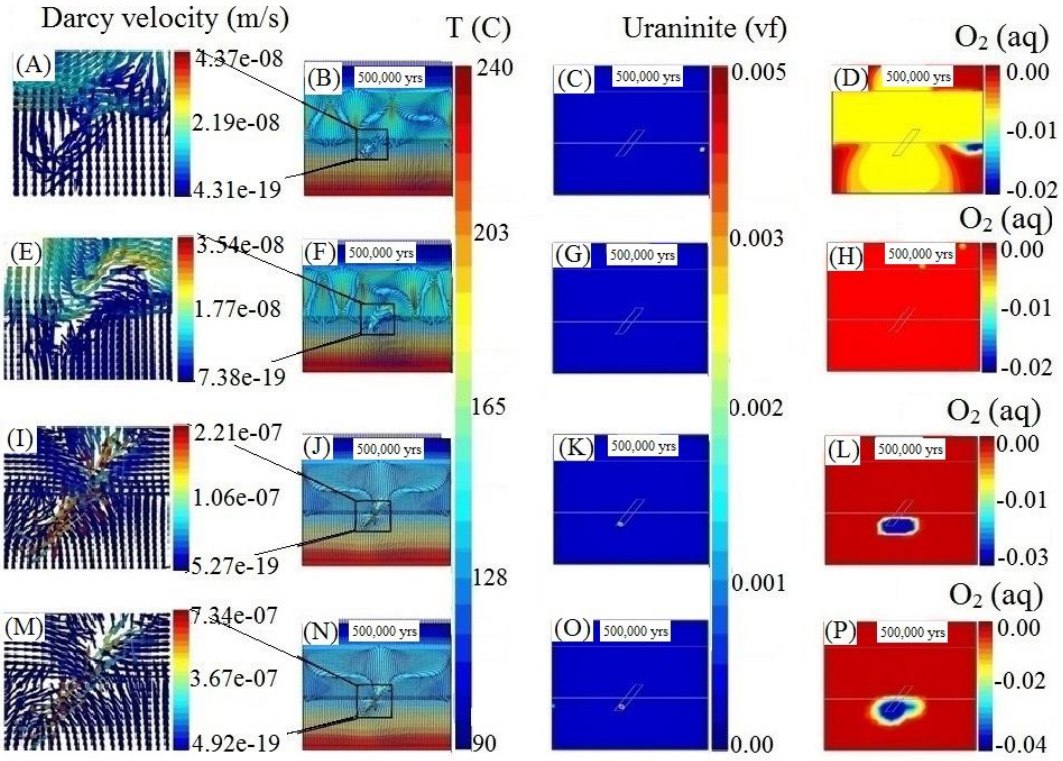

Fig. 4.6. Fluid flow pattern and rate around the fault, fluid flow pattern and temperature distribution, precipitated uraninite, and variation of oxygen fugacity throughout the model area at 500,000 years. (A) subject to a permeability of 10^{-13} m^2 for the fault, (B) subject to a permeability of 10^{-14} m^2 for the fault, (C) subject to a permeability of 10^{-11} m^2 for the fault, (D) subject to a permeability of 10^{-10} m^2 for the fault.

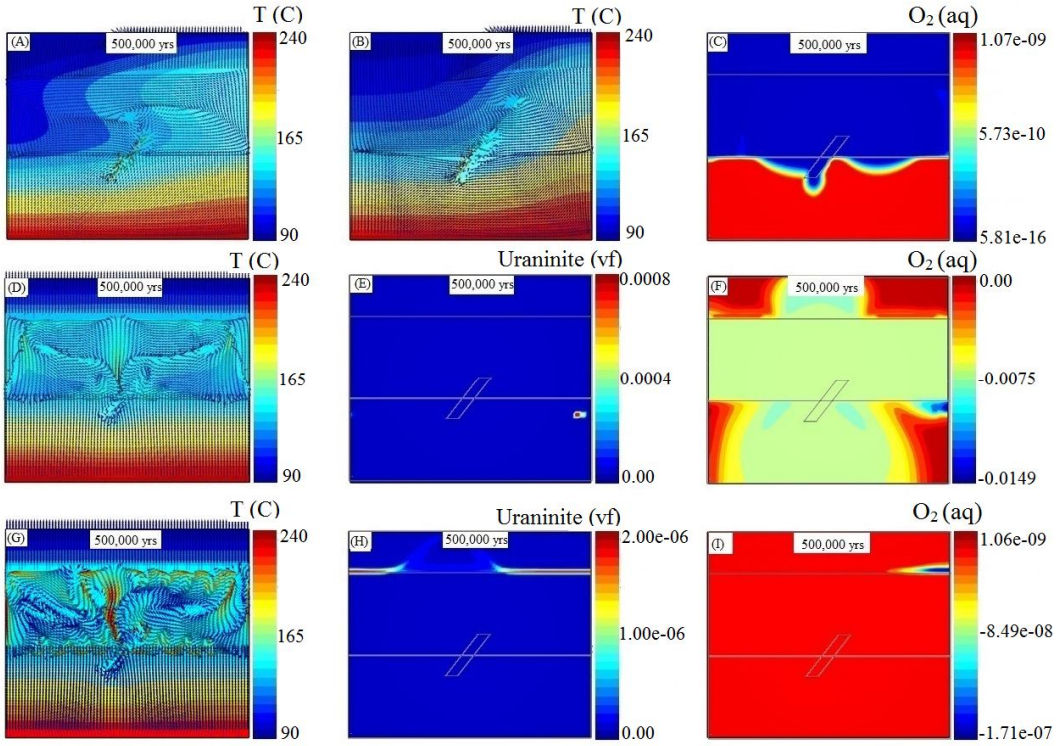

Fig. 4.7. Fluid flow pattern and temperature distribution, precipitated uraninite, and variation of oxygen fugacity regime at 500,000 years. (A and C) subject to a permeability of 3×10^{-14} m^2 for the sandstone, (B) subject to a permeability of 3×10^{-15} m^2 for the sandstone, (D-F) subject to a permeability of 3×10^{-12} m^2 for the sandstone, (G-I) subject to a permeability of 3×10^{-11} m^2 for the sandstone.

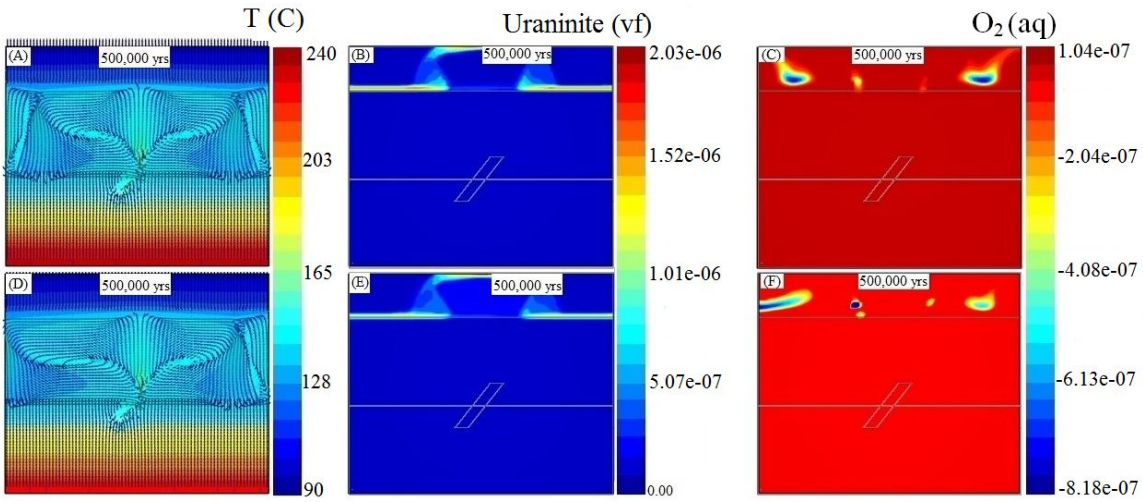

Fig. 4.8. Fluid flow pattern and temperature distribution, precipitated uraninite, and variation of oxygen fugacity regime at 500,000 years. (A-C) subject to a permeability of 3×10^{-17} m^2 for the basement, (D-F) subject to a permeability of 3×10^{-18} m^2 for the basement.

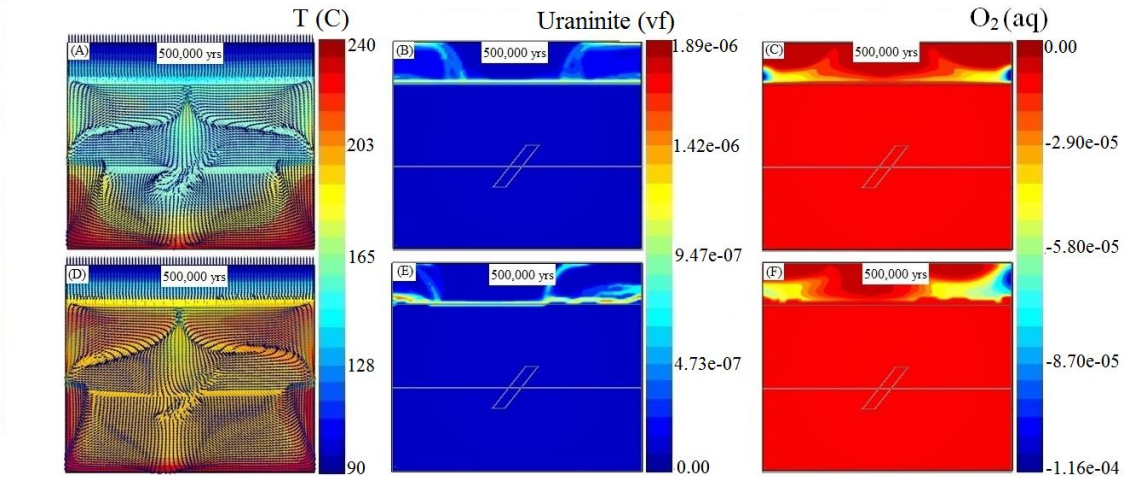

Fig. 4.9. Fluid flow pattern and temperature distribution, precipitated uraninite, and oxygen fugacity regime at 500,000 years. (A-C) subject to a permeability of 3×10^{-15} m^2 for the basement, (D-F) subject to a permeability of 3×10^{-14} m^2 for the basement.

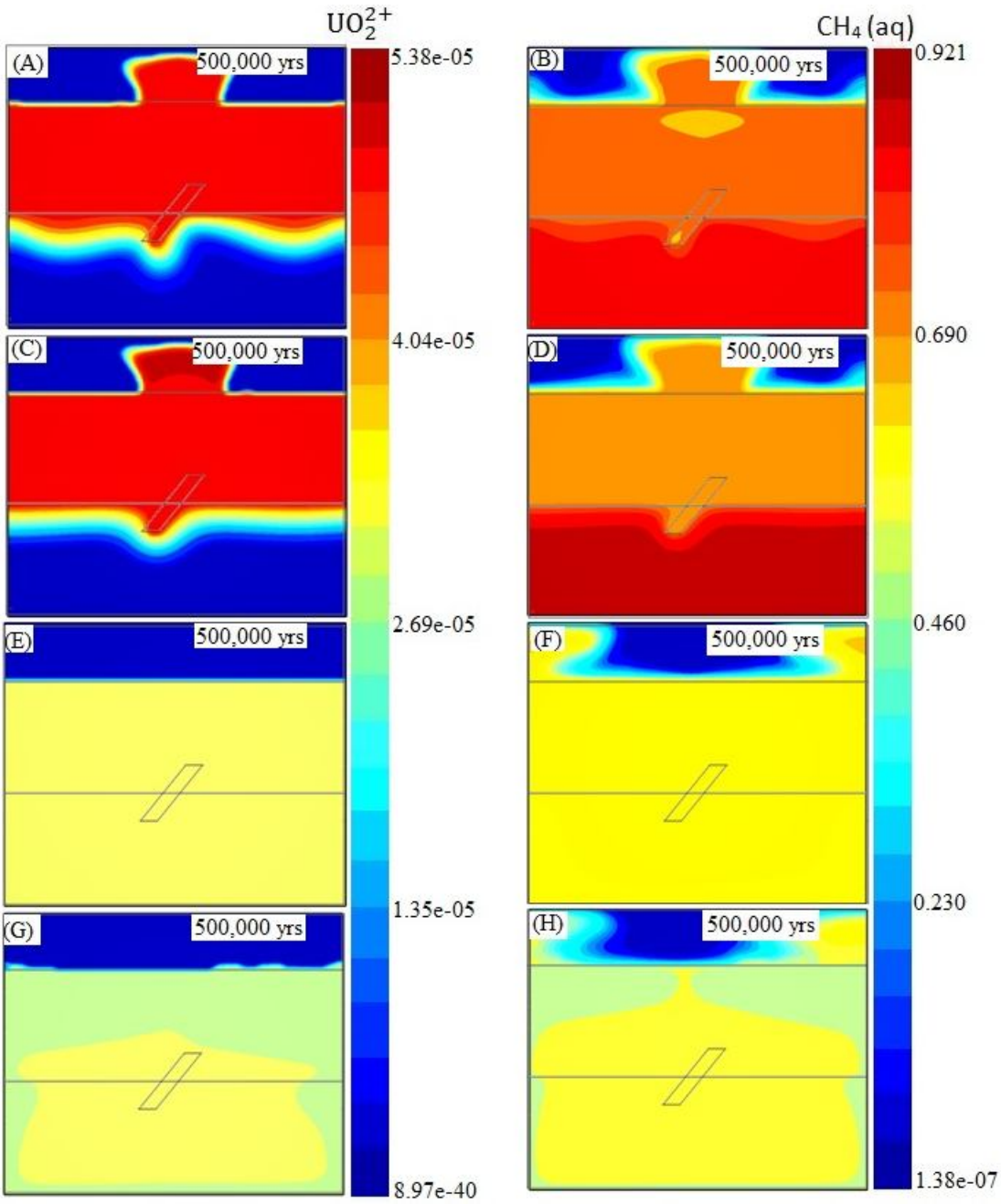

Fig. 4.10. Concentration of UO_2^{2+} and CH_4 (aq) at 500,000 years. (A-B) subject to a permeability of 3×10^{-17} m^2 for the basement, (C-D) subject to a permeability of 3×10^{-18} m^2 for the basement, (E-F) subject to a permeability of 3×10^{-15} m^2 for the basement, (G-H) subject to a permeability of 3×10^{-14} m^2 for the basement.

Table 4.1. Altered minerals associated with URU deposits in the Athabasca Basin.

Deposit	Alteration minerals
Cigar Lake	Illite, chlorite, hematite (Brunrton et al., 1987)
Key Lake	Kaolinite, chlorite, quartz, siderite, calcite (Dahlkampt, 1974)
Midwest Lake	Chlorite, sericite, muscovite (Ayres et al., 1983)
Collins Bay	Illite, chlorite, hematite (Tremblay, 1982)
Rabbit Lake	Chlorite, dolomite, quartz, tourmaline (Hoeve and Sibbald, 1978; Alexandre et al., 2005)
Dawn Lake	Illite, chlorite, hematite (Tremblay, 1982; Quirt, 1977)
McClean Lake	Illite, chlorite, hematite (Bray et al., 1987)
McArthur River (sandstone part)	Quartz, kaolinite, chlorite, dravite (McGill et al., 1993)
McArthur River (basement part)	Illite, chlorite, and dravite, with local apatite and carbonate (McGill et al., 1993)

References

Aben Resources Ltd, d. www.abenresources.com/s/uranium.asp.

Adlakha, E.E., Hattori, K., Zaluksi, G., Kotzer, T., and Potter, E.G., 2014, Alteration within the basement rocks associated with the P2 fault and the McArthur River uranium deposit, Athabasca Basin: Geological Survey of Canada, Open File 7462. doi: 10.4095/293364.

Aghbelagh, Y.B., and Yang, J., 2014, Effect of graphite zone in the formation of unconformity-related uranium deposits: Insights from reactive mass transport modeling: Journal of Geochemical Exploration, v. 144, p. 12-27.

Aghbelagh, Y.B., and Yang, J., 2015, Evaluation of Fe-rich chlorite as a reducing agent in the formation of unconformity-related uranium deposits: Insights from reactive flow modeling: Mineralium Deposita, Submitted and under review.

Alexandre, P., and Kyser, K., 2012, Reductants involved in the formation of the Athabasca Basin unconformity-related uranium deposits: Joint annual meeting of the Geological Association of Canada-Mineralogical Association of Canada, Abstracts, v. 35, p. 2.

Alexandre, P., Kyser, K., Jiricka, D., and Witt, G., 2012, Formation and evolution of the Centennial unconformity-related uranium deposit in the South-Central Athabasca Basin, Canada: Economic Geology, v. 107, p. 385-400.

Alexandre, P., Kyser, K., Thomas, D., Polito, P., and Marlat, J., 2009, Geochronology of unconformity-related uranium deposits in the Athabasca Basin, Saskatchewan, Canada and their integration in the evolution of the basin: Mineralium Deposita, v. 44, p. 41-59.

Alexandre, P., Kyser, K., and Polito, P., 2005, Alteration mineralogy and stable isotope geochemistry of paleoproterozoic basement hosted unconformity-type uranium deposits in the Athabasca basin, Canada: Economic Geology, v. 100, p. 1547-1563.

Ayres, D.E., Wray, E.M., Farstad, J., Ibrahim, H., 1983, Geology of the Midwest uranium deposit, *in* Cameron EM, editor, Uranium Exploration in Athabasca Basin, Saskatchewan: Geological survey of Canada, Paper 82-11, p. 33-40.

Bali, E., 2012, Uranium-ore giants: Nature Geoscience, v. 5, p. 96-97.

Barnes, H.L., 1997, Geochemistry of Hydrothermal Ore Deposits, Volume 1: John Wiley & Sons.

Belitz, K., and Bredehoeft, J.D., 1988, Hydrodynamics of Denver Basin: explanation of subnormal fluid pressures: American Association of Petroleum Geologists Bulletin, v. 72, p. 1334-1359.

Boiron, M.C., Cathelineau, M., and Richard, A., 2010, Fluid flows and metal deposition near basement/cover unconformity: Lessons and analogies from Pb_Zn_F_Ba systems for the understanding of Proterozoic U deposits: Geofluids, v. 10, p. 270-292.

Bray, C.J., Spooner, E.T.C., Hall, C.M., York, D., Bills, T.M., Krueger, H.W., 1987. Laser probe $^{40}Ar/^{39}Ar$ and conventional K/Ar dating of illites associated with the McClean unconformity-related uranium deposits, northern Saskatchewan, Canada: Canadian Journal of Earth Sciences 24, p. 10-23.

Bray, C.J., Spooner, E.T.C., and Longstaffe, F.J., 1988, Unconformity-related uranium mineralization, McClean deposits, north Saskatchewan, Canada: hydrogen and oxygen isotope geochemistry: Canadian Mineralogist, v. 26, p. 249-268.

Bruneton, P. 1987, Geology of the Cigar Lake uranium deposit (Saskatchewan, Canada), in Gliboy CF, Vigrass LW, editors, Economic Minerals of Saskatchewan: Saskatchewan Geological Society Special publication, v. 8, p. 99-119.

Chi G, Bosman S, and Card C. 2011, Fluid flow models related to uranium mineralization in the Athabasca basin: A review and new insights: Saskatchewan Geological Survey Open House, Abstract, v. 4.

Chi, G., Bosman, S., and Card, C., 2013, Numerical modeling of fluid pressure regime in the Athabasca Basin and implications for fluid flow models related to the unconformity type uranium mineralization: Journal of Geochemical exploration, v. 125, p. 8-19.

Chi, G., and Xue, C. 2014, Hydrodynamic regime as major control on localization of uranium mineralization in sedimentary basins: Science China –-Earth Sciences, v. 57, p. 2928-2933.

Cloutier, J., Kyser, K., Olivo, G.R., Alexandre, P., and Halaburda, J., 2009, The Millennium uranium deposit, Athabasca Basin, Saskatchewan, Canada: An atypical basement-hosted unconformity-related uranium deposit: Economic Geology, v. 104, p. 815-840.

Cui, T., 2012, The formation mechanisms of unconformity-related uranium deposits: numerical modeling concerning the Thelon Basin: Unpublished PhD thesis, Windsor, Canada.

Cui, T., Yang, J., and Samson, I.M., 2010, Numerical modeling of hydrothermal fluid flow in the Paleoproterozoic Thelon Basin, Nunavut, Canada: Journal of Geochemical Exploration, v. 106, p. 69-76.

Cui, T., Yang, J., and Samson, I.M., 2012a, Tectonic deformation and fluid flow: Implications for the formation of unconformity-related uranium deposits: Economic Geology, v. 107, p. 147-163.

Cui, T., Yang, J., and Samson, I.M., 2012b, Uranium transport across basement/cover interfaces by buoyancy-driven thermohaline convection: implications for the formation of unconformity-related uranium deposits: American Journal of Science 312, 994-1027.

Cuney, M., 2009, The extreme diversity of uranium deposits: Mineralium Deposita 44, 3-9.

Dahlkampt, F.J., 1978, Geologic appraisal of the Key Lake U-Ni deposits, northern Saskatchewan: Economic Geology, v. 73, p. 1430-1449.

Dieng, S., Kyser, K., Godin, L., 2013, Tectonic history of the North American shield recorded in uranium deposits in the Beaverlodge area, northern Saskatchewan, Canada: Precambrian Research, v. 224, p. 316-340.

Derome, D., Cathelineau, M., Cuney, M., Fabre, C., Lhomme, T., and Banks, D.A., 2005, Mixing of Sodic and Calcic Brines and Uranium Deposition at McArthur River, Saskatchewan, Canada: A Raman and Laser-Induced Breakdown Spectroscopic Study of Fluid Inclusions: Economic Geology, v.100, p. 1529-1545.

De Veslud, C.L.C., Cuney, M., Lorilleux, G., Royer, J.-J., and Jébrak, M., 2009, 3D modeling of uranium-bearing solution-collapse breccias in Proterozoic sandstones (Athabasca Basin, Canada)-Metallogenic interpretations: Computers & Geosciences, v. 35, p. 92-107.

Evans D.G., and Nunn J.A., 1989, Free thermohaline convection in sediments surrounding a salt column: Journal of Geophysical Research, v. 94, p. 413-422.

Fayek, M., and Kyser, T.K., 1997, Characterization of multiple fluid-flow events and rare-earth-element mobility associated with formation of unconformity- type uranium deposits in the Athabasca Basin, Saskatchewan: Canadian Mineralogist, v. 35, p. 627-658.

Finch, W., 1996, Uranium provinces of North America- their definition, distribution, and models: U.S. Geological Survey Bulletin, v. 2141.

Fridleifsson, I.B., Bertani, R., Huenges, E., Lund, J.W., Ragnarsson, A., and Rybach, L., 2008, The possible role and contribution of geothermal energy to the mitigation of climate change. IPCC Scoping Meeting on Renewable Energy Sources, Luebeck, Germany, 20-25 January, p. 59-80.

Freeze R.A., and Cherry, J.A., 1979, Groundwater. Prentice Hall, Englewood Cliffs, New Jersey

Garven, G., 1995, Continental-Scale Groundwater Flow and Geologic Processes: Annual Review of Earth and Planetary Sciences, v. 23, p. 89-117.

Garven, G., and Freeze, R.A., 1984, Theoretical analysis of the role of groundwater flow in the genesis of stratabound ore deposits: 2. Quantitative results: American Journal of Science, v. 284, p. 1125-1174.

Hajnal, Z., Györfi, I., Annesley, I.R., White, D.J., Powell, B., and Koch, R., 2005, International symposium on uranium production and raw materials for the nuclear fuel cycle - Supply and demand, economics, the environment and energy security: Extended synopses, Report IAEA-CN-128.

Hanor, J.S., 1987, Kilometer-scale thermohaline overturn of pore fluid in the Louisiana Gulf Coast: Nature, v. 327, p. 501-503.

Hiatt, E.E., Kyser, T.K., Fayek, M., Polito, P., Holk, G.J., and Riciputi, L.R., 2007, Early quartz cements and evolution of paleohydraulic properties of basal sandstones in three Paleoproterozoic continental basins: Evidence from in situ δ18O analysis of quartz cements: Chemical Geology, v. 238, p. 19-37.

Hitchon, B., 1969a, Fluid flow in the Western Canada Sedimentary Basin: 1. Effect of topography: Water Resources Research, v. 5, p. 186-195.

Hitchon, B., I 969b, Fluid flow in the Western Canada Sedimentary Basin: 2. Effect of geology: Water Resources Research, v. 5, p. 460-469.

Hoeve, J., and Quirt, D., 1984, Mineralization and host rock alteration in relation to clay mineral diagenesis and evolution of the middle Proterozoic, Athabasca basin, northern Saskatchewan, Canada: Saskatchewan Research Council Technical Report, 187p.

Hoeve, J., Rawsthorn, K., and Quirt, D., 1981, Uranium metallogenetic studies: clay mineral stratigraphy and diagenesis in the Athabasca Group: Saskatchewan Research Council Publication, v. 22, p. 76-89.

Hoeve, J., and Sibbald, T.I.I., 1978, On the genesis of Rabbit Lake and other unconformity-type uranium deposits in northern Saskatchewan, Canada: Economic Geology, v. 73, 1450-1473.

Jefferson, C.W., Thomas, D.J., Gandhi, S.S., Ramaekers, P., Delaney, G., Brisbin, D., Cutts, C., Quirt, D., Portella, P., and Olson, R.A., 2007, Unconformity associated uranium deposits of the Athabasca Basin, Saskatchewan and Alberta. In:

Goodfellow, W.D. (Ed.), Mineral Deposits of Canada: A Synthesis of Major Deposit-types, District Metallogeny, the Evolution of Geological Provinces, and Exploration Methods: Geological Association of Canada, Mineral Deposits Division, Special Publication, v. 5, pp. 273-305.

Kojima, S., Takeda, S., and Kogita, S., 1994, Chemical factors controlling the solubility of uraninite and their significance in the genesis of unconformity-related uranium deposits: Mineralium Deposita, v. 29, p. 353-360.

Komninou, A., and Sverjensky, D.A., 1996, Geochemical modeling of the formation of an unconformity-type uranium deposit: Economic Geology, v. 91, p. 590-606.

Kotzer, T.G., and Kyser, T.K., 1995, Petrogenesis of the Proterozoic Athabasca basin, northern Saskatchewan, Canada, and its relation to diagenesis, hydrothermal uranium mineralization and Paleohydrogeology: Chemical Geology, v. 120, p. 45-89.

Kyser, K., Cuney, M., 2009, Unconformity-related uranium deposits, in Cuney, M, Kyser K, eds, Recent and not-so-recent developments in uranium deposits and implications for exploration: Mineralogical Association of Canada (MAC) and the Society for Geology Applied to Mineral Deposits (SGA), v. 39, p. 161-219.

Kyser, T.K., Wilson, M.R., and Ruhrmann, G., 1989, Stable isotope constraints on the role of graphite in the genesis of unconformity-type uranium deposits: Canadian Journal of Earth Sciences, v. 26, p. 490-498.

Kuhn, M., Alt-Epping, P., Gessner, K., and Wilde, A., 2004, Application of reactive transport modeling to the Mount Isa Copper mineralized system: Predictive mineral discovery CRC conference, Barossa Valley, Australia, p. 107-110.

Kuhn, M., and Gessner, K., 2009, Coupled process models of fluid flow and heat transfer in hydrothermal systems in three dimensions: Surveys in Geophysics, v. 30, p. 193-210. doi:10.1007/s10712-009-9060-8.

Kuhn, M., and Gessner, K., 2006, Reactive transport model of silicification at the Mount Isa copper deposit, Australia: Journal of Geochemical Exploration, v. 89, p. 195-198.

Kwon, O., B. T. Ngwenya, I. G. Main, and Elphick S. C., 2005, Permeability evolution during deformation of siliciclastic sandstones from Moab, Utah, in R. Sorkhabi and Y. Tsuji, eds., Faults, fluid flow, and petroleum traps: AAPG Memoir, v. 85, p. 219 –-236.

Lai, K.H., Chen, J., H., Liu, C.W., and Yang, S.Y., 2012, Effect of permeability–porosity functions on simulated morphological evolution of a chemical dissolution front: Hydrological Processes. doi: 10.1002/hyp.9492.

Lasaga, A.C., 1984, Chemical kinetics of water-rock interactions: Journal of Geophysical Research, v. 89, p. 4009-4025.

Li, Z., Chi, G., Bethune, K.M., Bosman, S.A., and Card, C.D., 2015, Geometric and Hydrodynamic Modeling and Fluid-structural Relationships in the Southeastern Athabasca Basin and Significance for Uranium Mineralization, in Targeted Geoscience Initiative 4: unconformity-related uranium systems, (ed.) E.G. Potter and D.M. Wright; Geological Survey of Canada, Open File 7791, p. 103-114. doi:10.4095/295776.

Lonergan, L.,and Wilkinson, J.J., 2000, Fractures, Fluid Flow and Mineralization: Eos Transactions American Geophysical Union 81, no. 19.

Lorilleux, G., Cuney, M., Je´brak, M., Rippert, J.C., and Portella, P., 2003, Chemical brecciation processes in the Sue unconformity-type uranium deposits, Eastern Athabasca Basin (Canada): Journal of Geochemical Exploration, v. 80, p. 241-258.

McGill, B., Marlatt, J., Matthews, R., Sopuck, V., Homeniuk, L., and Hubregtse, J., 1993. The P2 North uranium deposit Saskatchewan, Canada: Exploration Mining Geology, v. 2, p. 321-331.

McGill, B., 1999, The MacArthur River Deposit-A Geological Update, in Uranium Deposit Studies and Exploration Techniques: Saskatchewan Geological Society Special Publication Number 14: MINEXPO'96 SYMPOSIUM - Advances in Saskatchewan Geology and Mineral Exploration, Proceedings of a Symposium, Saskatoon, Saskatchewan, 21-22 November.

Mclellan, J.G., Oliver, N.H.S., and Schaubs, P.M., 2004, Fluid flow in extensional environments: Numerical modeling with an application to Hamersley iron ores: Journal of Structural geology, v. 26, p. 1157-117.

Miller, A.R., 1995, Polymetallic unconformity-related uranium veins in lower Proterozoic Amer group, Pelly Lake map area, northern Thelon Basin, Churchill Province, Northwest Territories: Geological Survey of Canada, p. 151-161.

Mercadier, J., Richard, A., Boiron, M.C., Cathelineau, M., and Cuney, M., 2010, Migration of brines in the basement rocks of the Athabasca Basin through microfracture networks (P-Patch U deposit, Canada): Lithos, v. 115, p. 121-136.

Miller, A.R., 1995, Polymetallic unconformity-related uranium veins in lower Proterozoic Amer group, Pelly Lake map area, northern Thelon Basin, Churchill

Province, Northwest Territories. In Current Research 1995-C: Geological Survey of Canada, p. 151-161.

Millington, R.J., Quirk, J.P., 1961, Permeability of porous solids: Trans. Faraday Soc, v. 57, p. 1200-1207.

Morichon, E., Beaufort, D., Allard, T., and Quirt, D., 2010, Tracing past migrations of uranium in Paleoproterozoic basins: New insights from radiation-induced defects in clay minerals: Geology, v. 38, p. 983-986.

Narasimhan, T.N., and Witherspoon, P.A., 1976, An integrated finite difference method for analyzing fluid flow in porous media: Water Resources Research, v. 12, p. 57-64.

Nogues, J.P., Fitts, J. P.,Celia, M.A., and Peters, C.A., 2013, Permeability evolution due to dissolution and precipitation of carbonates using reactive transport modeling in pore networks: Water Resources Research, v. 49, p. 6006-6021. doi:10.1002/wrcr.20486, 2013.

Oliver, N.H.S.., McLellan, J.G., Hobbs, B.E., Cleverley, J.S., Ord, A., and Feltrin, L., 2006, Numerical models of extensional deformation, heat transfer, and fluid flow across basement-cover interfaces during basin-related mineralization: Economic Geology, v. 101, p. 1-31.

Pascal, M., Ansdell, K.M., and Annesley, I.R., 2015, Graphite-bearing and graphite-depleted basement rocks in the Dufferin Lake zone, south-central Athabasca Basin, Saskatchewan; in Targeted Geoscience Initiative 4: unconformity-related uranium systems, (ed.), E.G. Potter and D.M. Wright: Geological Survey of Canada, Open File 7791, p. 83-92. doi:10.4095/295776.

Peiffert, C., Cuney, M., and Nguyen-Trung, C., 1994, Uranium in granitic magmas: Part 1. Experimental determination of uranium solubility and fluid-melt partition coefficients in the uranium oxide-haplogranite-H2O-Na2 CO3 system at 720-770°C, 2 kbar : Geochimica et Cosmochimica Acta 58, 2495-2507.

Peiffert, C., Nguyen-Trung, C., and Cuney, M., 1996, Uranium in granitic magmas: Part 2. Experimental determination of uranium solubility and fluid-melt partition coefficients in the uranium oxide-haplogranite-H 2 O-NaX (X = Cl, F) system at 770°C, 2 kbar: Geochimica et Cosmochimica Acta, v. 60, p. 1515-1529.

Potter, E.G., and Wright, D.M. (ed.), 2015, Targeted Geoscience Initiative 4: unconformity-related uranium systems: Geological Survey of Canada, Open File 7791, 126 p. doi:10.4095/295776.

Pruess, K., 1987, TOUGH user's guide: Nuclear Regulatory Commission, report NUREG/CR-4645 (also Lawrence Berkeley Laboratory Report LBL-20700, Berkeley, California).

Pruess, K., 1991, TOUGH2: A general numerical simulator for multiphase fluid and heat flow: Lawrence Berkeley Laboratory Report LBL-29400, Berkeley, California.

Pruess, K., Oldenburg, C., and Moridis, G., 1999, TOUGH2 user's guide, Version 2.0: Lawrence Berkeley Laboratory Report LBL-43134, Berkeley, California.

Quirt, D.H., Wasyliuk, K., 1997, Kaolinite, dickite, and other clay minerals in the Athabasca Group, Canada, and the Kombolgie Formation, Australia: 11th International Clay Conference, Ottawa, Ontario, June 1997, Proceedings, p. A61

Raffensperger, J.P., and Garven, G., 1995a, The formation of unconformity-type uranium ore deposits 1. Coupled ground water flow and heat transport modeling: American Journal of Science, v. 295, p. 581-636.

Raffensperger, J.P., and Garven, G., 1995b, The formation of unconformity-type uranium ore deposits 2. Coupled hydrochemical modeling. American Journal of Science, v. 295, p. 639-696.

Ramaekers, P., 1990, Geology of the Athabasca Group (Helikian) in northern Saskatchewan: Saskatchewan Energy and Mines, Saskatchewan Geological Survey, Report 195.

Renac, C., Kyser, T.K., Durocher, K., Dreaver, G., and O'Connor, T., 2002, Comparison of diagenetic fluids in the Proterozoic Thelon and Athabasca Basins, Canada: implications for protracted fluid histories in stable intracratonic basins: Canadian Journal of Earth Sciences, v. 39, p. 113-132.

Richard, A., Pettke, T., Cathelineau, M., Boiron, M.C., Mercadier, J., Cuney, M., Derome D., 2010, Brine–rock interaction in the Athabasca basement (McArthur River U deposit, Canada): consequences for fluid chemistry and uranium uptake: Terra Nova, v. 22, p.303-308.

Richard, A., Rozsypal, C., Mercadier, J., Banks, D. A., Cuney, M., Boiron, M. C., and Cathelineau, M., 2012, Giant uranium deposits formed from exceptionally uranium-rich acidic brines: Nature Geoscience, v. 5, p. 142-146.

Rutqvist, J., Rinaldi, A.P., Cappa, F., and Moridis, G.J., 2013, Modeling of fault reactivation and induced seismicity during hydraulic fracturing of shale-gas reservoirs: Journal of Petroleum Science and Engineering, v. 107, p. 31-44.

Senger, R.K., Fogg, G.E., 1987, Regional underpressuring in deep brine aquifers, Palo Duro Basin, Texas. 1 . Effects of hydrostratigraphy and topography: Water Resources Research, v. 23, p. 1481-1493.

Steefel, C.I., and Lasaga, A.C., 1994, A coupled model for transport of multiple chemical species and kinetic precipitation/dissolution reactions with applications to reactive flow in single phase hydrothermal system: American Journal of Science, v. 294, p. 529-592.

Thomas, D.J., Matthews, R., and Sopuck, V., 2000, Athabasca Basin (Canada) unconformity-type uranium deposits: Exploration model, current mine developments and exploration directions, in Cluer JK, Price JG, Struhsacker EM, Hardyman RF, Morris, C.L., eds., Geology and Ore Deposits 2000: The Great Basin and Beyond: Geological Society of Nevada Symposium, Reno, May 15-18, Proceedings, v. 1, p.103-126

Tremblay, L.P., 1982, Geology of the uranium deposits related to sub-Athabasca unconformity, Saskatchewan. Geological Society of Canada, Paper 81-20.

Vajdova, V., Baud, P., and Wong, T., 2004, Permeability evolution during localized deformation in Bentheim sandstone: Journal of Geophysical Research, DOI: 10.1029/2003JB002942.

Wang, K., Chi, G., Bethune, K.M., and Card, C.D., 2015, Fluid composition, thermal conditions, fluid-structural relationships and graphite alteration of the Phoenix uranium deposit, Athabasca Basin, Saskatchewan; in Targeted Geoscience Initiative 4: unconformity-related uranium systems, (ed.), E.G. Potter and D.M. Wright. Geological Survey of Canada, Open File 7791, p. 93-102. doi:10.4095/295776.

Walshe, J., 1986, A six component chlorite solid solution model and the conditions of chlorite formation in hydrothermal and geothermal systems: Economic Geology, v. 81, p. 681.703.

Walter, A.L., Frind, E.O., Blowes, D.W., Ptacek, C.J., and Molson, J.W., 1994, Modeling of multicomponent reactive transport in groundwater: 1, Model development and evaluation: Water Resources Research, v. 30, p. 3137-3148.

Wilde, A.R., Bloom, M.S., and Wall, V.J, 1989a, Transport and deposition of gold, uranium, platinum-group elements in unconformity- related uranium deposits: Economic Geology Monographs, v. 6, p. 637-650.

Wilde, A.R., Mernagh, T.P., Bloom., M.S., and Hoffmann, C.F., 1989b, Fluid inclusion evidence on the origin of some Australian unconformity-related uranium deposits: Economic Geology, v. 84, p.1627-1642.

Wilde, A.R, Wall, V.G., and Bloom, M.S., 1985, Wall-rock alteration associated with unconformity-related uranium deposits Northern Territory, Australia: implications for uranium transport and depositional mechanisms: Int. Meet. 'Concentration Mechanisms of Uranium in Geological Environments', Nancy, France, pp 231-239.

Wolery, T.J., 1992, EQ3/6: Software package for geochemical modeling of aqueous systems: Package overview and installation guide (version 7.0): Lawrence Livermore National Laboratory Report UCRL-MA-110662 PT I, Livermore, California.

Xu, T., and Pruess, K., 2001, Modeling multiphase non-isothermal fluid flow and reactive geochemical transport in variably saturated fractured rocks: 1. methodology, American Journal of Science, v. 301, p. 16-33.

Xu, T., Sonnenthal, E., Spycher, N., and Pruess, K., 2004, TOUGHREACT user's guide: A simulation program for nonisothermal multiphase reactive geochemical transport in variably saturated geologic media: Earth Sciences Division, Lawrence Berkeley National Laboratory Report CA 94720, Berkeley, California.

Yeh, G.T., Tripathi, V.S.A., 1991, Model for simulating transport of reactive multispecies components: model development and demonstration, Water Reources Research, v. 27, p. 3075-3094.

Chapter 5

Summary of original contribution and recommendations for future work

5.1 Summary of original contribution

5.1.1 The effect of a graphite zone

The effect of a graphite zone on the formation of URU deposits was numerically investigated by considering two different reducing mechanisms for the precipitation of uranium. The first reducing mechanism involves methane, produced by the alteration of the graphite zone, as the reducing agent, and the second one uses oxygen for formulating the redox reaction of uraninite precipitation. Either reducing mechanism leads to the precipitation of uraninite below the unconformity interface and away from the faulted graphite zone. Simulation results confirm that uraninite can precipitate even if methane is not involved as the reducing agent. The alteration of graphite, which provides methane, is not always required for uraninite precipitation. However, methane produces a better reducing environment for uraninite precipitation and leads to the formation of higher grade uranium deposits. The faulted graphite zone is important since it also serves as a pathway for the interaction of the basinal sandstone with the basement formation. The uranium-bearing brines flow into the faulted graphite zone and interact with the basement lithology. Also, fluids in the basement use the faulted graphite zone as a conduit to mix with the basinal fluids.

5.1.2 The role of physicochemical parameters

Simulation results confirm that favorable physicochemical conditions (e.g., temperature, pressure, pH, and oxygen fugacity) are required to form URU deposits over a time period of 0.1–1 million years. Uranium mineralization occurs in the locales experiencing a reduction of oxygen fugacity and temperature, and having a temperature of 160-180 °C and a pH of 4-4.5. From a geochemical point of view, these parameters collectively control whether the metals are deposited to form ore, or remain in the fluids to be transported elsewhere.

5.1.3 Evaluation of Fe-rich chlorite as a reducing agent

Simulation results confirm that Fe^{2+}, released by the destruction of Fe-rich chlorite, is a viable reducing agent for uraninite precipitation. Uraninite precipitates in the basement either away from the fault zone or along the fault zone, depending on the fault permeability, as a result of the redox process. Hydraulic properties of the fault zone control the fluid flow pattern within the basinal sandstone, and play a critical role in the formation and location of URU deposits. A hydraulically more permeable fault tends to lead to uraninite precipitation along the fault zone in the basement; while a less permeable fault more likely leads to the formation of URU deposits in the basement and away from the fault zone.

5.1.4 The uranium source

To address the question of where the large amount of uranium is sourced for uranium mineralization, two models were developed. In the first model, the sandstone is assumed to be a uranium source by assigning an initial fluid composition of 1×10^{-4} mol/L ($\simeq$ 27 ppm) total uranium therein. In the second model, the basement is considered to be a uranium source by assigning the same initial fluid composition. Both models are compared with each other in terms of their capacity to form a typical URU deposit. The simulation results show that precipitated uraninite in the first model has a higher grade (0.43 %) compared with that in the second model (0.29 %). In addition, the first model exhibits both chlorite and muscovite alterations that are commonly present in most basement-hosted URU deposits, whereas the second model exhibits only a muscovite alteration zone. Therefore, our results support the concept that the source of uranium in the major URU deposits seems to be more likely from the basinal sandstones, rather than the basement.

5.1.5 The role of hydrodynamic factors

A number of reactive flow modeling experiments were carried out by assigning different dip angles and directions to the fault and various permeabilities to the hydrostratigraphic units involved. Our numerical results show that the fault dip angle and direction, and the permeability of the hydrostratigraphic units govern the flow convection pattern, temperature distribution, and consequently the uranium mineralization. A vertical fault results in uranium mineralization at the bottom of the fault within the basement, while a dipping fault leads to uraninite precipitation below the unconformity either away from or along the fault, depending on the fault permeability. Regardless of the reducing

agent, a more permeable fault induces uraninite precipitation along the fault zone, whereas a less permeable fault gives rise to the precipitation of uraninite away from it, as already stated in Section 5.1.3. No economic ore mineralization can form when either very low or very high permeabilities are assigned to the sandstone or the basement, which suggests that these units seem to have an optimal window of permeability for the formation of URU deposits. Our numerical results also confirm that the difference in size and grade of different URU deposits may result from the variation in fluid flow patterns and physicochemical conditions, which is caused by the change in structural features and hydraulic properties of the stratigraphic units involved.

5.2 Suggestions for future work

Several aspects with respect to the formation of URU deposits in sedimentary basins are still worthy of further investigation in more detail. This thesis can be used as a starting point for future research as follows.

1. This thesis only investigated the fluid flow and uranium mineralization during tectonically quiet periods, without taking into account the control of tectonic deformation. The reason is that we currently do not have a software package that couples fluid flow, heat transport, rock deformation, and reactive mass transport in a collective manner. In order to understand the connection between the physical and chemical aspects of the ore-forming fluid and the possible role that structural deformation may have

played, future work will need to fully couple reactive flow modeling with tectonic deformation.

2. This thesis only dealt with 2D modeling, without considering the complexities of 3D hydrothermal system in reality. Future work will need to fill in this gap. Recently, Li et al. (2015) constructed a 3D geometric model of the sub-Athabasca unconformity surface and basin stratigraphy using publicly available geological, geophysical and drill-hole data, which can be used to constrain future 3D reactive flow modeling.

3. In this thesis, the initial volume fraction of the minerals and concentration of the aqueous species were based on a previous study by Raffensperger and Garven (1995b). There are some disagreements regarding the volume fraction of the minerals present in each hydrostratigraphic unit in the Athabasca Basin. For example, Raffensperger and Garven (1995b) assumed k-feldspar to be a primary mineral in the Athabasca Group. However, other researchers (e.g., Kister et al., 2006; Hiatt et al., 2007) have argued that no preserved feldspar mineral grains have been observed in the Athabasca Group. More up-dated and complete data will therefore need to be incorporated into future reactive transport modeling.

References

Hiatt, E. E., Kyser, T. K., Fayek, M., Polito, P., Holk, G. J., and Riciputi, L. R., 2007, Early quartz cements and evolution of paleohydraulic properties of basal sandstones in three Paleoproterozoic continental basins: Evidence from in situ δ18O analysis of quartz cements: Chemical Geology, v. 238, p. 19-37.

Kister, P., Laverret, E., Quirt, D., Cuney, M., Patrier Mas, P., Beaufort, D. and Bruneton, D., 2006, Mineralogy and geochemistry of the host-rock alterations associated with the Shea Creek unconformity-type uranium deposits (Saskatchewan, Canada). Part 2. Regional scale spatial distribution of the Athabasca Group sandstone matrix minerals: Clays and Clay Minerals, v. 54, p. 295-313.

Li, Z., Chi, G., Bethune, K.M., Bosman, S.A., and Card, C.D., 2015, Geometric and Hydrodynamic Modeling and Fluid-structural Relationships in the Southeastern Athabasca Basin and Significance for Uranium Mineralization, in Targeted Geoscience Initiative 4: unconformity-related uranium systems, (ed.) E.G. Potter and D.M. Wright: Geological Survey of Canada, Open File 7791, p. 103-114. Doi:10.4095/295776.

Raffensperger, J.P., and Garven, G., 1995b, The formation of unconformity- type uranium ore deposits 2. Coupled hydrochemical modeling: American Journal of Science, v. 295, p. 639-696.

Appendix 1 Governing equations and Integral Finite Differences (IFD) space discretization method

The governing equations for reactive mass transport modeling include coupled non-isothermal fluid flow, solute transport, and reactive geochemistry. The flow and transport equations which have a similar structure can be derived from the principle of mass and energy conservation. Table A.1 summarizes these equations and Table A.2 gives the meaning of the symbols used. The models for fluid and heat flow have been discussed in detail by Pruess (1987 and 1991) and Pruess et al. (1999). The chemical transport equations are written in terms of total dissolved concentrations of chemical components that are concentrations of their primary species plus their associated aqueous secondary species (Yeh and Tripathi, 1991; Steefel and Lasaga, 1994; Walter et al., 1994). Advection and diffusion processes are considered for chemical transport, and diffusion coefficients are assumed to be the same for all aqueous species. The primary governing equations given in Table A.1 must be complemented with constitutive relationships that express all parameters as functions of thermophysical and chemical variables. The expressions for non-isothermal flow are given by Pruess et al. (1999) and the expressions for chemical reactions are presented by Xu et al. (2004a).

For solving the governing equations, TOUGHREACT uses the Integral Finite Differences (IFD; Narasimhan and Witherspoon, 1976) space discretization method. For mesh generation, the code uses an algorithm (MeshMaker) (Pruess et al., 1999; 2012) which is different from standard gridding methods. This algorithm uses local coordinates

(rather than global coordinates) to describe the relative positions of the centers of the grid block elements.

The discretization approach used in the IFD method and the definition of the geometric parameters are illustrated in Fig. A.1. To illustrate the IFD method, let the shaded region (Fig. A.1a) to be an element whose average properties are associated with a representative nodal point m = 6, which may be located anywhere within or on the boundaries of the element. The basic mass- (for water and chemical components) and energy- (for heat) balance equations are written in integral form for an arbitrary domain V_n (Fig. A.1b)

$$\frac{d}{dt}\int_{V_n} M^K dV_n = \int_{\Gamma_n} \boldsymbol{F}^K \bullet \boldsymbol{n} d\Gamma_n + \int_{V_n} q^K d\, V_n \qquad \text{(A.1)}$$

Which can be written as follows:

$$V_n \frac{\Delta M_n}{\Delta t} = \sum_m A_{nm} F_{nm} + V_n q_n \qquad \text{(A.2)}$$

where subscript n labels a grid block, subscript m labels grid blocks connected to grid block n, Δt is time step size, and M_n is the average mass or energy density in grid block n. Surface integrals are approximated as a discrete sum of averages over surface segments A_{nm}, F_{nm} is the average flux (of mass or energy) over the surface segment A_{nm}between volume elements n and m (Fig. A.1c), and q_n is the average source/sink rate in grid block n per unit volume. The IFD method gives a flexible discretization for geologic media that allows the use of irregular unstructured grids, which is well-suited for simulation of flow, transport, and fluid-rock interaction in multi-region heterogeneous and fractured rock

systems. For systems with regular grids, IFD is equivalent to conventional finite differences.

Table A.1. Mathematical equations for fluid and heat flow, and chemical transport (Xu et al., 2004a).

General governing equations:	$\frac{\partial M_\kappa}{\partial t} = -\nabla F_\kappa + q_\kappa$		
Water:	$M_w = \phi(S_l\rho_l X_{wl} + S_g\rho_g X_{wg})$	$F_w = X_{wl}\rho_l \mathbf{u}_l + X_{wg}\rho_g \mathbf{u}_g$	$q_w = q_{wl} + q_{wg}$
Air:	$M_c = \phi(S_l\rho_l X_{cl} + S_g\rho_g X_{cg})$	$F_c = X_{cl}\rho_l \mathbf{u}_l + X_{cg}\rho_g \mathbf{u}_g$	
	$q_c = q_{cl} + q_{cg} + q_{cr}$		
Heat:	$M_h = \phi(S_l\rho_l U_l + S_g\rho_g U_g) + (1-\phi)\rho_s U_s$	$F_h = \sum_{\beta=l,g} h_\beta \rho_\beta \mathbf{u}_\beta - \lambda\nabla T$	q_h
	where $\mathbf{u}_\beta = -k\frac{k_{r\beta}}{\mu_\beta}\left(\nabla P_\beta - \rho_\beta \mathbf{g}\right)$ $\beta = l, g$		(Darcy's Law)
Chemical components in the liquid phase ($j = 1,2,\ldots,N_l$):			
	$M_j = \phi S_l C_{jl}$	$F_j = \mathbf{u}_l C_{jl} - (\tau\phi S_l D_l)\nabla C_{jl}$	$q_j = q_{jl} + q_{js} + q_{jg}$
		$\tau_\beta = \phi^{1/3} S_\beta^{7/3}$	(Millington and Quirk, 1961)

Table A.2. Symbols used in Table 1.1.

C	component concentration, mol L^{-1}	ρ	density , kg m^{-3}
D	diffusion coefficient, $m^2 s^{-1}$	μ	viscosity, kg $m^{-1}s^{-1}$
F	mass flux, kg $m^{-2}s^{-1}$ (*)	λ	heat conductivity, W $m^{-1}K^{-1}$
k	permeability, m^2		
k_r	relative permeability	Subscripts:	
g	gravitational acceleration, m s^{-2}	c	air
M	mass accumulation, kg m^{-3}	g	gas phase
N	number of chemical components	h	heat
p	pressure, Pa	j	aqueous chemical component
q	source/sink	l	liquid phase
S	saturation	r	reaction
T	temperature, °C	s	solid phase
U	internal energy, J kg^{-1}	w	water
u	Darcy velocity, m s^{-1}	κ	governing equation index
X	mass fraction	β	phase index
ϕ	porosity	τ	medium tortuosity

(*) For chemical transport and reaction calculations, molar units are used instead of kg.

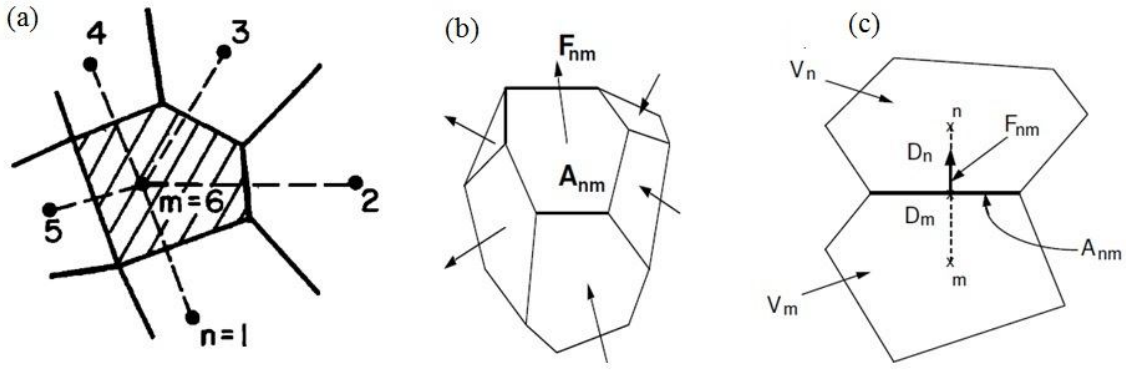

Fig. A.1. Space discretization and geometric data for the integral finite difference method.

The time discretization of fluid and heat flow equations results in a set of coupled nonlinear algebraic equations for the unknown thermodynamic state variables in all grid blocks. These equations are solved by Newton-Raphson iteration. The set of coupled linear equations arising at each iteration step is solved iteratively. Different solvers are available in TOUGHREACT, including bi-conjugate gradient, Lanczos-type bi-conjugate gradient, generalized minimum residual, and stabilized bi-conjugate gradient. The convergence is usually attained in 3-4 iterations. If the convergence cannot be achieved within a certain number of iterations (default is 8), the time step size will be reduced and a new iteration process will be started automatically.

Appendix 2 Geochemical subsystem which includes primary species, secondary species, and the minerals along with their associated reactions (methane as a reducing agent)

Primary species (components)	H^+, HCO_3^-, CH_4^0 (aq), H_2O , Ca^{2+}, Cl^-, Fe^{2+}, Mg^{2+}, Na^+, SiO_2(aq), SO_4^{2-}, AlO_2^-, k^+, UO_2^{2+}
Secondary species (aqueous complexes)	**Chemical reaction**
OH^-	$OH^- + H^+ \leftrightarrow H_2O$
HCl (aq)	$HCl \leftrightarrow H^+ + Cl^-$
CO_2(aq)	$CO_2 + H_2O \leftrightarrow H^+ + HCO_3^-$
CO_3^{-2}	$CO_3^{-2} + H^+ \leftrightarrow HCO_3^-$
HSO_4^-	$HSO_4^- \leftrightarrow H^+ + SO_4^{2-}$
H_2S (aq)	$H_2S + H_2O + HCO_3^- \leftrightarrow H^+ + CH_4(aq) + SO_4^{2-}$
$HSiO_3^-$	$HSiO_3^- + H^+ \leftrightarrow H_2O + SiO_2(aq)$
$HFeO_2^-$	$HFeO_2^- + 3H^+ \leftrightarrow Fe^+ + 2H_2O$
NaOH (aq)	$NaOH + H^+ \leftrightarrow Na^+ + H_2O$
NaCl (aq)	$NaCl \leftrightarrow Na^+ + Cl^-$
$NaHCO_3$ (aq)	$NaHCO_3 \leftrightarrow HCO_3^- + Na^+$
$NaHSiO_3$ (aq)	$NaHSiO_3 + H^+ \leftrightarrow H_2O + Na^+ + SiO_2$
KOH (aq)	$KOH + H^+ \leftrightarrow K^+ + H_2O$

KCl (aq)	$KCl \leftrightarrow K^+ + Cl^-$
KSO_4^-	$KSO_4^- \leftrightarrow K^+ + SO_4^{2-}$
$KHSO_4$ (aq)	$KHSO_4 \leftrightarrow H^+ + K^+ + SO_4^{2-}$
$CaCl^+$	$CaCl^+ \leftrightarrow Ca^{2+} + Cl^-$
$CaCl_2$ (aq)	$CaCl_2 \leftrightarrow Ca^{2+} + 2Cl^-$
$CaCO_3$ (aq)	$CaCO_3 + H^+ \leftrightarrow Ca^{2+} + HCO_3^-$
$CaHCO_3^+$	$CaHCO_3^+ \leftrightarrow Ca^{2+} + HCO_3^-$
$CaSO_4$ (aq)	$CaSO_4 \leftrightarrow Ca^{2+} + SO_4^{2-}$
$MgOH^+$	$MgOH^+ + H^+ \leftrightarrow Mg^{2+} + H_2O$
MgO (aq)	$MgO + 2H^+ \leftrightarrow Mg^{2+} + H_2O$
$MgCl^+$	$MgCl^+ \leftrightarrow Mg^{2+} + Cl^-$
$MgCO_3$ (aq)	$MgCO_3 + H^+ \leftrightarrow HCO_3^- + Mg^{2+}$
$MgHCO_3^+$	$MgHCO_3^+ \leftrightarrow HCO_3^- + Mg^{2+}$
U^{3+}	$U^{3+} + \frac{3}{8}HCO_3^- + \frac{7}{8}H_2O \leftrightarrow UO_2^{2+} + \frac{3}{8}CH_4^0(aq) + \frac{5}{8}H^+$
U^{4+}	$U^{4+} + \frac{1}{4}HCO_3^- + \frac{5}{4}H_2O \leftrightarrow UO_2^{2+} + \frac{1}{4}CH_4^0(aq) + \frac{7}{4}H^+$
$UO_2(CO_3)_2^{-2}$	$UO_2(CO_3)_2^{-2} + 2H^+ \leftrightarrow UO_2^{2+} + 2HCO_3^-$
UO_2Cl^+	$UO_2Cl^+ \leftrightarrow UO_2^{2+} + Cl^-$
UO_2Cl_2(aq)	$UO_2Cl_2 \leftrightarrow UO_2^{2+} + 2Cl^-$

$UO_2CO_3(aq)$	$UO_2CO_3 + H^+ \leftrightarrow UO_2^{2+} + HCO_3^-$
$UO_2SO_4(aq)$	$UO_2SO_4 \leftrightarrow UO_2^{2+} + SO_4^{2-}$
$AlOH^{2+}$	$AlOH^{2+} + H_2O \leftrightarrow 3H^+ + AlO_2^-$
$HAlO_2(aq)$	$HAlO_2 \leftrightarrow H^+ + AlO_2^-$
Al^{3+}	$Al^{3+} + 2H_2O \leftrightarrow 4H^+ + AlO_2^-$
$NaAlO_2(aq)$	$NaAlO_2 \leftrightarrow Na^+ + AlO_2^-$
$AlSO_4^+$	$AlSO_4^+ + 2H_2O \leftrightarrow SO_4^{2-} + 4H^+ + AlO_2^-$
$FeCl_2^+$	$FeCl_2^+ + \frac{1}{8}CH_4 + \frac{3}{8}H_2O \leftrightarrow Fe^{2+} + \frac{1}{8}HCO_3^- + + \frac{9}{8}H^+ + 2Cl^-$
$FeOH^+$	$FeOH^+ + H^+ \leftrightarrow Fe^+ + H_2O$
FeO (aq)	$FeO + 2H^+ \leftrightarrow Fe^+ + H_2O$
$FeCl^+$	$FeCl^+ \leftrightarrow Fe^{2+} + Cl^-$
$FeCl_2(aq)$	$FeCl_2 \leftrightarrow Fe^{2+} + 2Cl^-$
$FeHCO_3^+$	$FeHCO_3^+ \leftrightarrow Fe^{2+} + HCO_3^-$
Fe^{3+}	$Fe^{3+} + \frac{3}{8}H_2O + \frac{1}{8}CH_4 \leftrightarrow Fe^{2+} + \frac{9}{8}H^+ + \frac{1}{8}HCO_3^-$
HS^-	$HS^- + HCO_3^- + H_2O = SO_4^{2-} + CH_4$
Minerals	**Chemical reaction**

Graphite	$C + \frac{3}{2}H_2O \leftrightarrow \frac{1}{2}H^+ + \frac{1}{2}HCO_3^- + \frac{1}{2}CH_4^0(aq)$
Halite	$NaCl \leftrightarrow Na^+ + Cl^-$
Albite	$NaAlSi_3O_8 \leftrightarrow Na^+ + 3SiO_2(aq) + AlO_2^-$
Sylvite	$KCl \leftrightarrow K^+ + Cl^-$
K-feldspar	$KAlSi_3O_8 \leftrightarrow K^+ + 3SiO_2(aq) + AlO_2^-$
Muscovite	$KAl_2(AlSi_3O_{10})(OH)_2 \leftrightarrow K^+ + 3SiO_2(aq) + 3AlO_2^- + 2H^+$
Calcite	$CaCO_3 + H^+ \leftrightarrow Ca^{2+} + HCO_3^-$
Dolomite	$CaMg(CO_3)_2 + 2H^+ \leftrightarrow Ca^{2+} + Mg^{2+} + 2HCO_3^-$
Anhydrite	$CaSO_4 \leftrightarrow Ca^{2+} + SO_4^{-2}$
Anorthite	$CaAl_2Si_2O_8 \leftrightarrow Ca^{2+} + 2SiO_2(aq) + 2AlO_2^-$
Magnesite	$MgCO_3 + H^+ \leftrightarrow Mg^{2+} + HCO_3^-$
Chlorite	$(Mg_{2.5}Fe_{2.5})Al_2Si_3O_{10}(OH)_8 + 8H^+ \leftrightarrow 3SiO_2(aq) + \frac{5}{2}Fe^{2+} + \frac{5}{2}Mg^{2+} + 8H_2O + 2AlO_2^-$
Uraninite	$UO_2 + \frac{1}{4}HCO_3^- + \frac{9}{4}H^+ \leftrightarrow UO_2^{2+} + \frac{3}{4}H_2O + \frac{1}{4}CH_4^0(aq)$
Rutherfordine	$UO_2CO_3 + H^+ \leftrightarrow UO_2^{2+} + HCO_3^-$
Kaolinite	$Al_2Si_2O_5(OH)_4 \leftrightarrow 2H^+ + 2SiO_2(aq) + H_2O + 2AlO_2^-$
Hematite	$Fe_2O_3 + \frac{15}{4}H^+ + \frac{1}{4}CH_4 \leftrightarrow 2Fe^{2+} + \frac{1}{4}HCO_3^- + \frac{9}{4}H_2O$

Magnetite	$Fe_3O_4 + \frac{23}{4}H^+ + \frac{1}{4}CH_4 \leftrightarrow 3Fe^{2+} + \frac{1}{4}HCO_3^- + \frac{13}{4}H_2O$
Siderite	$FeCO_3 + H^+ \leftrightarrow Fe^{2+} + HCO_3^-$
Pyrite	$FeS_2 + \frac{11}{4}H_2O + \frac{7}{4}HCO_3^- \leftrightarrow 2SO_4^{2-} + \frac{1}{4}H^+ + Fe^{2+} + \frac{7}{4}CH_4$
Quartz	$SiO_2 \leftrightarrow SiO_2(aq)$

Appendix 3 Geochemical subsystem which includes primary species, secondary species, and the minerals along with their associated reactions (water as a reducing agent)

Primary species (components)	$H^+, HCO_3^-, H_2O, Ca^{2+}, Cl^-, Fe^{2+}, Mg^{2+}, Na^+, O_2(aq), SiO_2(aq), SO_4^{2-}, AlO_2^-, k^+, UO_2^{2+}$
Secondary species (aqueous complexes)	**Chemical reaction**
OH^-	$OH^- + H^+ \leftrightarrow H_2O$
HCl (aq)	$HCl \leftrightarrow H^+ + Cl^-$
$CO_2(aq)$	$CO_2 + H_2O \leftrightarrow H^+ + HCO_3^-$
CO_3^{-2}	$CO_3^{-2} + H^+ \leftrightarrow HCO_3^-$
HSO_4^-	$HSO_4^- \leftrightarrow H^+ + SO_4^{2-}$
H_2S (aq)	$H_2S + 2O_2(aq) \leftrightarrow 2H^+ + SO_4^{2-}$
$HSiO_3^-$	$HSiO_3^- + H^+ \leftrightarrow H_2O + SiO_2(aq)$
$HFeO_2^-$	$HFeO_2^- 3H^+ \leftrightarrow Fe^+ + 2H_2O$
NaOH (aq)	$NaOH + H^+ \leftrightarrow Na^+ + H_2O$
NaCl (aq)	$NaCl \leftrightarrow Na^+ + Cl^-$
$NaHCO_3$ (aq)	$NaHCO_3 \leftrightarrow HCO_3^- + Na^+$
$NaHSiO_3$ (aq)	$NaHSiO_3 + H^+ \leftrightarrow H_2O + Na^+ + SiO_2$

KOH (aq)	$KOH + H^+ \leftrightarrow K^+ + H_2O$
KCl (aq)	$KCl \leftrightarrow K^+ + Cl^-$
KSO_4^-	$KSO_4^- \leftrightarrow K^+ + SO_4^{2-}$
$KHSO_4$ (aq)	$KHSO_4 \leftrightarrow H^+ + K^+ + SO_4^{2-}$
$CaCl^+$	$CaCl^+ \leftrightarrow Ca^{2+} + Cl^-$
$CaCl_2$ (aq)	$CaCl_2 \leftrightarrow Ca^{2+} + 2Cl^-$
$CaCO_3$ (aq)	$CaCO_3 + H^+ \leftrightarrow Ca^{2+} + HCO_3^-$
$CaHCO_3^+$	$CaHCO_3^+ \leftrightarrow Ca^{2+} + HCO_3^-$
$CaSO_4$ (aq)	$CaSO_4 \leftrightarrow Ca^{2+} + SO_4^{2-}$
$MgOH^+$	$MgOH^+ + H^+ \leftrightarrow Mg^{2+} + H_2O$
MgO (aq)	$MgO + 2H^+ \leftrightarrow Mg^{2+} + H_2O$
$MgCl^+$	$MgCl^+ \leftrightarrow Mg^{2+} + Cl^-$
$MgCO_3$ (aq)	$MgCO_3 + H^+ \leftrightarrow HCO_3^- + Mg^{2+}$
$MgHCO_3^+$	$MgHCO_3^+ \leftrightarrow HCO_3^- + Mg^{2+}$
U^{3+}	$U^{3+} + \frac{3}{4}O_2(aq) + \frac{1}{2}H_2O \leftrightarrow UO_2^{2+} + H^+$
U^{4+}	$U^{4+} + \frac{1}{2}O_2(aq) + H_2O \leftrightarrow UO_2^{2+} + 2H^+$
$UO_2(CO_3)_2^{-2}$	$UO_2(CO_3)_2^{-2} + 2H^+ \leftrightarrow UO_2^{2+} + 2HCO_3^-$

UO_2Cl^+	$UO_2Cl^+ \leftrightarrow UO_2^{2+} + Cl^-$
$UO_2Cl_2(aq)$	$UO_2Cl_2 \leftrightarrow UO_2^{2+} + 2Cl^-$
$UO_2CO_3(aq)$	$UO_2CO_3 + H^+ \leftrightarrow UO_2^{2+} + HCO_3^-$
$UO_2SO_4(aq)$	$UO_2SO_4 \leftrightarrow UO_2^{2+} + SO_4^{2-}$
$AlOH^{2+}$	$AlOH^{2+} + H_2O \leftrightarrow 3H^+ + AlO_2^-$
$HAlO_2(aq)$	$HAlO_2 \leftrightarrow H^+ + AlO_2^-$
Al^{3+}	$Al^{3+} + 2H_2O \leftrightarrow 4H^+ + AlO_2^-$
$NaAlO_2(aq)$	$NaAlO_2 \leftrightarrow Na^+ + AlO_2^-$
$AlSO_4^+$	$AlSO_4^+ + 2H_2O \leftrightarrow SO_4^{2-} + 4H^+ + AlO_2^-$
$FeCl_2^+$	$FeCl_2^+ + \frac{1}{2} H_2O \leftrightarrow Fe^{2+} + 2Cl^- + \frac{1}{4} O_2(aq) + H^+$
$FeOH^+$	$FeOH^+ + H^+ \leftrightarrow Fe^+ + H_2O$
$FeO\ (aq)$	$FeO + 2H^+ \leftrightarrow Fe^+ + H_2O$
$FeCl^+$	$FeCl^+ \leftrightarrow Fe^{2+} + Cl^-$
$FeCl_2(aq)$	$FeCl_2 \leftrightarrow Fe^{2+} + 2Cl^-$
$FeHCO_3^+$	$FeHCO_3^+ \leftrightarrow Fe^{2+} + HCO_3^-$
Fe^{3+}	$Fe^{3+} + \frac{1}{2} H_2O \leftrightarrow Fe^{2+} + H^+ + \frac{1}{4} O_2(aq)$

HS^-	$HS^- + 2O_2(aq) \leftrightarrow H^+ + SO_4^{-2}$
Minerals	**Chemical reaction**
Graphite	$C + H_2O + O_2(aq) \leftrightarrow H^+ + HCO_3^-$
Halite	$NaCl \leftrightarrow Na^+ + Cl^-$
Albite	$NaAlSi_3O_8 \leftrightarrow Na^+ + 3SiO_2(aq) + AlO_2^-$
Sylvite	$KCl \leftrightarrow K^+ + Cl^-$
K-feldspar	$KAlSi_3O_8 \leftrightarrow K^+ + 3SiO_2(aq) + AlO_2^-$
Muscovite	$KAl_2(AlSi_3O_{10})(OH)_2 \leftrightarrow K^+ + 3SiO_2(aq) + 3AlO_2^- + 2H^+$
Calcite	$CaCO_3 + H^+ \leftrightarrow Ca^{2+} + HCO_3^-$
Dolomite	$CaMg(CO_3)_2 + 2H^+ \leftrightarrow Ca^{2+} + Mg^{2+} + 2HCO_3^-$
Anhydrite	$CaSO_4 \leftrightarrow Ca^{2+} + SO_4^{-2}$
Anorthite	$CaAl_2Si_2O_8 \leftrightarrow Ca^{2+} + 2SiO_2(aq) + 2AlO_2^-$
Magnesite	$MgCO_3 + H^+ \leftrightarrow Mg^{2+} + HCO_3^-$
Chlorite	$(Mg_{2.5}Fe_{2.5})Al_2Si_3O_{10}(OH)_8 + 8H^+ \leftrightarrow 3SiO_2(aq) + \frac{5}{2}Fe^{2+} + \frac{5}{2}Mg^{2+} + 8H_2O + 2AlO_2^-$
Uraninite	$UO_2 + \frac{1}{2}O_2(aq) + 2H^+ \leftrightarrow UO_2^{2+} + H_2O$
Rutherfordine	$UO_2CO_3 + H^+ \leftrightarrow UO_2^{2+} + HCO_3^-$

Kaolinite	$Al_2Si_2O_5(OH)_4 \leftrightarrow 2H^+ + 2SiO_2(aq) + H_2O + 2AlO_2^-$
Hematite	$Fe_2O_3 + 4H^+ \leftrightarrow 2H_2O + \frac{1}{2}O_2(aq) + 2Fe^{2+}$
Magnetite	$Fe_3O_4 + 6H^+ \leftrightarrow 3H_2O + \frac{1}{2}O_2(aq) + 3Fe^{2+}$
Siderite	$FeCO_3 + H^+ \leftrightarrow Fe^{2+} + HCO_3^-$
Pyrite	$FeS_2 + \frac{7}{2}O_2(aq) + H_2O \leftrightarrow Fe^{2+} + 2H^+ + 2SO_4^{-2}$
Quartz	$SiO_2 \leftrightarrow SiO_2(aq)$

Appendix 4. Geochemical subsystem which includes primary species, secondary species, and the minerals along with their associated reactions (ferrous iron as a reducing agent)

Primary species (components)	$H^+, HCO_3^-, H_2O, Ca^{2+}, Cl^-, Mg^{2+}, Na^+, SiO_2(aq), SO_4^{2-}, AlO_2^-, k^+, UO_2^{2+}, Fe^{2+}$
Secondary species (aqueous complexes)	**Chemical reaction**
OH^-	$OH^- + H^+ \leftrightarrow H_2O$
$O_2(aq)$	$O_2 + 4Fe^{2+} + 4H_2O \leftrightarrow 2Fe_2O_3 + 8H^+$
HCl (aq)	$HCl \leftrightarrow H^+ + Cl^-$
$CO_2(aq)$	$CO_2 + H_2O \leftrightarrow H^+ + HCO_3^-$
CO_3^{-2}	$CO_3^{-2} + H^+ \leftrightarrow HCO_3^-$
HS^-	$HS^- + 4Fe_2O_3 + 15H^+ \leftrightarrow SO_4^{2-} + 8Fe^{2+} + 8H_2O$
HSO_4^-	$HSO_4^- \leftrightarrow H^+ + SO_4^{2-}$
H_2S (aq)	$H_2S + 4Fe_2O_3 + 14H^+ \leftrightarrow SO_4^{2-} + 8Fe^{2+} + 8H_2O$
$HSiO_3^-$	$HSiO_3^- + H^+ \leftrightarrow H_2O + SiO_2(aq)$
$HFeO_2^-$	$HFeO_2^- + 3H^+ \leftrightarrow Fe^{2+} + 2H_2O$
NaOH (aq)	$NaOH + H^+ \leftrightarrow Na^+ + H_2O$

NaCl (aq)	$NaCl \leftrightarrow Na^+ + Cl^-$
$NaHCO_3$ (aq)	$NaHCO_3 \leftrightarrow HCO_3^- + Na^+$
$NaHSiO_3$ (aq)	$NaHSiO_3 + H^+ \leftrightarrow H_2O + Na^+ + SiO_2$
KOH (aq)	$KOH + H^+ \leftrightarrow K^+ + H_2O$
KCl (aq)	$KCl \leftrightarrow K^+ + Cl^-$
KSO_4^-	$KSO_4^- \leftrightarrow K^+ + SO_4^{2-}$
$KHSO_4$ (aq)	$KHSO_4 \leftrightarrow H^+ + K^+ + SO_4^{2-}$
$CaCl^+$	$CaCl^+ \leftrightarrow Ca^{2+} + Cl^-$
$CaCl_2$ (aq)	$CaCl_2 \leftrightarrow Ca^{2+} + 2Cl^-$
$CaCO_3$ (aq)	$CaCO_3 + H^+ \leftrightarrow Ca^{2+} + HCO_3^-$
$CaHCO_3^+$	$CaHCO_3^+ \leftrightarrow Ca^{2+} + HCO_3^-$
$CaSO_4$ (aq)	$CaSO_4 \leftrightarrow Ca^{2+} + SO_4^{2-}$
$MgOH^+$	$MgOH^+ + H^+ \leftrightarrow Mg^{2+} + H_2O$
MgO (aq)	$MgO + 2H^+ \leftrightarrow Mg^{2+} + H_2O$
$MgCl^+$	$MgCl^+ \leftrightarrow Mg^{2+} + Cl^-$

$MgCO_3$ (aq)	$MgCO_3 + H^+ \leftrightarrow HCO_3^- + Mg^{2+}$
$MgHCO_3^+$	$MgHCO_3^+ \leftrightarrow HCO_3^- + Mg^{2+}$
U^{3+}	$U^{3+} + \frac{3}{2}Fe_2O_3 + 5H^+ \leftrightarrow UO_2^{2+} + 3Fe^{2+} + \frac{5}{2}H_2O$
U^{4+}	$U^{4+} + Fe_2O_3 + 2H^+ \leftrightarrow UO_2^{2+} + 2Fe^{2+} + H_2O$
UCl^{3+}	$UCl^{3+} + Fe_2O_3 + 2H^+ \leftrightarrow UO_2^{2+} + Cl^- + 2Fe^{2+} + H_2O$
UCl_2^{2+}	$UCl_2^{2+} + Fe_2O_3 + 2H^+ \leftrightarrow UO_2^{2+} + 2Cl^- + 2Fe^{2+} + H_2O$
$UHCO_3^{3+}$	$UHCO_3^{3+} + Fe_2O_3 + 2H^+ \leftrightarrow UO_2^{2+} + 2Fe^{2+} + HCO_3^- + H_2O$
$U(HCO_3)_2^{2+}$	$U(HCO_3)_2^{2+} + Fe_2O_3 + 2H^+ \leftrightarrow UO_2^{2+} + 2Fe^{2+} + 2HCO_3^- + H_2O$
UO_2^+	$UO_2^+ + \frac{1}{2}Fe_2O_3 + 3H^+ \leftrightarrow UO_2^{2+} + Fe^{2+} + \frac{3}{2}H_2O$
UO_2Cl(aq)	$UO_2Cl(aq) + \frac{1}{2}Fe_2O_3 + 3H^+ \leftrightarrow UO_2^{2+} + Fe^{2+} + \frac{3}{2}H_2O + Cl^-$
$UO_2Cl_2^-$	$UO_2Cl_2^- + \frac{1}{2}Fe_2O_3 + 3H^+ \leftrightarrow UO_2^{2+} + Fe^{2+} + \frac{3}{2}H_2O + 2Cl^-$
UO_2HCO_3(aq)	$UO_2HCO_3(aq) + \frac{1}{2}Fe_2O_3 + 3H^+ \leftrightarrow UO_2^{2+} + Fe^{2+} + \frac{3}{2}H_2O + HCO_3^-$
$UO_2(HCO_3)_2^-$	$UO_2(HCO_3)_2^- + \frac{1}{2}Fe_2O_3 + 3H^+ \leftrightarrow UO_2^{2+} + Fe^{2+} + \frac{3}{2}H_2O +$

	$2HCO_3^-$
UO_2Cl^+	$UO_2Cl^+ \leftrightarrow UO_2^{2+} + Cl^-$
$UO_2Cl_2(aq)$	$UO_2Cl_2 \leftrightarrow UO_2^{2+} + 2Cl^-$
$UO_2CO_3(aq)$	$UO_2CO_3 + H^+ \leftrightarrow UO_2^{2+} + HCO_3^-$
$UO_2HCO_3^+$	$UO_2HCO_3^+ \leftrightarrow UO_2^{2+} + HCO_3^-$
$UO_2(HCO_3)_2(aq)$	$UO_2(HCO_3)_2(aq) \leftrightarrow UO_2^{2+} + 2HCO_3^-$
$UO_2SO_4(aq)$	$UO_2SO_4 \leftrightarrow UO_2^{2+} + SO_4^{2-}$
$UO_2HSO_4^+$	$UO_2HSO_4^+ \leftrightarrow UO_2^{2+} + SO_4^{2-} + H^+$
$AlOH^{2+}$	$AlOH^{2+} + H_2O \leftrightarrow 3H^+ + AlO_2^-$
$AlCl^{2+}$	$AlCl^{2+} + 2H_2O \leftrightarrow AlO_2^- + Cl^- + 4H^+$
$AlCl_2^+$	$AlCl_2^+ + 2H_2O \leftrightarrow AlO_2^- + 2Cl^- + 4H^+$
$FeCl^{2+}$	$FeCl^{2+} + \frac{3}{2}H_2O \leftrightarrow \frac{1}{2}Fe_2O_3 + 3H^+ + Cl^-$
Fe^{3+}	$Fe^{3+} + \frac{3}{2}H_2O \leftrightarrow \frac{1}{2}Fe_2O_3 + 3H^+$
$FeOH^+$	$FeOH^+ + H^+ \leftrightarrow Fe^{2+} + H_2O$
FeO (aq)	$FeO + 2H^+ \leftrightarrow Fe^{2+} + H_2O$

$FeCl^+$	$FeCl^+ \leftrightarrow Fe^{2+} + Cl^-$
$FeCl_2(aq)$	$FeCl_2 \leftrightarrow Fe^{2+} + 2Cl^-$
$FeHCO_3^+$	$FeHCO_3^+ \leftrightarrow Fe^{2+} + HCO_3^-$
Minerals	**Chemical reaction**
Halite	$NaCl \leftrightarrow Na^+ + Cl^-$
Albite	$NaAlSi_3O_8 \leftrightarrow Na^+ + 3SiO_2(aq) + AlO_2^-$
Sylvite	$KCl \leftrightarrow K^+ + Cl^-$
K-feldspar	$KAlSi_3O_8 \leftrightarrow K^+ + 3SiO_2(aq) + AlO_2^-$
Muscovite	$KAl_2(AlSi_3O_{10})(OH)_2 \leftrightarrow K^+ + 3SiO_2(aq) + 3AlO_2^- + 2H^+$
Calcite	$CaCO_3 + H^+ \leftrightarrow Ca^{2+} + HCO_3^-$
Dolomite	$CaMg(CO_3)_2 + 2H^+ \leftrightarrow Ca^{2+} + Mg^{2+} + 2HCO_3^-$
Anhydrite	$CaSO_4 \leftrightarrow Ca^{2+} + SO_4^{-2}$
Anorthite	$CaAl_2Si_2O_8 \leftrightarrow Ca^{2+} + 2SiO_2(aq) + 2AlO_2^-$
Magnesite	$MgCO_3 + H^+ \leftrightarrow Mg^{2+} + HCO_3^-$
Chlorite	$(Mg_{2.5}Fe_{2.5})Al_2Si_3O_{10}(OH)_8 + 8H^+ \leftrightarrow 3SiO_2(aq) + \frac{5}{2}Fe^{2+} + \frac{5}{2}Mg^{2+} + 8H_2O + 2AlO_2^-$

Uraninite, Hematite	$UO_2 + Fe_2O_3 + 6H^+ \leftrightarrow UO_2^{2+} + 2Fe^{2+} + 3H_2O$
Rutherfordine	$UO_2CO_3 + H^+ \leftrightarrow UO_2^{2+} + HCO_3^-$
Kaolinite	$Al_2Si_2O_5(OH)_4 \leftrightarrow 2H^+ + 2SiO_2(aq) + H_2O + 2AlO_2^-$
Magnetite	$Fe_3O_4 + 2H^+ \leftrightarrow Fe_2O_3 + Fe^{2+} + H_2O$
Siderite	$FeCO_3 + H^+ \leftrightarrow Fe^{2+} + HCO_3^-$
Pyrite	$FeS_2 + 7Fe_2O_3 + 26H^+ \leftrightarrow 15Fe^{2+} + 2SO_4^{2-} + 13H_2O$
Graphite	$C + 2Fe_2O_3 + 7H^+ \leftrightarrow 4Fe^{2+} + HCO_3^- + 3H_2O$
Quartz	$SiO_2 \leftrightarrow SiO_2(aq)$

Vita Auctoris

Yousef Beiraghdar Aghbelagh was born in Tabriz, Iran. Upon completion of the high school, he successfully passed the national competitive entrance exam and entered the Teacher's Training University of Tehran where he obtained a BSc degree in Physics. He got a fellowship in 2004 and admitted into the MSc-Geophysics program at the University of Tehran. He graduated in 2007, and joined Research Institute of Petroleum Industry (RIPI) where he worked for three years. In 2011, he got admission into the PhD-Earth Sciences program at the University of Windsor and came to Canada to pursue his doctoral studies in Geofluids division at the Department of Earth and Environmental Sciences. He successfully defended his doctoral dissertation in May 2016.